Faculty of Electrical Engineering
Department of Computer Science

Master's thesis

Communication Infrastructure Building in Mobile Robot Exploration

Bc. Martin Zoula

January 2023

Supervisor: prof. Ing. Jan Faigl, Ph.D.

MASTER‘S THESIS ASSIGNMENT

I. Personal and study details

Student's name: **Zoula Martin** Personal ID number: **466113**

Faculty / Institute: **Faculty of Electrical Engineering**

Department / Institute: **Department of Computer Science**

Study program: **Open Informatics**

Specialisation: **Artificial Intelligence**

II. Master’s thesis details

Master’s thesis title in English:

Communication infrastructure building in mobile robot exploration

Master’s thesis title in Czech:

Budování komunikace v úloze robotického průzkumu neznámého prostředí

Guidelines:

Familiarize yourself with mobile robot exploration in communication-constrained environments [1, 2, 3].
Investigate methods for modeling communication accessibility and building mobile communication infrastructure [4, 5].
Propose a method for building communication infrastructure with communication accessibility modeling and prediction of the signal availability.
Develop the proposed method and experimentally verify it, preferably using communication modules developed in the Computational Robotics Laboratory or other available communication technology.

Bibliography / sources:

[1] Y. Marchukov: Multi-robot deployment planning in communication-constrained environments, Doctoral dissertation, Universidad de Zaragoza, 2019. https://zaguan.unizar.es/record/87036/files/TESIS-2020-017.pdf
[2] F. Amigoni, J. Banfi and N. Basilico: Multirobot Exploration of Communication-Restricted Environments: A Survey, IEEE Intelligent Systems, 32(6):48–57, 2017. https://doi.org/10.1109/MIS.2017.4531226
[3] Bayer, J. and Faigl, J.: Decentralized Topological Mapping for Multi-robot Autonomous Exploration under Low-Bandwidth Communication, European Conference on Mobile Robots (ECMR), 2021. https://doi.org/10.1109/ECMR50962.2021.9568824
[4] S. Greco: Experimental analysis of the impact of communication models on exploration strategies for multirobot systems, Master thesis, Politecnico di Milano, 2019, https://www.politesi.polimi.it/handle/10589/149822
[5] A. Quattrini Li, P.K. Penumarthi, J. Banfi, N. Basilico, J.M. O’Kane, I. Rekleitis, S. Nelakuditi, F. Amigoni: Multi-robot online sensing strategies for the construction of communication maps. Autonomous Robots, 44:299–319, 2020. https://doi.org/10.1007/s10514-019-09862-3

Name and workplace of master’s thesis supervisor:

prof. Ing. Jan Faigl, Ph.D. Artificial Intelligence Center FEE

Name and workplace of second master’s thesis supervisor or consultant:

Date of master’s thesis assignment: **28.01.2022** Deadline for master's thesis submission: **10.01.2023**

Assignment valid until: **30.09.2023**

prof. Ing. Jan Faigl, Ph.D.	Head of department’s signature	prof. Mgr. Petr Páta, Ph.D.
Supervisor’s signature		Dean’s signature

III. Assignment receipt

The student acknowledges that the master's thesis is an individual work. The student must produce his thesis without the assistance of others, with the exception of provided consultations. Within the master's thesis, the author must state the names of consultants and include a list of references.

. _____ Date of assignment receipt

_____ Student's signature

Declaration

I declare that the presented work was developed independently and that I have listed all sources of the information used within it in accordance with the methodical instructions for observing the ethiclal principles in the preparation of university theses.

Prague, January 10, 2023

. . . . . .

Bc. Martin Zoula

Acknowledgement

I want to thank my thesis supervisor Jan Faigl for guidance, consultations and encouragement for teaching. Further, Jan Bayer's assent to use his robotic exploration implementation and support in this regard is kindly appreciated. I also thank Kolektory Praha, a.s. and Regionální muzeum v Jílovém u Prahy for providing access to their premises. Besides, my thanks go to the whole amazing collective of the Computational Robotics Laboratory, their enthusiasm being my inspiration. Jag vill också tacka mina tyska, svenska och andra vänner för underbara tider i Sverige. A v neposlední řadě chci poděkovat celé své rodině za neochvějnou podporu.

Abstrakt

Tato diplomová práce se zabývá problematikou budování komunikační infrastruktury během autonomní robotické průzkumné mise v podzemním prostředí. Na základě souvisejících prací a v kontextu nedávné soutěže DARPA Subterranean Challenge je představena strategie automatického umisťování retranslačních rádiových stanic, které rozšiřují komunikační dosah základnové stanice. Cílem je tak udržet spojení robotu se základnovou stanicí při minimálním dopadu na průběh průzkumné mise. Proto je na cestě k aktuálnímu průzkumnému cíli vybírán nejvzdálenější navigační bod s dostatečnou očekávanou kvalitou signálu, ke kterému je robot navigován. Pokud takový navigační bod není nalezen, je položena retranslační stanice a mise pokračuje. Usiluje se tedy o udržení spojení mezi radiostanicemi při zachování nezměněné průzkumné cesty. Za tímto účelem se k extrapolaci dostupnosti signálu používá model šíření signálu. Práce se proto zaměřuje na vyhodnocení čtyř navržených modelů. Teorie vlnovodů je využita v práci navrženém lineárním vlnovodném modelu, který kromě predikce kvality signálu umožňuje určit některé charakteristiky prostředí z naměřených hodnot útlumu. Přístup je následně zobecněn ve varianci-vzorkujícím modelu a polynomiálním modelu, které využívají linearitu šíření vlnovodného signálu v kombinaci s technikami latentních prostorů. Poslední navržený model je založen na přímé regresi ze vzorků s využitím Gaussovských procesů. Modely jsou vyhodnoceny na vytvořeném souboru dat, který obsahuje přibližně $33\,000$ přesně lokalizovaných vzorků kvality signálu v prostředí městských kolektorů. Na základě prezentovaného vyhodnocení dosahuje nejlepších výsledků navržený varianci-vzorkující model, který za použití pouze šesti regresních parametrů dosahuje v interpolačních i extrapolačních scénářích zanedbatelné průměrné chyby se směrodatnou odchylkou okolo $10\,\mathrm{dB}$. Závěr práce je věnován experimentálnímu ověření navrženého konceptu budování komunikační infrastruktury během robotické mise v demonstrativním reálném nasazení ve štole Halíře poblíž Jílového u Prahy.

Klíčová slova: predikce dostupnosti komunikačního signálu; mobilní robotický průzkum; podzemní rádiová komunikace; strojové učení

Abstract

This thesis addresses the problem of communication infrastructure building during an autonomous robotic exploration mission in subterranean environments. A strategy for the automatic placement of retranslating radio stations that extend the base station communication range is presented based on related work and the context of the recent DARPA Subterranean Challenge. We aim to maintain connectivity with the base station while incurring minimal overhead to the exploration mission performance. The path to the current exploration goal is truncated to the farthest waypoint with sufficient expected signal, where the robot is navigated. If there are no farther waypoints with the expected signal coverage observed upon arrival, the radio station is placed, and the mission proceeds; thus, we aim to maintain the link between the radios while keeping the exploration path unchanged. To this end, an onboard computational signal propagation model is used to extrapolate signal availability. As signal propagation modeling in subterranean environments is of prime importance, the thesis focuses on evaluating four proposed models. The theory of oversized Waveguides is exploited in Waveguide Linear Model, providing a possibility of physically relevant material properties inference along the signal quality predictions. The approaches are combined in the Variance Windowing Model and Generic Embedding Polynomial Model, which take advantage of the linearity of the waveguide signal propagation combined with latent space embedding techniques. Finally, the Evidence Regression Model aggregates data by computing a low-dimensional description of space between radios, utilizing Gaussian Process as the regression method. The models are evaluated on a dataset gathered during work on the thesis, containing around $33\,000$ precisely localized signal quality samples from urban utility tunnels. The models are able to predict the signal with accuracy close to the inherent noise level in the dataset, with the Variance Windowing Model selected as the best-performing in extrapolation and interpolation scenarios with negligible bias and prediction standard deviation around $10\,\mathrm{dB}$ while requiring only six regression parameters. Finally, the presented concept of the communication infrastructure building in a robotic mission was demonstrated in a real-world deployment in a mine adit near Jílové u Prahy.

Keywords: communication signal availability prediction; mobile robotic exploration; subterranean radio communication; machine learning

Contents

List of Figures

List of Tables

List of Algorithms and Code Examples

Table of Abbreviations

CRAS	Center for Robotics and Autonomous Systems
CRL	Computational Robotics Laboratory
SubT	DARPA Subterranean Challenge
ERM	Evidence Regression Model
GEPM	Generic Embedding Polynomial Model
LiDAR	Light Detection and Ranging
MAE	Mean Absolute Error
ME	Mean Error (signed)
NORLAB	Northern Robotics Laboratory
ROS	Robot Operating System
RMSE	Root Mean Square Error
SAR	Search-and-Rescue
SLAM	Simultaneous Localization and Mapping
SD	Standard Deviation
VWM	Variance Windowing Model
WLM	Waveguide Linear Model

Table of Symbols

β	Attenuation coefficient
$\mathfrak{B}$	Bressenham's line algorithm
dB	Decibel
d	Distance
ρ	Electric charge density
j	Electric current density
E	Electric field
$\mathcal{E}$	Environment
$\hat{\mathcal{E}}$	Environment model
$\mathcal{F}_l$	Euclidean distance feature
$\mathcal{F}$	Feature vector
$\mathcal{GP}$	Gaussian Process
K	Gaussian Process kernel
O_{min}	Generalized q. of s., requested
O	Generalized quality of signal
$\mathcal{F}_v$	Geometric variable length f. v.
$\mathcal{F}_h$	Histogram feature vector
B	Magnetic field
m	Number of motes in a mission
μ	Permeability
ϵ	Permittivity
P	Position in $\mathbb{R}^3$
P_{BS}	Position of base station
P_{E}	Position of exploration goal
P_{R}	Position of robot
P_{R}^0	Position of robot, initial
C	Radios configuration
$\mathbb{C}$	Radios configuration domain
$C^\star$	Radios configuration, optimal
$\mathcal{F}_g$	Segmentation feature vector
S_c	Set of curved tunnel segments
S_s	Set of straigt tunnel segments
$\mathcal{F}_s$	Shortest signal path length feature
l	Shortest signal path waypoint count
$\mathcal{G}$	Signal gain
Q	Signal power
$\mathcal{S}$	Signal quality function ground truth
$\hat{\mathcal{S}}$	Signal quality model
t	Time
$\epsilon_r^{(h)}$	Tunnel floor and ceiling permittivity
h	Tunnel height
l	Tunnel length
γ	Tunnel surface reflectivity
Δh	Tunnel surface roughness
θ	Tunnel surface roughness
$\epsilon_r^{(v)}$	Tunnel vertical wall permittivity
w	Tunnel width
$\mathcal{F}_u$	UMAP latent feature vector
$\mathcal{B}$	WLM latent vector
m, n	Waveguide mode indices
λ	Wavelength
W	Waypoint sequence
$\mathcal{W}$	Window in $\mathcal{F}_v$
$\mathcal{F}_w$	Windowing feature vector

Chapter 1
Introduction

This thesis deals with communications in underground environments in the context of mobile robotics. Robotics is principally concerned with a mechanical design of an artificial articulated structure and intelligence that drives the structure through an environment to fulfill the desired task [1, 2]. Mobile robots can operate in large environments according to their traversability limits [3], fulfilling tasks such as exploration, search, inspection, or maintenance. Various locomotion principles can be utilized for ground robots, including wheels [4, 5], tracks [6, 7] or legs [8, 9]. In robotic missions, the robots need to decide where to navigate next using robot routing [10] to perform inspection [11, 12], patrolling [13–16] or exploration tasks [17, 18].

In the robotic exploration, the robot makes its decisions according to the currently perceived environments model [19] using robot localization that can be based on the *Simultaneous Localization and Mapping* (SLAM) [20], where the built model (map) is utilized to provide an estimate on the robot position. Robot navigation is a combination of localization, mapping, and path planning with path execution that thus represents a relatively complex system also regarding needed software components. Here, one can benefit from unified software models such as the ecosystem of the *Robot Operating System* (ROS) [21], which is a middleware with a wide range of available computational modules. Still, specific solutions are needed to implement new research ideas.

The herein-studied topic of communication infrastructure building is motivated by deployments of the robots in communication-denied environments such as underground mining [22]. During mining, a freshly excavated tunnel may collapse, or some mechanical failure may start a fire. Such disasters leave wounded or stunned survivors scattered throughout the tunnels or some technology broken while the mine may still be dangerous for human rescue parties. Hence, robotic *Search-and-Rescue* (SAR) scenarios are among the main motivations in contemporary mobile robotic research [23–25]. In SAR scenarios, a robot is supposed to be deployed in a disaster area or generally dangerous and unknown environment that discourages exposing humans to the risk. The DARPA Subterranean Challenge [26] (SubT), organized in 2018–2021, was an international robotic competition motivated by SAR deployments of mobile robots in underground, communication-denied environments. The competing teams were tasked to design a human-supervised (semi)autonomous robotic system to search an a-priori unknown underground environment for objects of interest under the given time limit. Tunnel, cave, and urban environments have been considered as illustrated in Fig. 1.

(a) SubT NIOSH Tunnel. (b) SubT Urban. (c) SubT Utility Tunnel. (d) Bull Rock Cave [27].

Figure 1: Subterranean environments, courtesy of the CTU-CRAS-NORLAB team.

SubT has been organized into three main events. First, SubT Integration Exercise (STIX) was held in Edgar's gold Mine, in Idaho Springs, Colorado [28] that contains a mixture of historical and modern tunnel sections dug in proterozoic bedrock region [29]. The first scored run of SubT was the Tunnel circuit that took place in the United States National Institute for Occupational Safety and Health (NIOSH) experimental mine of the Pittsburgh Mining Research Division [30]. The site contains horizontal tunnels inside a sedimental limestone-sandstone region [31]. The second scored run was the Urban circuit round held in the unfinished Satsop Nuclear Power Plant [32] representing an urban underground. The Cave circuit has been canceled due to the pandemic; however, the final round, the SubT Finals, consists of all three environment types. The circuit has been built inside a limestone room-and-pillar mine Mega Cavern [33], Louisville, Kentucky. Team solutions are summarized in the special issue articles dedicated to the first two phases of SubT [34]. The main related part of the existing solutions is making the robot reliably communicate with the human supervisor as the radio signal underground attenuates non-trivially. Using pre-installed communication infrastructure was disallowed, and robots had to build the communication infrastructure during the mission to facilitate collaboration and make teleoperation possible.

The problem studied in this thesis is directly motivated by the participation of the CTU-CRAS-NORLAB team in SubT [35], where a problem of communication infrastructure building during the robotic exploration mission is declared. An onboard signal strength prediction model using only limited sensing and computational resources available on the robotic units is required. We[1] primarily target low-bandwidth communication channels using the so-called *breadcrumbs* as deployed retranslation communication motes [35]. The used breadcrumbs technology limits the transmission of the messages in the network to 1 Hz at maximum. Regarding the average speed of the robots, such frequency is too sparse to use the *Received Signal Strength Indicator* (RSSI) for reliable indication of signal availability in complex underground environments. Therefore, we study existing signal propagation models suitable for field robotic hardware and conditions. Based on the existing work, we propose four new models called *Waveguide Linear Model* (WLM), *Variance Windowing Model* (VWM), *Generic Embedding Polynomial Model* (GEPM), and *Evidence Regression Model* (ERM). Besides, we examined two existing baseline methods, the *Free Space Path Loss Model* (FSPL) and its parameterization with attenuation coefficient denoted FSPL-β. On the way to success, we tackled the subproblems of describing variable-length series in a fixed-size vector and separating measurements with a suitable kernel to facilitate the regression task predicting the signal availability. The proposed models have been evaluated using a new dataset gathered along the work on the thesis because, to the best of our knowledge, there was no existing suitable dataset available. The evaluation was conducted using the developed computational framework that supports deploying the prediction models in real-time in autonomous robotic exploration missions. The developed solution deployment in building a chain of radio re-translating stations is demonstrated in the gold mine adit near Jílové u Prahy.

The thesis is organized as follows. The next chapter reviews existing solutions to robotic exploration missions under communication-constrained conditions, including an overview of solutions the teams used in the DARPA Subterranean Challenge. Chapter 3 formally defines the problem we address, which is to support communication infrastructure building in robotic exploration missions. Following the problem statement, we propose a strategy based on the communication signal propagation model in Chapter 4. An overview of existing solutions in Chapter 5 then supports our proposed subterranean signal propagation models introduced in Chapter 6. Chapter 7 describes the dataset used for model verification and evaluation together with implementation details. The evaluation results are reported in Chapter 8 together with the showcase of the real deployment of the developed solution. The thesis is summarized in the conclusion dedicated to Chapter 9.

[1] Following the custom with academic publications, I, the Author, have decided to use *pluralis auctoris* to refer to my original work.

Chapter 2
Communication Constrained Mobile Robot Exploration

In this chapter, we provide an overview of the related work on mobile robot exploration and communication methods. Exploration generally involves collecting data to create a model of phenomena of interest. Concerning the motivational SubT scenario, we consider the exploration a problem of building a spatial model of the environment suitable to reason about possible locations of artifacts to be searched. A mobile robot exploration can be summarized as a repetitive assessment of the currently valid environment model to determine locations where the robot can gain new information, enhancing the model. Thus, an exploration strategy is responsible for determining a sequence of navigation waypoints, a path. The robot is then navigated toward the waypoints with the assumption that the area is explored (covered) by the robot's sensors once the robot follows the path. The expected result of the exploration is a model of the environment created by the robot's sensory system. With a single robot exploration, the communication can support mission monitoring or eventual teleoperation. However, in a multi-robot setup, the robots can exchange their positions and locally created models to improve their decision-making [36]. In communication-denied environments, robots can build the communication infrastructure, serve as communication nodes, or address rendezvous as meeting points, where data can be shared using local communication [37].

The rest of the chapter is structured into the following parts. First, a brief overview of the mobile robot exploration is presented in Section 2.1. Existing communication systems in robot exploration missions are described in Section 2.2. Finally, the context of the CTU-CRAS-NORLAB team solution to the DARPA Subterranean Challenge is summarized in Section 2.3.

2.1 Mobile Robot Exploration

The fundamental work on mobile robot exploration is the frontier-based exploration [38] using occupancy grid maps [39]. The frontier is a free space of the known part of the environment at the boundary of the unknown part of the environment. The idea is that the robot would likely explore an unseen part of the environment while navigating toward the frontiers. Originally, the nearest closed grid cell is classified as the currently pursued frontier while the robot builds a map and localizes itself during the navigation. The localization can be based on the *Iterative Closest Point* (ICP) algorithm [40]; however, the localization and mapping are considered out of the thesis scope. Therefore, the interested reader is referred to existing surveys such as [18, 20, 41–43] to list a few here.

Several follow-up methods have improved the former greedy approach [38]. The authors of [44] compute an expected coverage at frontier grid cells in the *Next-Best-View* fashion [45]. Clustering a set of frontier grid cells by K-means algorithm [46] showed to improve the performance [36] similarly to the using non-myopic decision making based on multi-goal path planning [47]. In 3D environment exploration, it is necessary to address the computational complexity of 3D path planning. For example, the authors of [48] employ Rapidly-Exploring Random Tree [49] to facilitate real-time performance.

Besides frontier-based exploration, information-theoretic approaches have been proposed [50]. The determination of the next navigational waypoints can be based on Kriging such that the variance of the built model is gradually diminished by collecting new measurements. The authors of [19] build a model of the environment together with the traversability model using Kriging based on Gaussian

Algorithm 1: Generic exploration procedure.

```
1 W ← (getRobotPosition())          // Initialize by non-empty tuple.
2 while W ≠ ∅ do
3 |   P_R ← getRobotPosition()      // Current position by localization module.
4 |   Ê ← getBestEnvironmentModel()  // Current model from mapping module.
5 |   W = (P_w^1, ..., P_w^k) ← getExplorationWaypoints(Ê, P_R) // Expl. strategy.
6 |   navigateTowardWaypoints(W)    // Set waypoints for the path follower.
7 terminateMission() // End the exploration as no goals are left to be explored.
```

Process (GP) regression [51]. The exploration procedure can be summarized by Algorithm 1 derived from [52], where the exploration strategy is to determine the navigation waypoints that are then followed by the path following procedure. Note that the exploration procedure is one of the parallel processes of the whole exploration framework. It runs at a lower frequency than processes for localization, mapping, and path following.

In multi-robot exploration, it is necessary to determine which robot will follow which navigational waypoints that can be formulated as the task allocation problem [53]. Depending on communication availability, the multi-robot exploration strategy can be centralized, distributed, or uncoordinated. In the centralized solutions, one entity is responsible for determining which robot shall pursue which waypoint using task allocation methods [53] such as Hungarian algorithm [54] or non-myopic planning using multi-robot, multi-goal planning with cluster-first, route-second heuristic [36]. Distributed exploration strategies can be based on distributed multi-robot task allocation methods [55] using market-based methods with auctions algorithms [56–59].

The MinPos [60] decentralized task allocation for multi-robot exploration is based on the individually computed ranks of the possible exploration goals. The rank is the number of robots closer to the particular waypoint than the robot computing the rank. Each robot is navigated toward the exploration goal with the subjectively lowest rank making the decision completely decentralized. The original rank determination [60] requires sharing the robot positions and individual maps of the robots to compute the shortest paths. However, only robot positions showed to be sufficient using topometric mapping [61]. Hence, the method's advantage is in modest requirements on the communication bandwidth, thus making it suitable for scenarios in communication-denied environments using low-bandwidth communication breadcrumbs.

2.2 Existing Solutions to Communication in Exploration

Communication between two entities can be facilitated by various means. Implicit communication may be used in robotics to infer immediate intentions, yet it is impractical for transmitting high amounts of information [62]. A high-bandwidth tethered link may be used to teleoperate a single robot; however, tethered communication is limited by the reach of the wire [63]. Moreover, when used in the real world, the tether is prone to physical damage by tearing, shearing or breaking. Such damage may occur when laid down, traversed by other robots, or damaged. Therefore, a wireless radio communication medium is preferred.

Radio equipment can be lightweight, mechanically rugged, and versatile [35]. Multiple works addressed robotic mission communication and cooperation [64]. For multi-robot teams with relatively few robots regarding the size of the environment, the robots can deliberately leave communication range and return to it once there is some important-enough information to be transmitted [65]. Thus, as long as there is no reckon upon existing or created wireless infrastructure, robots might need to predict mutual connectivity [17].

A straightforward idea for extending the communications reach is to use a static infrastructure for relaying wireless messages. In urban overground, it can be successfully facilitated via modern cellular technologies [66–68]. However, such infrastructure is not available underground, and we cannot rely on that, specifically in SAR missions. Therefore, the communication infrastructure needs to be built during the mission. Several approaches to ad-hoc communication infrastructure building were presented in DARPA Subterranean Challenge (SubT) that are summarized in the following paragraphs.

The winner team of the SubT Final Event, the Cerberus team [69], built their robotic cooperation on standard Wireless Local Access Network (Wi-Fi) radio technology operating at $5.8\,\mathrm{GHz}$. In particular, the team used off-the-shelf technology based on Rajant BreadCrumb® [70]. Two network devices were present: mesh-capable routers and client access points. Legged robots and operator's base station were equipped with the former, while the drones wielded the latter, less capable but lighter devices. Further, each legged robot carried four deployable mesh-capable devices based on Rajant BreadCrumb® DX2 radio module. The module is furnished with a battery for $2\,\mathrm{h}$ of uptime, foldable antenna, water, shock and dust proof sealed casing, Besides, the module is equipped with a magnetic power switch to prevent operation before deployment and mechanism, making the device stand upright [71]. The authors noted that the resulting signal quality significantly deteriorated when modules landed in a tilted orientation. The technology allowed throughput up to $300\,\mathrm{Mb\,s^{-1}}$, enabling the robots to share odometry, topometry, compressed LiDAR (Light Detection And Ranging) data, and artifact detections and telemetry.

It is intriguing to realize that despite the overall technological sophistication, the breadcrumb deployment strategy was trivial. The Cerberus team resigned from automatic reasoning about when to deploy communication modules and relied solely on the operator's expert decision. In practice, the operator placed the modules such that they formed a communication tree stemming from the base station. During the mission, the robots were allowed to leave the network; when they later realized a need to rejoin the network, they backtracked their recent route until they regained connection.

Similarly, the team CoSTAR [72] used retransmission radios installed in the environment during the mission. However, the team used an unsupervised reactive strategy. A robot deployed a breadcrumb once the signal-to-noise ratio dropped below a certain level, which was known to facilitate good-enough communication quality such that the span of the network was maximized. The robot relied on up-to-date and frequent signal power measurements sustained by heartbeat messages. Even though the strategy leads practically to a tree-like deployed structure, in theory, different network topologies might have been created. For example, an exploring robot can drop a communication node while closing a loop in the environment. The team Explorer based their reactive criterion on a fixed Euclidean distance threshold and a line-of-sight condition [73]. As far as we are concerned, the team CSIRO Data61 [74] used operator expert knowledge.

Besides the SubT effort, extensive research on robotic exploration in a straight uniform tunnel was conducted and summarized by the authors of [75] in addition to surveys [76], and recent [77]. The prime contribution of field deployment reported in [75] is in characterizing signal propagation in the tunnel environment as an instance of an oversized waveguide in a manner useful for robotic missions. Such an environment exhibits nontrivial signal propagation. Most importantly, a systematic damped oscillation pattern can be observed when comparing the signal attenuation to the distance between the transmitter and receiver. The authors conducted precise measurements of the radio operating at $2.4\,\mathrm{GHz}$ with throughput of at most $6\,\mathrm{Mb\,s^{-1}}$. The probability of the message delivery as a function of received signal power was empirically established. The knowledge combined with known spatial attenuation pattern was exploited in [78] where the robots were spaced at a particular distance of around $500\,\mathrm{m}$; indeed, the robots were able to communicate according to assumptions. However, therein presented solution relied on offline measurements and single case-fitted precomputed value of the robot spacing. Nevertheless, the explicit signal propagation modeling approach is rare, and, to the best of our knowledge, it is the first to such an extent.

A pair of robots autonomously measure signal quality in [79] exploring an underlying all-pose-pairs space of possible radio configurations in the Kriging sense. Such a communication map can then be utilized for determining the best locations to place communication nodes. However, it does not support the online building of the communication infrastructure and provides only interpolation of the signal availability, lacking useful predictions outside the traversed area.

2.3 Communication Systems of the CTU-CRAS-NORLAB

The thesis has been pursued within the *Computational Robotics Laboratory* (CRL) [80] that participated in the CTU-CRAS-NORLAB SubT team [35]. Besides, the robotic platforms and sensors available in the *Center for Robotics and Autonomous Systems* (CRAS) [81] have been utilized in the data collection and deployment of the proposed solution. Therefore, a brief description of the team's technological solution to the communication and used platforms is presented.

Two ground robotic platforms have been utilized among the available robotic fleet depicted in Fig. 2. The wheeled Husky A200 platform [4] with the nominal locomotion speed $1\,\mathrm{m\,s^{-1}}$ and possible $70\,\mathrm{kg}$ payload was selected for its ruggedness and tuned control. The quadruped robot Spot® [82] is, however, able to traverse even rough terrain where Husky A200 would fail; its enhanced traversability is payed off by reduced maximum payload of $14\,\mathrm{kg}$ with maximum locomotion speed of $1.6\,\mathrm{m\,s^{-1}}$. The Intel® NUC class computer [83] facilitates computations necessary for exploration [35]. The primary used exteroceptive sensor is Ouster OS0 LiDAR [84] with $35\,\mathrm{m}$ range, 128 row $90°$ vertical field of view at up to $20\,\mathrm{Hz}$ readout frequency, with up to 5.2×10^6 measured points per second.

Figure 2: Robotic fleet of the CTU-CRAS-NORLAB team. Courtesy of CTU-CRAS-NORLAB.

The CTU-CRAS-NORLAB team used three different wireless communication technologies [35]. The first is the UISP airMAX® Bullet™ AC Dual-Band Radio technology [85], used only for testing and local short-range communication. The second is the Mobilicom MCU-30 Lite [86] proprietary radio system operating at $2.4\,\mathrm{GHz}$, which uses precise time division multiplexing to achieve meshing. Thus, it requires a predefined configuration of the network units before the deployment.

Finally, the third type of radio communication technology represents deployable breadcrumbs that are further referred to as motes. Each mote, see Fig. 3a, is based on the RFM69HCW transceiver [87] with the output power of $100\,\mathrm{mW}$ operating configurably either at $868\,\mathrm{MHz}$ or $915\,\mathrm{MHz}$ ISM band. The frequency has been selected because it exhibits better around-corner propagation than higher frequencies [88]. The mote uses a quarter-wavelength whip antenna and frequency shift keying (FSK) modulation schema. Direct measurement of the received power is provided via the internal module circuitry but only after the successful reception of a whole message, which limits the precision of the available RSSI. One lithium-ion type 18650 cell provides the mote with around $16\,\mathrm{h}$ of operation.

Two types of motes are distinguished. Motes intended to be deployed during the robotic mission are sealed in a custom 3D-printed case with a mechanical attachment mechanism that releases it from the holder on demand, see Fig. 3b. These motes are programmed to convey messages by the flood-fill protocol forming an implicit ad-hoc network. Motes lacking the battery and cover serve as access

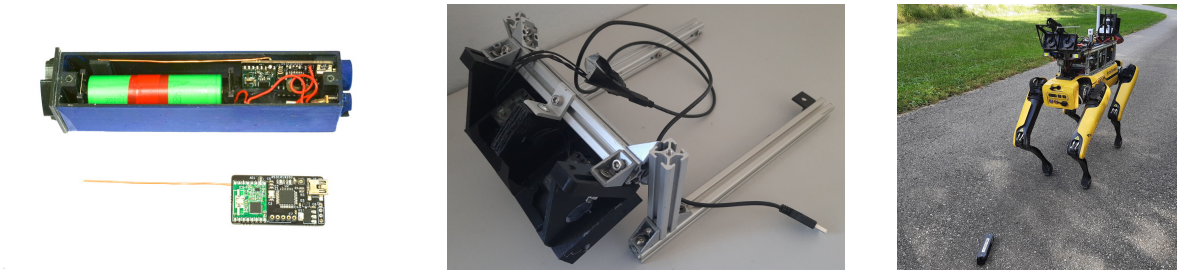

(a) Mote communication module (b) Deployer mechanism (c) Spot® and mote

Figure 3: Motes communication technology used by team CTU-CRAS-NORLAB.

points for robotic units implementing the USB serial communication stack [89] but not participating in the message conveying.

The motes are configured to form an implicit ad-hoc network exploiting a flood fill protocol, where every message is broadcasted with a possible particular intended recipient address. The retranslation happens only once per each source node and each particular message to reduce the network load. Hence, the longest possible round trip of a message in the network with n nodes is n, making the message's lifespan limited yet still keeping it possible to reach any destination in the network. The device only needs to remember the last n messages per each possible network node identification that is limited by the used RFM69HCW chip to 255. Each message can carry $60\,\mathrm{B}$ data payload encrypted via default AES [90] cipher available on the RFM69HCW hardware to provide basic security.

In the CTU-CRAS-NORLAB team participation in SubT, the motes were intended to extend the area where the robots could convey artifact detections and where they can be teleoperated. Each robot has been equipped with the mote, and ground robots have been fitted with up to eight deployable motes as illustrated in Fig. 3c. Like other SubT teams, it was intended to build an ad-hoc tree-like communication structure as the robots reached an edge of communication.

Figure 4: Demonstrator communication infrastructure building mission result based on reactive $1\,\mathrm{Hz}$ RSSI measurements. The background image source: Maps Data: Google ©2023 Landsat/Copernicus.

A snapshot from the motes demonstrator deployment is depicted in Fig. 4. The deployment was reactive using a readout of the available RSSI based on frequent transmitting heartbeat messages from the base station to the robot. Such a strategy would not work in practice because the update of the RSSI is available only when a new message is received. The frequency of message exchange can be up to $1\,\mathrm{Hz}$, which is insufficient, specifically for the robots moving at more than $0.5\,\mathrm{m\,s^{-1}}$. Besides, the RFM69HCW requires around $2\,\mathrm{ms}$ to switch between receiving and transmitting mode, which makes it probable to miss messages in the switch time. Therefore, we asked ourselves for a solution independent of the particular technology to predict signal availability based on the signal propagation modeling and estimation of the expected RSSI and, thus, communication accessibility.

Chapter 3
Problem Statement

The problem addressed in this thesis is to develop a solution to support building a communication infrastructure with m available deployable motes during the exploration mission when the environment is initially unknown. The problem can be formalized as maximizing the covered area, and thus finding the most suitable locations of the motes, $C^\star = (P_1, \ldots, P_m)$, $P_i \in \mathbb{R}^3$ among all possible configurations of motes $C \in \mathbb{C}$, with regard to a given position of the mission operator base station P_{BS}. It can formulate as an optimization problem

$$C^\star = \arg\max_{C \in \mathbb{C}} \mathcal{V}\left(\mathcal{S}^\cup(C, P_{\text{BS}})\right), \tag{1}$$

where $\mathcal{V}$ denotes the volume of a set $\mathcal{S}^\cup(C, P_{\text{BS}})$, the result of *objective signal coverage function* $\mathcal{S}^\cup$, that contains all positions with connectivity to the base station

$$\mathcal{S}^\cup(C, P_{\text{BS}}) = \bigcup_{\{P_i, P_i \in C, G_{\text{C}}(P_i, P_{\text{BS}})\}} \mathcal{S}^*(P_i). \tag{2}$$

The $\mathcal{S}^*$ marks the *one hop coverage function* under the minimum required signal quality $O_{\text{min}} \in \mathbb{R}$ that is considered to be given

$$\mathcal{S}^*(P) = \left\{P' \in \mathbb{R}^3, \mathcal{S}(P, P', \mathcal{E}) \geq O_{\text{min}}\right\} \tag{3}$$

with $\mathcal{S}$ being the *signal quality function* $\mathcal{S} : \mathbb{R}^3 \times \mathbb{R}^3 \times \mathcal{E} \to \mathbb{R}$ depending on the particular environment $\mathcal{E}$, yielding the true signal quality, which is a generalized signal availability measure. G_{C} is the *connectivity relation* defined on the *connectivity graph* $G = (V, E)$ with vertices V and edges E such that, with the abused notation of vertices being associated with the motes locations as $V = C$,

$$(P_i, P_j) \in E \iff P_i \in \mathcal{S}^*(P_j, Q_{\text{min}}) \wedge P_j \in \mathcal{S}^*(P_i, Q_{\text{min}}); P_i, P_j \in C. \tag{4}$$

Thus the relation $G_{\text{C}}(P_a, P_b)$ holds if and only if there is a path between the points in G.

The task would lead to continuous domain high-dimensional optimization in an off-line scenario with known $\mathcal{E}$ and $\mathcal{S}$. However, in the robotic exploration context, the problem has to be solved online, in the way the robot can always communicate with the base station using only a limited number of motes. Besides, a mote, once placed, its positions cannot be further changed. Thus, the problem is to support (in theory any) an exploration strategy such that the robot places the mote when it is necessary to keep the connectivity graph a single connected component. Hence, the problem turns out **to develop a signal availability prediction model** to place the mote as far as possible from the previously placed motes but still within the communication range.

Chapter 4
Proposed Mote Placement Strategy

We propose the strategy to place the mote during the exploration mission so that the placed mote is connected with the operator base station positioned at the location P_{BS} either directly or via already placed motes. Since we aim to enable mote placement with a generic exploration strategy, we assume the exploration procedure summarized in Algorithm 1 to determine a sequence of waypoints $W = \left(P_{\text{w}}^1, \ldots, P_{\text{w}}^k\right)$ toward which the robot is navigated. Besides, we use an environment model $\hat{\mathcal{E}}$ built during the exploration mission.

We assume the robot is initially placed within the communication range of the base station P_{BS} in the sense of the connectivity relation $G_{\text{C}}(P_{\text{R}}, P_{\text{BS}})$. If the robot leaves the communication range, a mote needs to be placed, extending the connectivity to the base station. To this end, the robot maintains a set of so-far placed mote positions $C = \{P_{\text{BS}}, P_1, \ldots, P_m\}$ including also the base station position P_{BS}, which is initially the only element. The robot asks if there is a sufficient signal strength among the waypoints W to any of such mote $P_i \in C$. Specifically, the robot chooses the farthest waypoint to maximalize the resulting covered area.

In general, the signal availability depends on the environment and is determined by the true signal quality function $\mathcal{S}(P_{\text{tx}}, P_{\text{rx}}, \mathcal{E})$ with the minimum required signal quality O_{min}. However, the true signal quality is unknown unless the robot travels to the position of interest and measures the signal; we regard such action as infeasibly costly. That is why the robot uses the onboard signal availability model $\hat{\mathcal{S}}(P_{\text{tx}}, P_{\text{rx}}, \hat{\mathcal{E}})$ to predict the expected signal quality at any radio position pair, using the current perception of the environment $\hat{\mathcal{E}}$.

We propose to adjust Algorithm 1 by selecting the farthest location $P_{\text{w}}^* \in W$ for which

$$\hat{\mathcal{S}}(P_{\text{w}}^*, P^i, \hat{\mathcal{E}}) > O_{\text{min}} \wedge \hat{\mathcal{S}}(P^i, P_{\text{w}}^*, \hat{\mathcal{E}}) > O_{\text{min}}$$

holds with any known deployed radio $P^i \in C$. The robot navigates towards P_{w}^* using precedent waypoints, discarding the following. Upon arrival, new exploration waypoints are retrieved, and the expected signal quality is determined. If no waypoint promises sufficient signal quality, the robot places the mote at the current location and recomputes the signal quality. Then the exploration is resumed, and the procedure repeats until the environment is explored. As long as the signal propagation model $\hat{\mathcal{S}}$ provides good predictions

$$\forall P_{\text{tx}} \in \mathbb{R}^3, P_{\text{rx}} \in \mathbb{R}^3 : \hat{\mathcal{S}}(P_{\text{tx}}, P_{\text{rx}}, \hat{\mathcal{E}}) > O_{\text{min}} \iff \mathcal{S}(P_{\text{tx}}, P_{\text{rx}}, \hat{\mathcal{E}}) > O_{\text{min}},$$

the placed mote is connected to the base station P_{BS} via C which follows from the induction rule. The proposed mote placement strategy within the exploration procedure of Algorithm 1 is summarized in Algorithm 2, where the main part of the mote placement is added as Lines 7–19.

Assuming a model of the signal availability is given, the proposed strategy provides an automated placing of communication motes during the exploration mission without relying on insufficient real-time signal quality data. However, if the model mispredicts the signal quality, the resulting true signal quality deteriorates, possibly even to the loss of communication altogether, breaking the communication chain. The signal quality model $\hat{\mathcal{S}}$ is thus of the utmost importance. Specifically, if $\hat{\mathcal{S}}$ would predict a higher signal quality than in reality, the mote would be placed without connectivity to the base station. Therefore, we further focus on the problem of signal quality modeling and its predictions.

Algorithm 2: Proposed mote placement strategy.

Input: P_{BS} - Position of the base station.
Parameter: m - Number of available motes.
Parameter: O_{min} - Desired minimum signal quality.

$C \leftarrow \{P_{\text{BS}}\}$ // The set of positions of known radios.
$W \leftarrow$ (getRobotPosition()) // Initialize by non-empty tuple.
while $W \neq \emptyset$ **do**
  $P_{\text{R}} \leftarrow$ getRobotPosition() // Current position by localization module.
  $\hat{\mathcal{E}} \leftarrow$ getBestEnvironmentModel() // Current model from mapping module.
  $W = \left(P_{\text{w}}^1, \ldots, P_{\text{w}}^k\right) \leftarrow$ getExplorationWaypoints($\hat{\mathcal{E}}$,P_{R}) // Expl. strategy.
  if $|C| \leq m$ **then**
    $P_{\text{w}}^* \leftarrow \emptyset$ // Seek the farthest waypoint with the connectivity.
    foreach i in $1 \ldots k$ **do**
      foreach P^j in C **do**
        if predictSignalQuality($P_{\text{w}}^i, P^j, \hat{\mathcal{E}}$) $\geq O_{\text{min}}$ **and**
         predictSignalQuality($P^j, P_{\text{w}}^i, \hat{\mathcal{E}}$) $\geq O_{\text{min}}$ **then**
          $P_{\text{w}}^* \leftarrow P_{\text{w}}^i$ // Update the farthest waypoint with connectivity.
          break // Connectivity to any known radio suffices.
    if $P_w^* == \emptyset$ **then**
      placeMote(P_{R}) // Place mote at P_{R}.
      $C \leftarrow C \cup \{P_{\text{R}}\}$ // Update the set of deployed radios.
      $W \leftarrow (P_{\text{R}})$ // Request a new determination of the exploration waypoints.
    else
      $W \leftarrow (P_{\text{w}}^1, \ldots, P_{\text{w}}^*)$ // Filter out waypoints without connectivity.
  navigateTowardWaypoints(W) // Set waypoints for the path follower.
terminateMission() // End the exploration as no goals are left to be explored.

In a robotic mission, the concern of communication availability lies in the probability of successful message delivery. We follow the work [78] that asserts a measurable and assessable relationship between the packet delivery probability and the received signal power. The received signal power measurement is a standard hardware feature of wireless systems, which we consider more suitable than a packet loss rate. Measuring the message loss rate requires knowing the number of messages to be received, which is tricky in a robotic mission. Therefore, we assume the probability is known and focus on modeling the received signal power Q_{rx}.

Now assume that we know the nominal transmitted signal power Q_{tx} in advance, such as the setup of the communication device. Then, we can model the signal gain $\mathcal{G}$ in the logarithmic units of decibels dB as

$$\mathcal{G}(P_{\text{tx}}, P_{\text{rx}}, \mathcal{E}) = Q_{\text{tx}} - Q_{\text{rx}}, \tag{5}$$

given the radio positions P_{tx} and P_{rx} in an environment $\mathcal{E}$, where negative values of $\mathcal{G}$ denotes the signal attenuation. We can further assume that the exploration framework provides a model of the environment $\mathcal{E}$. Hence, we may focus on the signal gain (attenuation) modeling instead of message reception probability, as the former is supported by the rich electromagnetic field theory overviewed in the following chapter.

Chapter 5
Theory and Modeling of Radio Signal

A brief theoretical background to signal propagation is provided in this chapter to support the selected solutions for signal availability prediction. The radio signal is a dynamic electromagnetic field that conveys information encoded in amplitude, frequency, and phase of the underlying harmonic field variations. Signal power and its ratio to the highest noise component are of particular interest since they determine whether the signal can be correctly received and interpreted. The electromagnetic fields that carry the signal can be characterized by Maxwell's equations [91]; at any time, any electromagnetic field can be described by a solution of these equations. Since the full general equations are too complex for many practical cases, researchers considered specific assumptions leading to simplifications that sufficiently describe the signal propagation in the reduced domain [76]. One such approach is based on the waveguide theory that matches our domain of propagation in underground environments. We also provide an overview of existing statistical and data-driven signal propagation models that disregard the physical nature but still provide useful predictions corresponding to real observations and measurements.

5.1 Electromagnetic Field Theory and Simplified Models

Maxwell's theory of electromagnetic field [91] describes principles of electric charges, magnetic forces, and related phenomena. The theory may be formulated in several ways; as an illustration, we provide a formulation using physical quantities of electric field E, volumetric electric charge density ρ, magnetic field B, and electric current density j. The quantities are related together with four differential equations, namely Gauss law

$$\nabla \cdot E = \frac{\rho}{\varepsilon_0 \varepsilon_r}, \tag{6}$$

Gauss law for magnetism

$$\nabla \cdot B = 0, \tag{7}$$

Faraday's law of induction

$$\nabla \times E = \frac{-\partial B}{\partial t}, \tag{8}$$

and Ampère's circuital law

$$\nabla \times B = \mu_0 \mu_r \left(j + \varepsilon_0 \varepsilon_r \frac{\partial E}{\partial t} \right). \tag{9}$$

The symbol ε_0 denotes the permittivity of vacuum, ε_r is relative permittivity, μ_0, and μ_r are respective magnetic permeabilities, while t stands for time. The symbols $\nabla\times$ and $\nabla\cdot$ denote the operations of rotation and divergence, respectively. Our robotic mission is concerned with a power received at a distance from the source of the electromagnetic field in a volume with some distribution of ε_r and μ_r. Poynting vector is a power spatial density measure that can be expressed using vector product $\times$ as

$$Q = E \times \frac{1}{\mu_0} B, \tag{10}$$

in the case of materials with no polarization or magnetization.

Solving the equations can produce a specific distribution of all concerned quantities in time and space. However, the analytic solution to the equations is not available. Furthermore, it is impossible to describe the particular environment in the robotic missions in terms of the equations' parameters. Direct numerical solutions are also not straightforward. The wavelength of the electromagnetic waves is about $34\,\mathrm{cm}$ for the communication frequency around $868\,\mathrm{MHz}$. Following Shannon's sampling theorem [92], we would need a grid with a resolution of $17\,\mathrm{cm}$ or lower to represent the modeled phenomena properly, which means the relative permittivity and respective permeabilities. Furthermore, the environment might exhibit significant geometry features at a smaller scale, leading to further necessary model refinement. For a possible spatial discretization of the mission area about $1000\,\mathrm{m} \times 1000\,\mathrm{m} \times 50\,\mathrm{m}$ large, the footprint is expected at least $2.5\,\mathrm{GB}$, which would be too demanding to adequately identify all the parameters. Besides, the available exteroceptive sensors on the robots perceive only transparent atmospheric volumes, such as LiDAR. Assessment of the material properties is impossible using common exteroceptive sensors.

Handling the precise material properties is neglected by assumptions about the environment leading to specific signal propagation models. The elementary model uses the maximum radio range method as in [93]. Such a model is suitable for simple laboratory scenarios such as Kilobots [94] with the infrared ground-directed low-power communication channel. The model yields a prediction of signal availability based on the distance between the transmitter and receiver. The line-of-sight model [95] assumes that a radio link exists as long as the transmitter and receiver can be connected by a line that does not intersect any obstacle. The fixed radius and line-of-sight are used for maintaining the connectivity of aerial vehicles in exploration missions in [96].

In environments without obstacles, it can be assumed that the signal propagates evenly in all directions. Then, the signal gain[2] can be described by Friis' formula [97]

$$\underbrace{Q_{rx} - Q_{tx}}_{\text{gain } \mathcal{G}} = \underbrace{\mathcal{G}tx + \mathcal{G}_{rx}}_{\text{circuitry gain}} + \underbrace{D_{tx} + D_{rx}}_{\text{alignment gain}} + \underbrace{20\beta \log_{10}\left(\frac{\lambda}{4\pi d}\right)}_{\text{environment gain}}, \tag{11}$$

where λ is the signal wavelength, d is the distance between the transmitter and receiver, and $\beta \in (0, 1)$ is the gain coefficient. Q_{rx} and Q_{tx} are the received and transmitted power, respectively, and their difference is the total signal gain that is measured in the logarithmic units of decibels (dB). The gain comes from three main sources. Internal circuitry and manufacturing imperfections may cause power depletion even before the signal becomes airborne. Moreover, since antennas may transmit the signal non-uniformly, the misalignment of the transmitter and the receiver results in additional power loss. Finally, as the signal travels from its source, the surface of the wave sphere grows quadratically with the distance d, resulting in an environment-induced gain.

In environments with obstacles, such as in urban scenarios, the state-of-the-art methods [98, 99] attempt to explicitly describe electromagnetic phenomena such as signal scattering, reflections, multipath propagation, or shadowing. Existing models extend the concept of Friis' formula (11) by adding abstraction terms to characterize building surface distribution [100], Earth propagation loss, or tropospheric refraction. Enumerating the signal propagation as a stochastic process is also possible using Gilbert-Elliot packet loss model [101]. However, such methods are valid only in specific scenarios, limited to terrestrial broadcasting.

The class of approaches based on the raytracing principle known from computer graphics relies on a knowledge of the precise geometric environment models. A set of optical rays is simulated from a signal source according to the radiation pattern; then, it is investigated how many rays reach a recipient antenna [102]. However, with each ray's collision with an uneven surface, a stochastic reflective ray multiplication needs to be simulated, leading to an explosion of computational demands. On the other

[2]Note that, in our case, the signal gain negative as the signal attenuates.

hand, the multipath propagation phenomenon is implicitly included. Parabolic vector equations model only a specific cone of radiation space under a paraxial approximation assumption [103] that is shown to provide a trade-off between the verbosity of the raytracing method and succinctness of former models. The method was used in urban [104] and subterranean [105, 106] scenarios, but it relies on precise geometric and material descriptions of the environment, such as wall permittivity. The major principal shortcoming of the raytracing methods is sensitivity to inaccurate or biased input data that makes it unsuitable for mobile robots with limited onboard resources and limited sensing.

Regarding our mobile robotic setup, a precise model for the computation of anticipated signal power suitable for onboard deployment is required. We reject the verbose raytracing models or direct numerical simulations for two reasons. First, their inherent significant demands on calculations imply that they cannot be supported on limited onboard computers. Second and more importantly, the models require a precise notion of material properties, such as material permittivity or permeability which cannot be directly provided online with contemporary onboard sensory. Following the work of [75] and [88], the signal propagates underground nontrivially and non-monotonically with distance. We need more informed models to exploit some systematic features of signal propagation than the basic ones based on range and line-of-sight criteria. The model may be limited to the specific domain of subterranean environments. We thus seek a set of assumptions that would make the free parameters determinable and the model computable onboard.

5.2 Waveguide Theory

In rough underground environments, the signal scatters by reflections and refractions from uneven surfaces. Besides, ambient humidity and soaked walls become partial conductors worth considering. Such a scenario is generally known as a waveguide, and it is elaborated upon in several works overviewed in [107–109]. In general, waveguides satisfy Maxwell's equations only in discrete solutions known as waveguide modes; thus, an electromagnetic wave can propagate only via such modes. Waveguide theory is widely applied in integrated circuit design or optic fibers. In our case, we are interested in a category of oversized waveguides where the signal wavelength is significantly smaller than the waveguide's cross-sectional dimension.

The authors of [110] and [111] note that in tunnels, the signal may be considered as a wave propagating predominantly in mode $(1, 1)$. The tunnel is classified into two types of tunnel segments, the uniform straight segments S_s and uniformly curved segments S_c. As long as radios are farther than the first Fresnel zone limit q^2/λ, where q is the distance to the nearest obstacle, the total environment-induced gain along a complex path can be expressed as

$$\mathcal{G} = \sum_{i \in 1 \ldots |S_s|} (\mathcal{G}_i^s) + \sum_{j \in 1 \ldots |S_c|} (\mathcal{G}_j^c), \tag{12}$$

where $\mathcal{G}_i^s$ is the gain for the i-th straight section and $\mathcal{G}_j^c$ is the gain in the j-th curved section, both terms in decibels dB. The gain along a straight line segment can be then expressed as

$$\mathcal{G}_i^s = l_i \frac{\ln 10}{20} \frac{\lambda^2}{2} \Bigg[\underbrace{\frac{\pi^2 \Delta h_i^2}{\lambda} \left(\frac{1}{w_i^4} + \frac{1}{h_i^4} \right)}_{\text{roughness gain}} + \underbrace{\frac{\pi^2 \theta_i^2}{\lambda^3}}_{\text{tilt gain}} + \underbrace{+ \begin{cases} \frac{\epsilon_r^{(h)} (m+1)^2}{w_i^3 \sqrt{\epsilon_r^{(h)} - 1}} + \frac{(n+1)^2}{h_i^3 \sqrt{\epsilon_r^{(v)} - 1}}, & \text{horizontal mode} \\ \frac{(m+1)^2}{w_i^3 \sqrt{\epsilon_r^{(h)} - 1}} + \frac{\epsilon_r^{(v)} (n+1)^2}{h_i^3 \sqrt{\epsilon_r^{(v)} - 1}}, & \text{vertical mode} \end{cases}}_{\text{modal gain}} \Bigg], \tag{13}$$

where l_i is the length of the segment with a uniform width w_i and height h_i, $\epsilon_r^{(v)}$ is the relative permittivity of the side walls, $\epsilon_r^{(h)}$ is the relative permittivity of the ceiling and floor, λ is the signal wavelength, Δh is the wall roughness (computed as an average deviation from the local mean wall level), θ is the tilt of the section (an average angular offset from the long-distance meandering tunnel [rad]), and m and n are the indices of the dominant mode of propagation. The terms that depend on Δh and θ approximate the loss induced by scattering the energy carried in the mode $(m, n) = (1, 1)$ to different modes and directions.

They propose a ray-based approach to determine gain induced by reflections and refractions if the tunnel is bent. In the uniformly curved segments, the rays are assumed to enter the curve collimated and parallel to the incident straight tunnel centerline. Hence, the number of reflections, together with the induced partial loss, is estimated as

$$\mathcal{G}_j^c = l_j \frac{1}{|R_j|} \sum_{x' \in R_j} \underbrace{\frac{20}{2\sqrt{r_j^2 - (x' - r_j)^2}}}_{\text{\# reflections}} \log_{10}(\gamma_j \exp(\square)),$$

$$\square = \underbrace{\frac{-8\pi^2 \Delta h_j^2 \sin^2\left(\arctan\left(\frac{\sqrt{r_j^2-(x'-r_j)^2}}{r_j - x'}\right)\right)}{\lambda^2}}_{\text{roughness by grazing angle}} \tag{14}$$

where γ is the standard reflectivity coefficient, and R is a set of distances between the edge and the individual evenly spaced rays entering the bend. Besides, if a junction occurs along the path, all outbound branches are ignored as if there was a solid wall.

The approach reduces the environment characterization to a handful of parameters as opposed to original continuous distributions of ϵ_r and μ_r by assuming homogeneous material distribution and rectangular tunnel cross-section profile along each tunnel segment length. We consider it advantageous that the environmental parameters have a physically relevant interpretation. As the properties $w, h, \Delta h, \theta$ are concerned with relatively simple geometrical features of the environment interior, an automatic method of their determination from spatial exteroceptive sensors might be possible. Parameters $\epsilon_r^{(v)}$ and $\epsilon_r^{(h)}$ may be determined before the robotic mission as its value is considered constant in the environment. The method provides a closed-form solution to signal gain modeling relying on observable parameters, which we consider suitable for our robotic mission.

5.3 Data Driven Models

Data-driven methods simplify the underlying physics and exploit generalization and machine-learning techniques to capture the nature of the electromagnetic fields implicitly. A thorough survey can be found in [112], and thus we focus on approaches most relevant to robotic scenarios. The authors of [113] characterize an environment by features such as line-of-sight visibility, obstacle obscuration, and ground reflection, which are used in a neural network that achieves a gain prediction absolute error of about 10 dB. Although possible, the approach cannot explain signal propagation in terms of physical quantities and principles, relying solely on machine learning.

A purely probabilistic model for signal characteristics estimation is presented in [114]. The work further provides mathematical reasoning about the predictability of the communication parameters. However, since their model lacks an explicit environment model, it cannot infer the gain. Besides, it always needs some prior measurements in the area of interest.

In [115], an evidence grid of the signal availability, called a communication map, is built. The approach utilizes a spatial *Gaussian Process* (GP) [51] that interpolates samples of communication

link quality, yielding the most likely value together with its confidence. Consequently, the GP-based model can be utilized in active perception tasks such as [116]. The environment may be thus captured with arbitrary resolution as it is a matter of sampling in $\mathcal{O}\left(n^4\right)$ to capture all pairs of radio locations in a 2D area. Even though there are efforts to sample the whole space [115, 117], such a task is not only practically demanding but also limited to interpolation only. Our former work on machine learning approach to signal availability prediction is presented in [118], where we examine the generalization of Friis' formula to consider environment abstraction in a data-driven fashion by a feature vector descriptions similar to [113]. Therein presented results support the feasibility of the approach while providing better RSSI prediction in the extrapolation setup compared to [115].

The data-driven methods are a valid way of signal propagation modeling as they adjust to different environments without any fixed assumptions making them possibly more generic. The models either rely on some scheme of interpolating training data, which themselves serve as the model's free parameters, or on some regression task that extracts anonymous latent parameters. The prediction accuracy of the methods can be generally adjusted by setting the number of those latent parameters. However, the lack of physical interpretation of the latent parameters does not contribute to model explainability.

5.4 Discussion of Existing Signal Propagation Methods

The addressed problem of signal coverage extension by mote placement during a mobile robot exploration mission was reduced to signal propagation modeling by fixing the mote placement strategy. In the proposed strategy, the signal quality needs to be predicted in regions where the robot has not been before, which follows from utilizing the waypoints toward the exploration goal provided by the exploration oracle. That is why the signal propagation modeling needs to extrapolate the signal quality in observed yet unvisited areas precisely.

Based on the review of the existing signal propagation modeling work, we propose combining the benefits of the model-based and data-driven approaches. We consider the oversized waveguide approach [110] to be the most promising among reviewed physically motivated methods with regard to onboard computability. The model assumes that the environment may be sufficiently characterized by simple local geometrical features such as corridor width or height, which can be computed from common onboard exteroceptive sensors. Hence, the challenging identification of the environmental parameters is categorically facilitated as opposed to verbose approaches. The closed-form solution makes the method computationally efficient. However, in practice, the model's assumptions are scarcely fulfilled as the tunnel cross-section is not always rectangular. That is why combining generalized approaches with physically relevant features seems a good idea. We extend the idea of the linear model to build an unconstrained polynomial descriptor of the tunnel geometry used in the linear signal strength regression to address the drawback. Also, a regression approach based on [51] is examined as it already exhibited supreme extrapolation capabilities.

Chapter 6
Proposed Signal Propagation Models

Four proposed models of signal gain suited for subterranean environments are presented in this section to support the robotic exploration strategy defined in Chapter 4. First, we focus on the waveguide formulation [110] in the proposed *Waveguide Linear Model* (WLM). We show that the original work can be reformulated to a linear equation in unknown environment properties, making the subsequent computation efficient. Moreover, given samples of signal measurements, the proposed formulation forms an overdetermined linear equation system that can be solved in the least squares sense, exposing values of environment properties. In practice, however, the assumptions of the WLM are hardly strictly followed. That is why we have sought to extend the approach. The proposed *Variance Windowing Model* (VWM) exploits the intuition behind the linear gain model by assessing the elementary gain contribution of equally spaced signal segments.

The *Generic Embedding Polynomial Model* (EGPM) abstracts the physical meaning by establishing an anonymous latent space embedding between the input data and regression, yet still keeping the efficient linearity. Finally, we generalized the data-driven processing proposed in [115] by abstracting environment properties with two-dimensional explicit feature vectors to facilitate spatial extrapolation [118]. The model is named *Evidence Regression Model* (ERM), and it improves the extrapolation capabilities over the [115]. Still, because it is data-driven, it does not support physics-related reasoning about its performance. All presented models commonly use the shortest signal path distance as a regression parameter either explicitly or implicitly, extending it with some added environment characterization. Sections 6.2 to 6.5 describe the proposed models.

All the models follow the same key idea of [118] to describe the tunnel geometry by local geometrical features such that the subsequent regression is performed over those features. The model's input query takes a form of a three-tuple $(P_{tx}, P_{rx}, \hat{\mathcal{E}})$ of the transmitter position P_{tx}, receiver position P_{rx}, and the current model of the environment $\hat{\mathcal{E}}$. Models can use various methods of environment abstraction into a descriptive numerical representation. A particular interest is taken in the methods being dependent only on local environment features, producing similar predictions in similarly perceived parts of the environment regardless of the reference frame to support spatial extrapolation. Then, the models use the environment abstractions for predicting the signal subsequently. The proposed environment characterizations are detailed in Section 6.1.

The proposed models share the following assumptions. First, we assume that the radio device is only described by its frequency and transmission power. Technical details like possible circuit-induced power loss are disregarded as they can be enumerated independently in laboratory assessments. Second, we assume that omnidirectional antennas are used, and they are always oriented vertically to decrease the number of free parameters. Different antenna orientations would lead not only to misalignment power loss but also possibly to anisotropic signal propagation in the environment, which we chose to disregard for the purpose of the thesis. Therefore, only the antenna positions are of interest to us. Further, we limit the models to a single frequency (heeding only the mote measurements at $868\,\mathrm{MHz}$) such that we may disregard signal propagation dependence on frequency while still keeping the predictions useful for the intended robotic mission. Besides, we assume that the environment where the signal propagates is static up to the single robot and motes which traverse it. The mass of the robot is assumed to have zero impact on the signal propagation by placing the antenna in a suitably detached place on the robot.

6.1 Environment Model and Geometric Features

According to the literature review about the waveguide theory in Section 5.2, the environment geometry is the dominant regression parameter. An automatic method for extracting geometry properties of an area between the investigated radio positions is necessary for model learning and regression to be useful in a mobile robotic mission. We use the available exploration framework [61] with occupancy grid map building [119] to provide us with the environment model $\hat{\mathcal{E}}$, which is a 3D grid map with a resolution of $5\,\mathrm{cm}$. Given two locations $P_{tx} = (t_x, t_y, t_z)$ and $P_{rx}(r_x, r_y, r_z)$, we are interested in describing the space along the path connecting the locations with a geometry feature vector $\mathcal{F}$. Multiple variants of the feature vector are considered.

First, we use Euclidean distance between the locations

$$\mathcal{F}_l = \|P_{tx} - P_{rx}\|^2 \tag{15}$$

as the basic relative measure. However, in subterranean environments, the signal propagation is constrained by abundant mass that directs the signal into sparse free space by the waveguide principle. Therefore, we use *Signal Shortest Path* length feature $\mathcal{F}_s$, computed as follows.[3]

The 3D grid map is segmented into walls and floor/ceiling using clustering with the assumption of walls being aligned to the vertical axis and floor/ceiling to the horizontal axis. A distance transform is generates a cost field that decreases proportionally with the distance from the walls (obstacle). Based on the cost field, the shortest signal path between assigned radio positions is determined as a sequence of waypoints $(P^1_{\mathrm{w}}, \ldots, P^l_{\mathrm{w}})$ using the planning method [119]. The waypoints are aligned with the underlying grid cell centers, resulting from planning on a planar grid with 8-neighborhood; see examples depicted in Figs. 5a and 6. The length of such a signal path can then be expressed as

$$\mathcal{F}_s = \sum_{i=2}^{l} \|P^{i-1}_{\mathrm{w}} - P^i_{\mathrm{w}}\|^2, \tag{16}$$

where P^i_{w} is the i-th waypoint location and l is the number of waypoints.

The 3D grid map is further utilized to sample local geometry properties along the signal path to provide regression parameters for the proposed signal gain models. For each waypoint, its projections to the closest floor and ceiling clusters are determined; the summed distances from the waypoint of the two projections comprise the height P^j_h of the corridor. The width P^j_w is then based on the value of the cost field. The Fig. 5a illustrates the described process. Further, the waveguide model in Section 5.2 relies on the knowledge of the tunnel's curvature, which is determined as follows.

We furnish each waypoint with two measures of the local tunnel curvature determined as illustrated in Fig. 5b. First, we measure an angle P^j_α at each waypoint as the smaller angle it forms with its two neighboring waypoints. Second, we compute P^j_r as the radius of the smallest sphere that would pass through the waypoint and its two neighboring waypoints using the cost field. All the measured features are further smoothed by $1\,\mathrm{m}$ sliding average window. Each signal gain model query $(P_{tx}, P_{rx}, \hat{\mathcal{E}})$ is thus provided with $P^j_{\{w,h,\alpha,r\}}$ organized as the *Geometry Describing Variable-Length* feature vector

$$\mathcal{F}_v = \begin{pmatrix} P^1_w & P^1_h & P^1_r & P^1_\alpha \\ P^2_w & P^2_h & P^2_r & P^2_\alpha \\ & & \vdots & \\ P^l_w & P^l_h & P^l_r & P^l_\alpha \end{pmatrix}. \tag{17}$$

The feature vector size depends on size of the path l between the transmitter and receiver, which is generally different with each model query. Therefore, we propose three methods to characterize the variable-length geometry properties along the path to enable its usage in the regression methods.

[3] The implementation of operations over the 3D grid map was kindly provided by Jan Bayer.

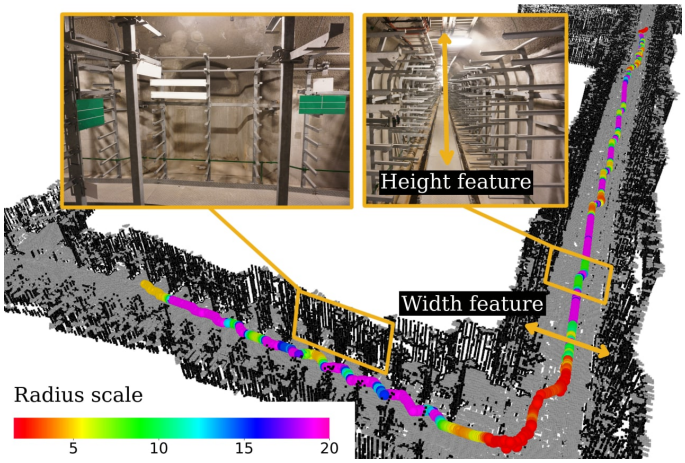

(a) Render from the environment geometry sampling framework, courtesy of Jan Bayer. The colored line depicts the local curvature computed as radius r at each waypoint; width, height, and an angle α are computed per each waypoint but not shown in this figure.

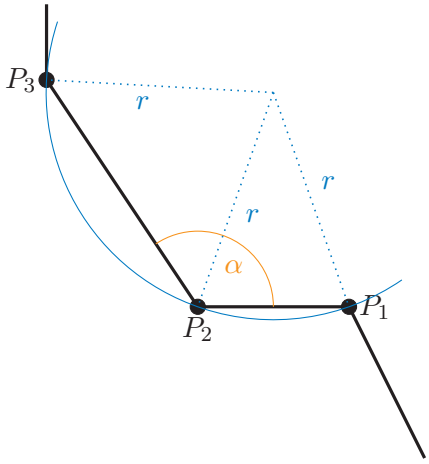

(b) Relation of curvature metrics radius r defined by a circle fitted through neighboring points $P_{1,2,3}$ and angle α held by the points.

Figure 5: Geometry features computation.

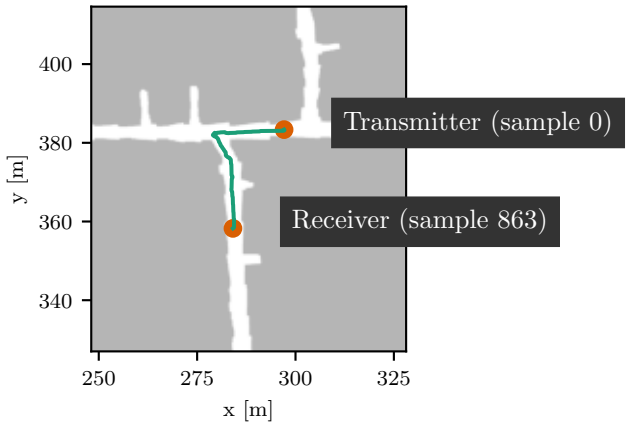

Figure 6: Shortest signal path as computed in the environment occupancy grid. Environment characterization along the signal path using the proposed segment-based characterization is depicted in Fig. 7 and windowing-based characterization in Fig. 8.

The method described in Section 6.1.1 implements the idea presented in [110] that is based on clustering the tunnel between investigated radio positions into segments of uniform geometries. A generalization of the method that considers overlapping equally-sized path segments called windows is presented in Section 6.1.2. A method based on histogram encodes the variable-length feature vector $\mathcal{F}_v$ into a fixed-size vector while preserving signal length information, briefly summarized in Section 6.1.3. Further, the occupancy feature supporting the ERM is described in Section 6.1.4.

6.1.1 Segment-based Characterization

The model based on waveguide theory (12) proposed in [110] includes environment geometry characterization as a parameter that describes a connected portion of the tunnel where the geometry fluctuation is small. The original work [110] does not provide an exact method of determination of the segments; hence an interpretation was devised as follows.

We propose identifying parts (called segments) of the shortest signal path by automatically detecting significant steady-state changes among values of the assignment's feature vector $\mathcal{F}_v$. The steady-state value changes are determined separately for each f-th column of $\mathcal{F}_v$ denoted $\mathcal{F}_f$ as

$$\check{\mathcal{F}}_f = \mathcal{F}_f - \overline{\mathcal{F}_f}, \tag{18}$$

where $\overline{\mathcal{F}_f}$ denotes the arithmetic mean of the values P_f^i in the column $\mathcal{F}_f$,

$$\overline{\mathcal{F}_f} = \frac{1}{l}\sum_{i=1}^{l} P_f^i. \tag{19}$$

$\check{\mathcal{F}}_f$ is then normalized by the maximum absolute value of the column

$$\hat{\mathcal{F}}_f = \frac{\check{\mathcal{F}}_f}{\max_{i=1}^{l} |P_f^i|}, \tag{20}$$

and convolved with a step vector $\mathcal{V} = (\mathcal{V}^1, \ldots, \mathcal{V}^{2l-1})$, where

$$\mathcal{V}^i = \begin{cases} -0.5 & \text{if } i \leq l \\ +0.5 & \text{otherwise} \end{cases}, \tag{21}$$

as

$$\tilde{\mathcal{F}}_f = \hat{\mathcal{F}}_f * \mathcal{V}. \tag{22}$$

A set of indices $\check{\mathcal{F}}_f = \left\{q_f^1, \ldots, q_f^p\right\}$ is determined such that $\tilde{P_f^{q^i}} \in \tilde{\mathcal{F}}_f$ is the topographic peak in $\tilde{\mathcal{F}}_f$ with $5\,\%$ prominence and at least 50 samples apart from another. Then, sorting the union of all l indices among all $\mathcal{F}_v$ columns

$$\dot{\mathcal{F}}_v = (\dot{q}_1, \ldots, \dot{q}_l), \quad \dot{q}_i < \dot{q}_{i+1}, \quad \dot{q}_i \in \{0, l\} \cup \left(\bigcup_{f \in \{w,h,r\}} \check{\mathcal{F}}_f \right) \tag{23}$$

defines the resulting segment values as 4-tuple

$$\mathcal{T}^i = \left(\text{med}\left(P_{\dot{q}_i}^w, \ldots, P_{\dot{q}_{i+1}}^w\right), \text{med}\left(P_{\dot{q}_i}^h, \ldots, P_{\dot{q}_{i+1}}^h\right), \text{med}\left(P_{\dot{q}_i}^r, \ldots, P_{\dot{q}_{i+1}}^r\right), \mathcal{T}_d^i\right), \tag{24}$$

where med is the median of a given sequence, $\mathcal{T}^i$ is the i-th segment and $\mathcal{T}_d^i$ is the segment length computed as

$$\mathcal{T}_d^i = D(i+1) - D(i), \quad D(j) = \sum_{i=1}^{j-1} \|P_{\text{w}}^i - P_{\text{w}}^{i+1}\|^2 \tag{25}$$

Note that we omit the curvature angle feature because it is not considered in the source work [110]. A *Segmentation* feature vector $\mathcal{F}_g$ is then constructed by stacking the segments into the matrix

$$\mathcal{F}_g = (\mathcal{T}_d^{1\intercal}, \ldots, \mathcal{T}_d^{l+1\intercal})^\intercal. \tag{26}$$

The proposed segmentation method is illustrated in Fig. 7.

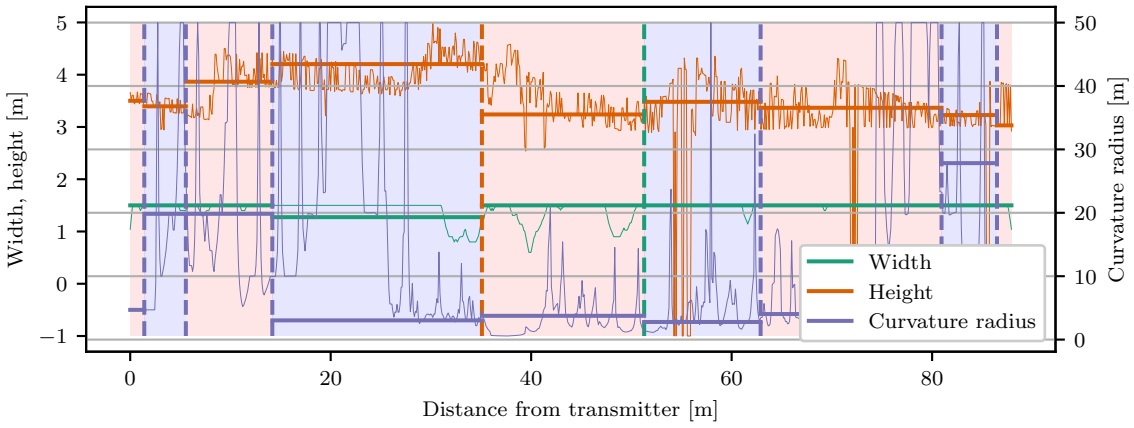

Figure 7: Segment-based characterization. Interleaving red and blue regions denote individual segments found on the given input feature vector $\mathcal{F}_v$ (thin lines) with the resulting segment mean values denoted by thick horizontal lines. Dashed vertical line colors represent the $\mathcal{F}_v$ component that caused the corresponding segment split. The illustrated Example for the same shortest signal path as visualized in Fig. 8 with one 90° curve depicted in Fig. 6.

6.1.2 Windowing-based Characterization.

A windowing scheme is proposed to expose local variations in the tunnel geometry granularly. Let the i-th window $\mathcal{W}^i$ be defined for every shortest signal path waypoint as a subset of rows in $\mathcal{F}_v$

$$\mathcal{W}^i = \begin{pmatrix} P_w^{\max(0,i-c)} & P_h^{\max(0,i-c)} & P_\alpha^{\max(0,i-c)} \\ & \vdots & \\ P_w^{\min(l,i+c)} & P_h^{\min(l,i+c)} & P_\alpha^{\min(l,i+c)} \end{pmatrix} \tag{27}$$

where $c \in \mathbb{N}$ is the window context width. The resulting *Windowing* feature vector $\mathcal{F}_w$ is constructed from mean and variance among the windowed values as

$$\mathcal{F}_w = \begin{pmatrix} \overline{\mathcal{W}_w^1} & \overline{\mathcal{W}_h^1} & \overline{\mathcal{W}_\alpha^1} & \operatorname{var}\mathcal{W}_w^1 & \operatorname{var}\mathcal{W}_h^1 & \operatorname{var}\mathcal{W}_\alpha^1 \\ & & \vdots & & & \\ \overline{\mathcal{W}_w^l} & \overline{\mathcal{W}_h^l} & \overline{\mathcal{W}_\alpha^l} & \operatorname{var}\mathcal{W}_w^l & \operatorname{var}\mathcal{W}_h^l & \operatorname{var}\mathcal{W}_\alpha^l \end{pmatrix} \tag{28}$$

Note that the radius feature values $\mathcal{F}_v^r$ are omitted. It is because the preliminary results showed that α facilitates better subsequent fits as it reflects the actual curvature linearly as opposed to the radius, which goes to infinity for straight line segments. The windowing-based characterization for the signal path in Fig. 6 is illustrated in Fig. 8.

6.1.3 Histogram-based Characterization

The *Histogram* feature vector is defined as $\mathcal{F}_h = (\operatorname{hist}_b(\mathcal{F}_v^w)^\intercal, \operatorname{hist}_b(\mathcal{F}_v^h)^\intercal, \operatorname{hist}_b(\mathcal{F}_v^\alpha)^\intercal)$, where hist_b is normalized b-bin histogram of given feature vector column. We select $b = 10$. The method is intended to characterize arbitrary signal path features by a fixed-size vector suitable for subsequent standard regressions. It showed the best results in preliminary evaluations compared to other considered methods based on orthogonal polynomial systems, which are therefore not included in the presentation of the examined environment characterization approaches.

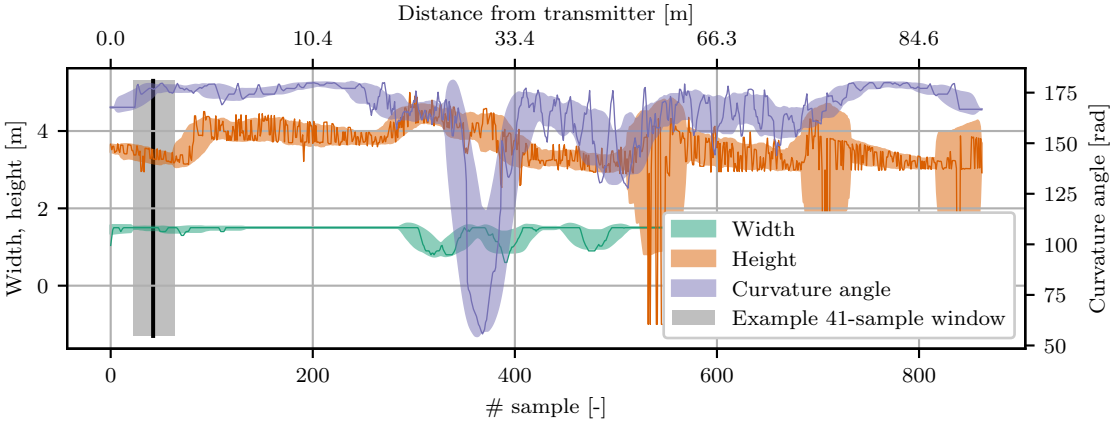

Figure 8: Windowing-based characterization. Color-coded areas show the variance, whereas raw measurements are solid lines. The illustrated Example for the same shortest signal path as visualized in Fig. 7 with one 90° curve depicted in Fig. 6. A single window $\mathcal{W}^{42}$ is depicted to illustrate the context of signal variance and mean value computation.

6.1.4 Line-of-sight Occupancy Characterization

In our previous work [118], the line-of-sight occupancy ratio is utilized as the regression parameter characterizing the environment geometry. A 2D occupancy grid is created by projecting the 3D grid into the horizontal plane, proclaiming unknown grid cells as occupied. The grid cell is considered occupied if it contains any projected point from the point cloud. Line-of-sight between the radio locations P_{tx} and P_{rx} is determined by Bressenham's line algorithm $\mathfrak{B}\left(P_{tx}, P_{rx}\right)$ [120]. The line-of-sight occupancy ratio [118] can be then expressed as

$$\mathcal{F}_o = 1 - \frac{\sum_{P_i \in \mathfrak{B}(P_{tx}, P_{rx})} G_{P_i^x, P_i^y}}{|\mathfrak{B}\left(P_{tx}, P_{rx}\right)|}, \tag{29}$$

where $G_{P_i^x, P_i^y}$ has the value 1 when occupied and 0 when free. The computation procedure is illustrated Fig. 9.

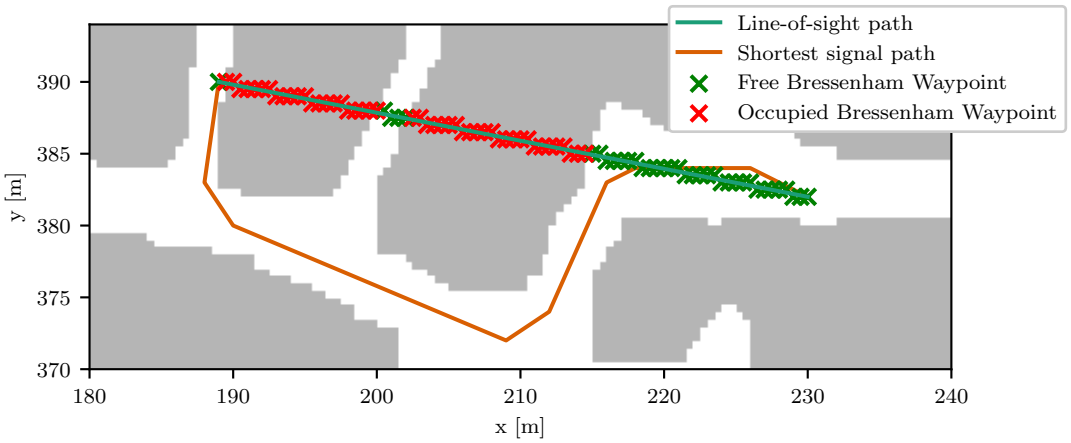

Figure 9: Illustration of occupancy feature computation.

6.2 Waveguide Linear Model (WLM)

The *Waveguide Linear Model* (WLM) exploits (13) and (14) to infer the material properties $\epsilon_r^{(v)}$, $\epsilon_r^{(h)}$, Δh, θ, and γ that cannot be directly assessed in full detail because they depend on the non-surface portions of the tunnel walls or details like roughness, which cannot be measured reliably enough. However, we assume that local tunnel geometry properties, the corridor width, height, radius, and segment length (w_i, h_i, r_i, l_i) can be observed as rows of $\mathcal{F}_g$, which is described in Section 6.1.1. We show that the gain depends linearly on the unobserved parameters (or their transformations) with the coefficients computed from the observed descriptors of the tunnel geometry.

Assuming a vertically oriented antenna, let the straight segment gain be fixed into the horizontal mode. Hence, the i-th straight segment gain in (13) can be reformulated as

$$\mathcal{G}_i^s = a_i \epsilon_*^{(h)} + b_i \epsilon_*^{(v)} + c_i \Delta h^2 + d_i \theta^2, \tag{30}$$

$$a_i = \frac{l_i \ln 10 \lambda^2 (m+1)^2}{40 w_i^3}, \qquad b_i = \frac{l_i \ln 10 \lambda^2 (n+1)^2}{40 h_i^3},$$
$$c_i = \frac{l_i \ln 10 \lambda \pi^2}{40} \left(\frac{1}{w_i^4} + \frac{1}{h_i^4} \right), \qquad d_i = \frac{l_i \ln 10 \pi^2}{\lambda 40}$$
$$\epsilon_*^{(h)} = \frac{\epsilon_r^{(h)}}{\sqrt{\epsilon_r^{(h)} - 1}}, \qquad \epsilon_*^{(v)} = \frac{1}{\sqrt{\epsilon_r^{(v)} - 1}},$$

a linear equation with respect to (w.r.t.) the substitute variables $\epsilon_*^{(h)}$, $\epsilon_*^{(v)}$, Δh^2, and θ^2, where the descriptors a_i, b_i, c_i, and d_i are computed directly from the uniform tunnel segment geometry.

In the j-th curved tunnel segment, the gain w.r.t. the roughness Δh and reflectivity γ can be reformulated by expanding the logarithm of the product in (14) into a sum of logarithms and then changing the base of the second term to get

$$\mathcal{G}_j^c = \frac{1}{|R_j|} \sum_{x' \in R_j} e_j(x') \left(\log_{10}(\gamma) + f_j(x') \Delta h^2 \right), \tag{31}$$

where x' and R_j have the same meaning as in (14) and

$$e_j(x') = \frac{20 l_j}{2\sqrt{r_j^2 - (x' - r_j)^2}} \tag{32}$$

and

$$f_j(x') = \frac{-8\pi^2 \sin^2 \left(\arctan \left(\frac{\sqrt{r_j^2 - (x' - r_j)^2}}{r_j - x'} \right) \right)}{\ln 10 \lambda^2}, \tag{33}$$

making the term linear w.r.t. $\log_{10} \gamma$ and Δh^2. We unify the two types of tunnel segments, the straight and curved, based on a radius value threshold $\check{r}$ (we use $\check{r} = 15\,\mathrm{m}$) as

$$\mathcal{B}_{\mathrm{WLM}}^k = \begin{cases} (a_k, b_k, c_k, d_k, 0) & \text{if } r > \check{r} \\ \left(0, 0, \frac{1}{|R_k|} \sum_{x' \in R_k} e_k(x'), 0, \frac{1}{|R_k|} \sum_{x' \in R_k} e_k(x') f_k(x') \right) & \text{otherwise} \end{cases}, \tag{34}$$

which makes it possible to define the WLM model by a latent parameter vector

$$X_{\mathrm{WLM}} = (\epsilon_*^{(v)}, \epsilon_*^{(h)}, \Delta h^2, \theta^2, \log_{10} \gamma), \tag{35}$$

such that a signal is predicted by the dot product as

$$\mathcal{G} = X_{\text{WLM}} \cdot \sum_{i=1}^{|\dot{\mathcal{F}}_v|} \mathcal{B}^i_{\text{WLM}} = X_{\text{WLM}} \cdot \mathcal{B}_{\text{WLM}} \tag{36}$$

where $\dot{\mathcal{F}}_v$ is defined in (23) and i iterates over all detected uniform segments detected by the segment-based characterization introduced in Section 6.1.1.

The learning step is performed in the least squares sense given a collection of N observations $\mathcal{B}_{\text{WLM}i}$, $\mathcal{G}_i$ from an overdetermined linear equation system

$$\begin{bmatrix} \mathcal{B}_{\text{WLM}\,1} \\ \vdots \\ \mathcal{B}_{\text{WLM}\,N} \end{bmatrix} \times X_{\text{WLM}} = \begin{bmatrix} \mathcal{G}_1 \\ \vdots \\ \mathcal{G}_N \end{bmatrix}. \tag{37}$$

In addition to the environment geometry, the waveguide model (13) also considers a measure of the surface roughness Δh, reflectivity γ, and tilt θ as the input parameters. Sadly, neither the original paper [110] provides useful instructions on how these measures can be computed, nor were we able to find a satisfactory surrogate method. That is why we opted to solve them via regression, which is supported by the presented results.

6.3 Variance Windowing Model (VWM)

The *Variance Windowing Model* (VWM) combines two principles as seen from (13) and (14). Firstly, the total logarithmic gain (units of dB) can be expressed as a sum of partial gains. Secondly, abrupt local changes in the tunnel geometry influence the local gain factor. Imagine leaving a wide and high cavern by a small tunnel. A proportion of the signal sent from the cavern to the tunnel deflects from the tunnel's portal as opposed to when the signal would be transmitted already in the tunnel, the signal being directed as in waveguide.

The method aims to provide an automatic method that would reflect both phenomena. The input geometry vector $\mathcal{F}_v$ is first transformed to $\mathcal{F}_w$ by the windowing-based environment characterization described in Section 6.1.2, using the context width 3, leading to 7 samples wide windows. Larger windows effectively averaged the values, thus losing information, which deteriorated the performance. The shortest path distance is captured implicitly by the number of windows. The i-th row $\mathcal{F}^i_w$ of the matrix $\mathcal{F}_w$ is called a spatial element that yields a local gain contribution $\mathcal{G}^i$ based on its values. For VWM, we propose the relation between $\mathcal{F}^i_w$ and its gain element $\mathcal{G}^i$ is polynomial

$$\mathcal{G}^i = X_{\text{VWM}} \cdot \mathbb{P}^p(\mathcal{F}^i_w), \tag{38}$$

where $\mathbb{P}^p$ is the polynomial transform that turns a vector of the type $(a, b, c, \dots)$ to

$$(1, a, b, c, ab, a^2, bc, b^2, ca, c^2, \dots, c^p).$$

The approach is intended to provide more degrees of freedom to fit in, contrary to the WLM. X_{VWM} is the latent variable vector of the same size as $\mathbb{P}^n(\mathcal{F}^i_w)$. Summing the partial gains yields the total gain on a given query as dot product

$$\mathcal{G} = \sum_{i=1}^{l} X_{\text{VWM}} \cdot \mathbb{P}^n(\mathcal{F}^i_w) = X_{\text{VWM}} \cdot \sum_{i=1}^{l} \mathbb{P}^n(\mathcal{F}^i_w). \tag{39}$$

Learning the model is possible in the least square sense by aggregating observations as in the WLM. We use $p = 2$ and regard only the curvature, which performed the best according to the preliminary Akaike model selection criterion [121]. Thus, the model is defined by just 6 parameters.

6.4 Generic Embedding Polynomial Model (GEPM)

The waveguide concept of signal propagation is extended in the proposed *Generic Embedding Polynomial Model* (GEPM) by further abstracting the material properties. As the VWM, exploiting the known linearity of signal propagation in the considered waveguide, failed to extrapolate well in the preliminary tests, we formed a hypothesis about an ill-conditioned dataset where the distribution of positive samples outweighed the model that predicts poorly in less populated regions, thus extrapolating poorly. The embedding technique UMAP [122] was used to remedy the issue by finding an anonymous latent space by learning a complex kernel function. We propose to use the method with histogram-based environment characterization $\mathcal{F}_h$ described in Section 6.1.3 transformed by UMAP to one-dimensional latent feature space $\mathcal{F}_u$. The feature space $\mathcal{F}_u$ is further concatenated with $\mathcal{F}_s$, and the resulting pair of values is used for linear regression similarly as for the VWM (described in Section 6.3) as it showed promising preliminary results.

6.5 Evidence Regression Model (ERM)

The *Evidence Regression Model* (ERM) is based on describing a space amid queried radio locations by a low dimensional fixed-size feature vector. The shortest signal path length $\mathcal{F}_s$ and occupancy ratio $\mathcal{F}_o$ are fed together with the measured signal gain to learn a regressor based on the Gaussian Process (GP) [51]. The method has been presented in [118], and it is briefly summarized here to make the thesis self-contained.

GP is a possibly infinite collection of random variables where every finite subset of the variables follows the multivariate normal distribution. We use GP to aggregate observations $x = (\mathcal{F}_o, \mathcal{F}_s), y = \mathcal{G}$ of the regressed signal propagation function $\hat{\mathcal{S}}$ measured with the white noise ε

$$y = \mathcal{S}(x) + \varepsilon, \quad \varepsilon \in \mathcal{N}(0, \sigma^2). \tag{40}$$

GP $\mathcal{GP}$ is a distribution over all possible functions [51] over the given domain

$$\mathcal{S}(x) \sim \mathcal{GP}(m(x), K(x, x')), \tag{41}$$

where $m(x)$ and $K(x, x')$ are the mean and covariance, respectively, defined as

$$m(x) = E\left[\mathcal{S}(x)\right], \tag{42}$$
$$K(x, x') = E\left[\left(\mathcal{S}(x) - m(x)\right)\left(\mathcal{S}(x') - m(x')\right)\right]. \tag{43}$$

The latent values $\mathcal{S}_*$ of the testing data $(\mathcal{F}_o, \mathcal{F}_s)_*$ are computed given the training data as

$$\begin{aligned} \mu((\mathcal{F}_o, \mathcal{F}_s)_*) &= K((\mathcal{F}_o, \mathcal{F}_s), (\mathcal{F}_o, \mathcal{F}_s)_*)\left[K((\mathcal{F}_o, \mathcal{F}_s), (\mathcal{F}_o, \mathcal{F}_s)) + \sigma^2 I\right]^{-1} y, \\ (\sigma((\mathcal{F}_o, \mathcal{F}_s)_*))^2 &= K((\mathcal{F}_o, \mathcal{F}_s)_*, (\mathcal{F}_o, \mathcal{F}_s)_*) - \\ -K((\mathcal{F}_o, \mathcal{F}_s), &(\mathcal{F}_o, \mathcal{F}_s)_*)^T \left[K((\mathcal{F}_o, \mathcal{F}_s), (\mathcal{F}_o, \mathcal{F}_s)) + \sigma^2 I\right]^{-1} K((\mathcal{F}_o, \mathcal{F}_s), (\mathcal{F}_o, \mathcal{F}_s)_*), \end{aligned} \tag{44}$$

where $K((\mathcal{F}_o, \mathcal{F}_s), (\mathcal{F}_o, \mathcal{F}_s)')$ is the covariance function. The squared exponential kernel is selected as the covariance function

$$K(x, x') = \sigma^2 \exp\left(-\frac{\|x - x'\|^2 2}{2l^2}\right), \tag{45}$$

where σ^2 and l are the method hyperparameters output variance and length scale, respectively, tuned by automatic black-box optimization provided by the used GPy implementation [123].

Chapter 7
Dataset and Evaluation Framework

The proposed solution to communication infrastructure building in robotic subterranean exploration missions relies on a signal propagation model. Four models are proposed based on the related work review, and the models need to be evaluated using representative scenarios. A part of the thesis effort was creating a suitable dataset described in Section 7.1. Based on the dataset, the preliminary approaches and finally proposed methods have been evaluated within the developed framework described in Section 7.2. The evaluation results are presented in Chapter 8, and a showcase of the demonstrative field deployment is reported in Section 8.7.

7.1 Dataset

The signal propagation models have been evaluated on the real-world dataset to assess their performance. Real signal propagation data have been collected in underground tunnel-like environments as measurements of the real gain between the transmitter and receiver corresponding with the considered robotic exploration scenario. Recalling the proposed mote placement strategy, we target predicting the signal propagation in scenarios with long and curved corridors where waveguiding effect and other nontrivial phenomena might occur. We tasked ourselves that the dataset should include as many complex signal propagation examples as possible. Besides, the dataset needs to comprise numerous samples to provide statistical significance. A suitable 3D map of the environment needs to be also included as the proposed methods can benefit from the environment geometry characterization. Finally, despite the signal modeling methods assumptions, we aimed to capture the dataset even richer so that it may be useful for other future works, albeit its full processing would be out of the thesis scope.

7.1.1 Data Collection Equipment

Since we expect to gather large data collections to capture a significant portion of the selected underground environments, we opt for an automated data collection system. The key desired property of the collected measurements is a localization of the gain measurement within the 3D map of the environment, which is necessary to evaluate the environment geometry impact on the signal propagation. Therefore, we developed a sensor rig equipped with the Ouster OS0 LiDAR [84] and communication devices that enable localization of a particular measurement using the laser scan, see Fig. 10a. In particular, two sensor rigs have been constructed to collect data measurements of the transmitter and receiver simultaneously. Besides, we opt for using the autonomous mobile robot to collect data in confined spaces, where a human operator will block signal propagation as shown in Fig. 10b.

The developed sensor rig is made of $85\,\mathrm{cm}$ long wooden rod with the LiDAR at one end and radio devices on the other. The LiDAR provides 128 row scans at $10\,\mathrm{Hz}$ stored on the Intel® NUC class computer attached to the rig. Wood was selected as an electrical insulator, which should not disrupt the electromagnetic field. Rod's length was intended to keep radios approximately $0.5\,\mathrm{m}$ from the operator such that the signal attenuation by the mass of the operator would be minimized while keeping the rig compact enough.

The primary radio device selected is the RFM69HCW radio module used in the deployable motes introduced in Section 2.3. The motes on the rig were paired, so an exclusive duplex channel at $868\,\mathrm{MHz}$ was established between the two rigs with burst packets exchange at about $2\,\mathrm{Hz}$ in both directions. The

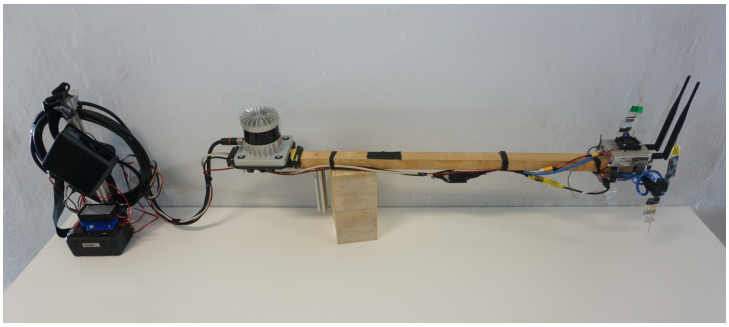

(a) Handheld sensor rig. Left to right, the peripheral with the Intel® NUC class computer and the battery are connected to the LiDAR fixed on one side of the wooden rod with a handle and radios placed on the opposite side.

(b) Husky A200 [4] mobile robot with the radio measuring equipment. The Leica TS-15 total station to the robot's right establishes a coordinate frame and captures ground truth positions.

Figure 10: Handheld sensor rig and autonomous robot used in data collection.

received signal power was measured directly via the internal circuitry of the mote. The motes have been set to their maximum transmitting power of $100\,\mathrm{mW}$. The antennas involved were oriented in the vertical direction (parallel to the z-axis) with regard to the LiDAR reference frame.

Besides, each rig carried one Mobilicom MCU-30 Lite [86] unit operating at $2.4\,\mathrm{GHz}$ and broadcast either at $-30\,\mathrm{dB\,mW}$ ($1\,\mu\mathrm{W}$) or $0\,\mathrm{dB\,mW}$ ($1\,\mathrm{mW}$). Mobilicom's received power and signal-to-noise ratio measurements are available at the firmware at $0.5\,\mathrm{Hz}$. Further, several statically placed and manually localized Mobilicom radios were present at various locations to increase the number of measurements. Each Mobilicom device offers two antennas, each operating at a designated channel. We oriented one antenna vertically and one horizontally. Different antenna orientations, power levels, and frequencies are intended to introduce diversity into the dataset, making it usable for further generalization and testing.

The time synchronization between the rigs was based on the ordinary *Network Time Protocol* (NTP) [124] with the *Wireless Local Access Network* (WLAN) router as the time source. The rigs are globally time-synchronized at the beginning of the data collection, assuming negligible drift during the measurement. Apart from support electronics, an off-the-shelf replaceable rechargeable battery is on the rig, allowing for around two hours of uninterrupted operation. The Husky A200 [4] autonomous robot used for data collection was equipped with the same technology as the handheld rig.

7.1.2 Data Collection Venue

The utilized evaluation dataset was gathered in municipal utility tunnels[4] [125]. Such facilities are designed to provide infrastructure support for the distribution of electricity, gas, Internet, water supply, and other utilities in the city's central region. The selected area of the city underground comprises corridors equipped with grounded iron racks that are approximately $1\,\mathrm{m}$ wide and $1\,\mathrm{m}$ apart. The tunnels are cut into the sedimentary bedrock at a depth of about two to four meters with reinforced concrete walls spanning an area of around $1\,\mathrm{km}^2$. A precise 3D map of the environment has been captured by a globally referenced point cloud using the Leica BLK360 Imaging Laser Scanner; see the example of the map depicted in Fig. 11. The map of the municipal tunnels contains roughly 317.5×10^6 points that are filtered to at most 1×10^4 points per square meter and cropped to contain only the selected areas of interest, resulting in approx 1.6×10^6 points.

[4] During the work on the thesis, more data collection campaigns have been performed. Due to the time constraints, we decided to list here only one dataset as its postprocessing is time-demanding. Processing all the collected data is beyond the thesis's time frame. Summed up, it took one person about two weeks to post-process one dataset campaign.

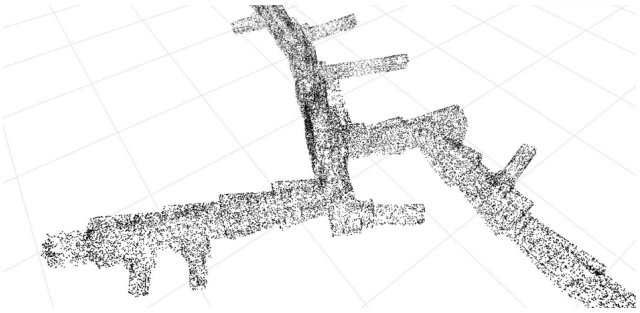

Figure 11: A snapshot of the dataset venue map used for localization and environment geometry characterization.

The gathering campaign lasted two workdays and resulted in around $8\,\mathrm{h}$ of LiDAR and radio recordings captured by each of the handheld rigs, amounting to ca. $690\,\mathrm{GB}$ of raw data. Special care was taken during the gathering to refrain from abrupt movements, mainly rotations, which could introduce skew into the resulting point cloud collected by the LiDAR at the sensor rig. Further, as the Mobilicom's signal strength frequency was limited to $0.5\,\mathrm{Hz}$, both operators moved about $2\,\mathrm{km\,h^{-1}}$ or slower. The operators were requested to roam the environment so they do not stay between the radios while measuring.

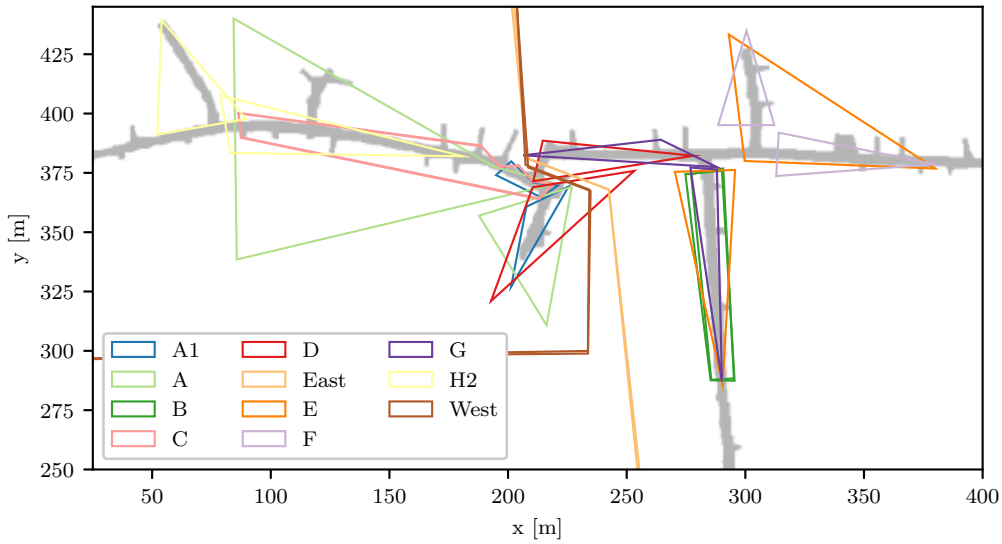

Figure 12: The annotated tunnel subsets of the evaluation dataset. Each subset is defined by two polygonal areas where the receiver and transmitter are placed. Hence, the signal is propagated in each subset through the tunnels between two particular areas.

The collected dataset is manually annotated into labeled subsets indicated in Fig. 12 and detailed in Tab. 1. The annotation is designed so that some subsets contain "easy" portions of the tunnel, like straight or singly-bent corridors, whereas others contain difficult paths with several curved sections. We aim to evaluate the proposed methods for extrapolation and generalization capability. Further, more labels of the same type are provided in different regions of the tunnels to enable cross-validation over nearby and far parts.

Table 1: Descriptions of the annotated subsets of the dataset.

Subset	# Samples	Description
all	33 134	All measured samples combined.
A1	1 017	Around-corner through ca. 90° $r = 2\,\mathrm{m}$ curve.
A	3 683	A1 with extended straight-passage; all samples went through the curve.
B	2 028	Straight passage.
C	11 851	Straight passage with slight curves of $r > 15\,\mathrm{m}$.
D	147	Complex signal path through 4 curves.
East	8 081	Combined samples in eastern† portion of the tunnels.
E	58	Complex signal path through 2–3 curves.
F	587	Around-corner, 90° $r = 2\,\mathrm{m}$ curve with long straight segments.
G	183	Around-corner, 100° $r = 3\,\mathrm{m}$ curve, fireproof door in northern part.
H2	340	A.-corner, 90° $r = 2\,\mathrm{m}$ curve, "straight" segment bent, fireproof door.
West	23 151	Combined samples in western† portion of the tunnels.

† East and West corresponds to the image's reference frame as shown in Fig. 12, not to the geographic directions.

7.1.3 Post-processing

After collecting data in the physical gathering campaign, the local LiDAR scans have been registered in the global environment map using the *Iterative Closest Point* (ICP) [40] implementation "libpointmatcher" [126]. The algorithm repeatedly solves the ordinary least squares equation for an unknown homogeneous transformation, each time with target points assigned as the nearest neighbor. We use the point-to-plane criterion of the equation.

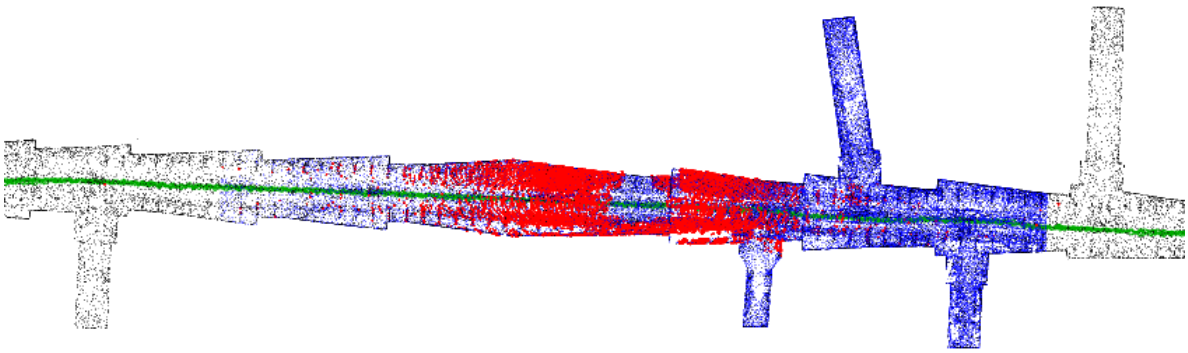

Figure 13: Automatic computation of the rig trajectory (green line) using sequential registration of subsequent local LiDAR scans (red) into a cropped portion (blue) of the global 3D map (black). Note the increased density of the local red scan, remedied by a density filter (not shown).

The ICP is used to sequentially register individual gathered local scans into the global map by using the previous registration result to initialize alignment of the next scan as illustrated in Fig. 13. The first scan is pre-aligned manually; see Fig. 14. Hence, a time-stamped trajectory of the measuring rig is obtained. The data postprocessing was semi-supervised because the ICP was prone to failure either by diverging completely or finding the wrong local minima, especially in long repetitive sections of the tunnels. Therefore, the shape of the sensor rig path has been manually verified. When in doubt, the corresponding scan was reprojected to the global map to validate whether the localization worked well. In the case of an error, the path was cropped, and a new initialization was created after the ICP's

point of failure.

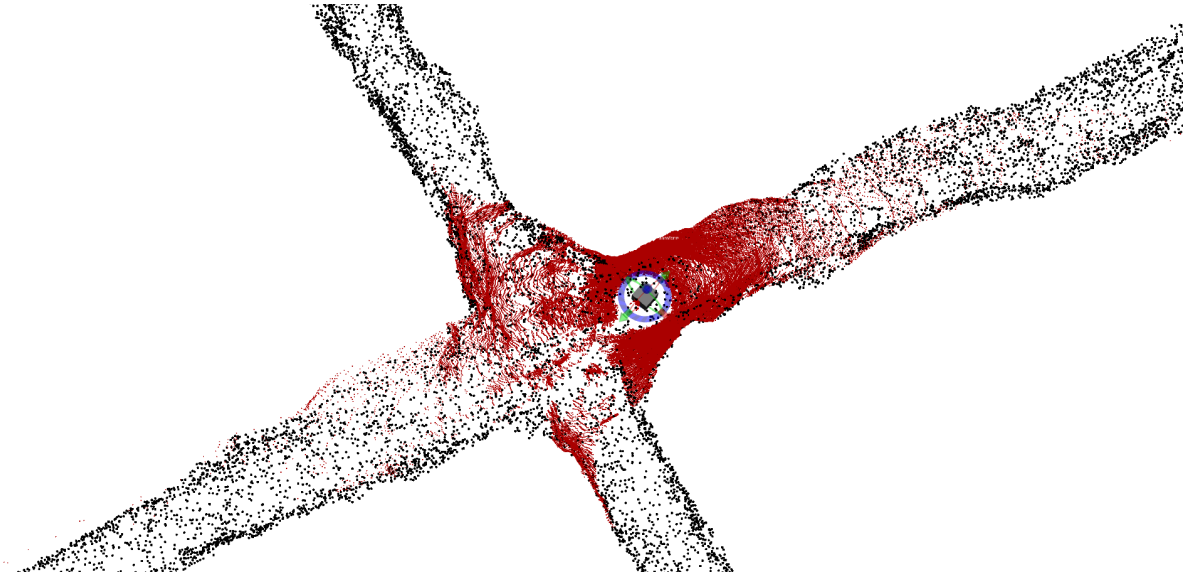

Figure 14: Manual alignment of the local scanned point cloud (red) into coarse global 3D point cloud (black) using an interactive graphical element (grey box with arrows and discs in the middle) defining a transform in 6 degrees of freedom.

Systematic failures were caused due to the LiDAR rays projecting with increased density for closer surfaces as illustrated in Fig. 13. In our experience, such dense areas outweigh farther points that capture a large-scale geometry crucial for a correct registration. That is why we employ a density filter to reduce such near-and-dense regions. The achieved localization precision is in units of centimeters, smaller than the used wavelength. Thus, we consider the localization sufficient.

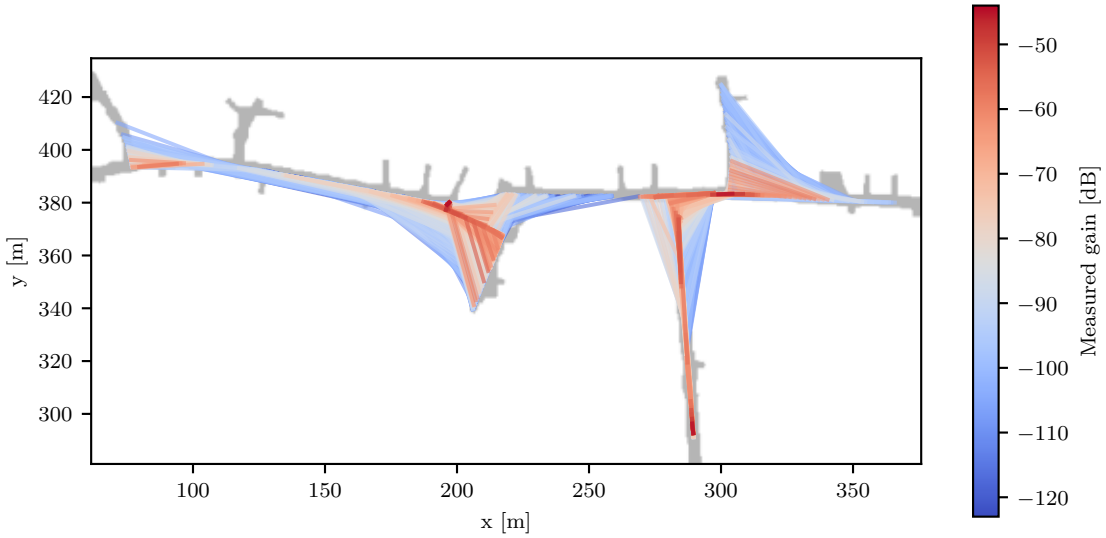

Figure 15: Resulting localized measurements of mote signal.

Static coordinate transformation, known by the design of the sensor rigs, was applied to obtain the positions of the antenna bases in six degrees of freedom. The rig localization was selected in the trajectory computed by the ICP by matching time stamps. Further, each measurement was labeled with the used frequency, nominal transmitter power, antenna type, and communication technology. After the postprocessing, the dataset comprises about 8.6×10^4 localized signal measurements, visualized in Fig. 15, of which 3.3×10^4 is measured by the motes, the rest by the Mobilicom. The detailed 3D environment model is a part of the dataset.

Note that the dataset contains only positive samples that are measured when the signal was successfully received, albeit the localization is available even for cases the signal was lost. However, we found it questionable how to represent negative samples in the dataset; therefore, we leave it for future work. The measured gains also include the power loss induced by the circuitry imprecision that was prospected to compensate for. Similarly to [110], we assumed that the signal propagates in free space as long as the transmitter and receiver are inside the first Fresnel zone and antennas are aligned. Hence, comparing measurements of the signal taken in the zone, we can enumerate the power loss induced by both the receiving and transmitting devices as $G_{rx} + G_{tx}$ in (11). However, we did not succeed in performing the method reliably. Therefore, we model the total attenuation that involves possible device-specific elements.

7.2 Evaluation Framework

The developed evaluation framework, called `zoulamar_dp`, has been designed to implement the proposed methods and error-proof evaluation of the volume of data gathered from the campaigns. The implementation systematically separates computational stages, keeping their results as reusable unique data units. Besides, care was taken to develop the implementation system so that it can be seamlessly deployed on a robotic unit, safely using all pre-computed data like the learned model parameters.

Listing 3: Example of the evaluation framework computational stage.

```
PipelineRootCommsRosified/.../Umap/              Computation stage as of Section 6.4.
├── config.yaml                  Target file recognized by this module with no dependencies.
├── KolKNall.umap                UMAP fitted to subset "all", source for KolKNall.npz
├── KolKNall.npz          Transformed measurements in subset "all", listed in module's registry.
├── KolKNall.pdf          UMAP module also provides visualization target shown in Fig. 19.
├── ...                                  Each subset has its .npz, .umap and .pdf files
└── Poly.2x/                 Subdirectory maps stage Poly with label 2x separated by dot.
    ├── config.yaml
    ├── KolKNall.yaml              Learned polynomial, depends on parent's KolKNall.npz.
    └── L_KolKNall_E_KolKNE.pred.npz          Prediction results on "E", learned on "all".
```

The structure of the intermediate data processing steps steers us to develop an evaluation framework to organize data in a hierarchical structure similar to the file system directory tree. The computation scheme is mapped so that each file system directory represents one computational stage that collects related implemented methods. The intermediate results are unambiguously saved as files in the corresponding directory, making it possible to reuse them in subsequent stages. A computation stage may be present multiple times when used by different parent stages or distinguished by a label separated by a dot in the path's name component. An example of a computation stage with its created targets is visualized in Listing 3. An example of the computational tree is illustrated in Listing 4.

Listing 4: The directory tree supporting the developed `zoulamar_dp`.

```
PipelineRootCommsRosified/                  Root module containing source data.
└─ Filter.motes/                            Allows only samples annotated as motes.
   ├─ Augment.histogram/                    Section 6.1.3
   │  └─ Forge/                             Splits the dataset to training and testing subsets.
   │     └─ Umap/                           Section 6.4
   │        ├─ Poly.2x/                     Section 6.4
   │        │  └─ Report/                   Chapter 8
   │        └─ #Poly.crop2x/                Labels allow experimenting with different parameters.
   ├─ Augment.occupancy/                    Section 6.1.4
   │  └─ Forge/
   │     ├─ GP.mesas/                       Section 6.5
   │     │  └─ Report/
   │     └─ #Umap/                          Subtrees may be disabled by prefix octothorpe.
   │        └─ GP/
   │           └─ Report/
   ├─ Augment.segmentation/                 Section 6.1.1
   │  └─ Forge/
   │     └─ Bedford/                        Section 6.2
   │        └─ Report/
   ├─ Augment.windowing/                    Section 6.1.2
   │  └─ Forge.rad_only/
   │     └─ PolyForWindowing/               Section 6.3
   │        └─ Report/
   ├─ Forge.fspl/                           Chapter 8
   │  ├─ FSPL/
   │  │  └─ Report/
   │  ├─ FSPL.beta/
   │  │  └─ Report/
   │  └─ Interpolator.halire/               Section 8.7
   ├─ StaticError/                          Section 8.1
   └─ #Augment.chebyshev/                   Disabled part of zoulamar_dp which was not reported.
      └─ Forge/
         └─ Umap/
            └─ Poly.2x/
```

The evaluation framework is implemented in `Python3` language [127]. Its usage can be considered similar to program `make` [128]; however, it works on targets that are Python objects that store intermediate computational data. A target is always associated with a unique file system path to store the data persistently and unambiguously; corresponding Python callable objects are linked to the target object at the discretion of the computational stage. Each target can have other targets referenced as its source data with optional parametrization; thus, the chain of targets forms the data processing pipeline. The final implementation adheres to the *"Don't Repeat Yourself"* principle by exploiting Python's module import system such that a name-matched Python module drives a computational stage. The code is documented by Python's `docstring`; see the attached source files for details. The core implementation is made of 4328 lines of source code in 19 files, which drive the computation of around 1500 individual targets organized in 58 computations stages. The computational modules rely on 3rd party software, most notably the `NumPY` [129], `SciPy` [130], `umap-learn` [122] and `GPy` [123].

Listing 5: Example of using the developed framework's command line frontend.

```
# Show particular module's declared targets and state
./ctl.py show Pip.../Augment.histogram/Forge/Umap

# Make one of a particular module's declared targets
./ctl.py make Pip.../Augment.histogram/Forge/Umap -t KolKNall.pdf

# Generate a script launching computation for whole pipeline sub-tree
./ctl.py scan Pip.../Augment.histogram/Forge/Umap -r -o do_it.sh

# Script invokes equivalents to line 4 harnessed by GNU Parallel
./do_it.sh
```

A command line utility was developed to manage the system of modules and targets interactively and consistently, as demonstrated in Listing 5. A basic diagnostic routine and inspection command are provided. Besides, miscellaneous utility is developed to generate a shell script that invokes intermediate computations using GNU Parallel [131], allowing exploitation of parallel computational environments. The generated script is constructed respecting target precedence and up-to-date data. Thus, its single invocation performs minimal computation to achieve the desired state.

A ROS [21] node is implemented to expose the system's consistency to usage in real-world deployment by selecting the particular methods and creating the processing pipeline. The node is given a particular computation module with a selected output and input target. The node inserts incoming compatible ROS messages as the input target value of a single specific target, launches the final target computation, and publishes the result. The pre-computed results, like the learned regression parameters, are automatically loaded from the file system hierarchy of the stored data.

Off-line experiments relied on measurement localization as described in Section 7.1.3 was implemented separately as a simple ROS package wrapping the `libpointmatcher` library [126]. Geometrical features are extracted from the environment model by the exploration framework [119], which also provides localization during real experiments. The environment geometry characterizations described in Sections 6.1.1 to 6.1.4 and the proposed signal propagation models in Sections 6.2 to 6.5, together with the ROS node, are part of the evaluation framework `zoulamar_dp` that is attached to the thesis on the optical Disc. However, the dataset was decided not for publication as it contains sensitive data related to critical infrastructure.

Chapter 8
Results

This chapter presents the results regarding the proposed methods' quality and feasibility. The proposed signal prediction methods (Sections 6.2 to 6.5) are examined together with two baseline approaches: (i) the uninformed *Free Space Path Loss Model* (FSPL); and (ii) its variant with the attenuation coefficient β, see (11), denoted FSPL-β. However, we first assess the systematic measurement error that is inherently present in the captured dataset in Section 8.1. In Section 8.2, we separately examine and discuss the performance of individual methods by testing their extrapolation capability in a cross-validation scheme. Section 8.3 briefly summarizes the computational and memory demands of the examined models. Then, the methods are compared relative to each other using the Wilcoxon matched sample signed-rank test [132], which investigates the median of prediction mean errors among the examined cross-validation cases in Section 8.4. We examine material properties inferred by the proposed WLM in Section 8.5. A detailed discussion of the achieved signal propagation modeling results is presented in Section 8.6. Despite several specific cases where individual approaches fail, the overall feasibility of the proposed approach is supported by the presented results. Deployment of the presented work in a field exploration mission is summarized in Section 8.7.

8.1 Systematic Measurement Error in the Dataset

The dataset of signal propagation in urban municipal tunnels introduced in Section 7.1 exhibits a level of measurement error as illustrated in Fig. 16a. We aggregated the samples into spatially determined groups to quantify the error. A group contains samples with the same position of the receiver and transmitter under discretized grid map with the grid cell size of $0.5\,\mathrm{m}$. As the measured gain distribution is exhibited as the normal distribution, the standard deviation is used to characterize the gain fluctuation within a group. The dataset is structured into about 2348 groups with the average size 7.84 samples per group. A statistic of standard deviations among groups is depicted in Fig. 16.

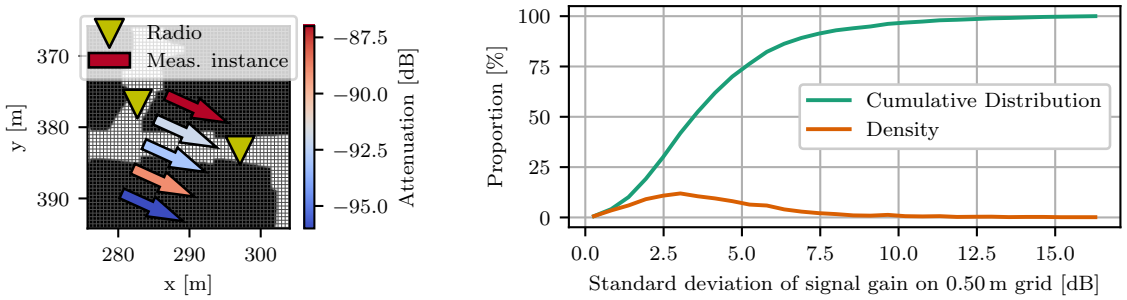

(a) A sample group of five measurements between radios within the same respective squared cells with the size $0.5\,\mathrm{m} \times 0.5\,\mathrm{m}$. Measurements span range of around $7\,\mathrm{dB}$ with standard deviation of $3.14\,\mathrm{dB}$.

(b) Distribution of standard deviations among signal measurements in the municipal utility tunnel dataset. Each group of radio pairs within the same grid cell contributed by one standard deviation value.

Figure 16: Systematic measurement error analysis.

We can see that around 50 % of the measurements share a variance of under 3 dB, whereas 90 % of the examined groups fluctuate under 7.5 dB, for the selected spatial resolution 0.5 m. We argue that the systematic measurement error comes from three different sources.

1. The manufacturing imperfections have been estimated to cause transmission loss difference between different device pairs about ±4 dB based on laboratory measurements.

2. The accuracy of the ICP-based localization (see Section 7.1.3) is considered to be in units of centimeters, which is estimated to yield an error of approximately ±3 dB. Such systematic error is in line with the results reported in [75].

3. Finally, the environment itself might be dynamic contrary to the assumptions as, for example, a tramway track leads above certain portions of the environment.

Improving the assessment of the systematic measurement would entail effort outside the scope of this thesis. Hence, we use the presented statistic as an expected lower bound on the predictive performance of individual models. We do not expect that the models' prediction error would be lower than 7.5 dB standard deviation in 90 % of cases; thus, predictions around that value are considered satisfiable.

8.2 Cross-validation of Individual Models

An extended cross-validation scheme was used to investigate the models' ability to learn from examples and extrapolate the knowledge to spatially uncorrelated queries. Each model was first trained on each of the labeled areas (see subsets defined in Fig. 12) with the 85:15 train-test ratio. Thus, each model has been trained with 85 % measurements from the particular subset selected randomly with uniform distribution. Then, predictions for each subset were computed for every such trained model instance using the remaining 15 % measurements from the subset as the ground truth.

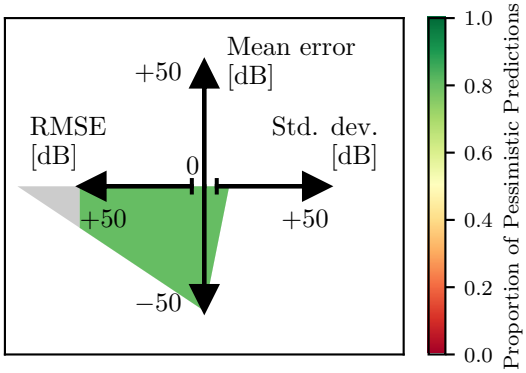

Figure 17: Legend of the proposed cross-validation visualization. The triangle's vertices represent values on two axes. The vertical axis denotes the prediction mean error, spanning the interval from −50 dB to +50 dB. The left part of the horizontal axis represents the root-mean-square-error (RMSE), while its right part shows the standard deviation, both half-axes with range 0 dB (in the center) to +50 dB. If the portrayed sample exceeds these limits, the triangle is cropped. Triangle color maps to the proportion of the pessimistic predictions, i.e., the cases where the signal was predicted with worse quality than in reality. The visualized example shows a cross-validation case with the mean error −50 dB, RMSE 75 dB (hence the cropped triangle), standard deviation 10 dB, and 80 % pessimism.

We consider the method's prediction bias important with regard to building the communication infrastructure. The value of the predicted signal gain below the ground truth is considered pessimistic as the model believes the signal between the queried radio positions is of poor quality, whereas in reality, the signal is better. In the context of communication availability, such a prediction would be caused by placing the communication mote (breadcrumb) earlier than necessary but still with sufficient signal for reliable communication. On the other hand, optimistic predictions where the predicted value exceeds the real measured signal gain might result in communication quality degradation or even complete loss of the signal. Therefore, we prefer pessimistic predictions over-optimistic predictions for robotic exploration scenarios.

The model predictions in the cross-validation evaluation are visualized for each particular learn-test case using colored triangles explained in Fig. 17. The vertices of the triangle map three statistical quantities: (i) the mean prediction error (the method's prediction bias) on the vertical axis, (ii) the root-mean-square-error (RMSE) on the left of the horizontal axis; and (iii) the standard deviation of prediction errors on the right of the horizontal axis. Hence, the narrower the triangle is, the more precise the predictions; the taller the triangle, the bigger bias was in the model's predictions. Further, the triangle color correlates to the proportion of predictions that overestimated the signal attenuation. Note that the color correlates with the triangle's orientation but is not necessarily the same. In the rest of this section, we comment results of the cross-validation evaluation for each particular model visualized in Fig. 18 using the visualization scheme described in Fig. 17.

Waveguide Linear Model (**WLM**), defined in Section 6.2, cross-validation results in Fig. 18a show poor performance, specifically in the dataset areas D and H2. Area D was intentionally designed to contain around-corner measurements, and the WLM overfits curved sections by lacking straight-line segment examples. The area H2 contains a long, slightly curved tunnel with a radius over the curved-section threshold. That is why the model misclassified the bend by the straight section and thus predicted it poorly. Generally, the assumptions of the WLM are not fulfilled with the particular municipal utility tunnel, which led to poor performance. The original method [110] assumes a coal mine with rectangular cross-section tunnels as opposed to the arched shape present. Nevertheless, the proposed model can be useful for inferring material properties, which is detailed in Section 8.5.

Variance Windowing Model (**VWM**), see Section 6.3, results depicted in Fig. 18b indicate that training on dataset areas A to C yields extrapolation performance in other areas significantly better than the WLM. However, that model cannot learn well in the difficult areas D, E, G, and H2. It is because the polynomial parameters cannot generalize beyond the presented samples.

Generic Embedding Polynomial Model (**GEPM**) from Section 6.4 fails to extrapolate the knowledge provided by the subset area E as shown in Fig. 18c. It is unsurprising because the dataset area E has only 58 samples, leading to uninformative anonymous UMAP embedding. For the other case, with enough samples, UMAP is able to find an anonymous latent space that is further illustrated in Fig. 19. The latent space allows the polynomial regressor to fit the samples well, leading to the prediction error means and variances both around 10 dB. Regarding the estimated systematic error, these results support the usage of the GEPM in the robotic mission. Interestingly, the method can extrapolate the learned model from area D significantly better than WLM and VWM methods, which both fail.

Evidence Regression Model (**ERM**) defined in Section 6.5 provides the best predictions among the proposed models, as can be seen in Fig. 18d. The ERM can learn from all areas with satisfactory extrapolation predictions in other areas. The results are achieved despite the limited input feature vector consisting of the occupancy ratio (depicted in Fig. 9) and distance as opposed to other proposed methods. Figure 20a depicts the model's predictions against input space to illustrate the model. The isolines of the prediction values illustrate that the ERM can implicitly reflect advanced signal propagation phenomena like the signal spatial oscillations discussed in [75]. We notice that the latent variables tightly correlate together; we argue that such a representation might be less informative than an orthogonal set of feature vectors, which would span the whole domain. The method can also be used

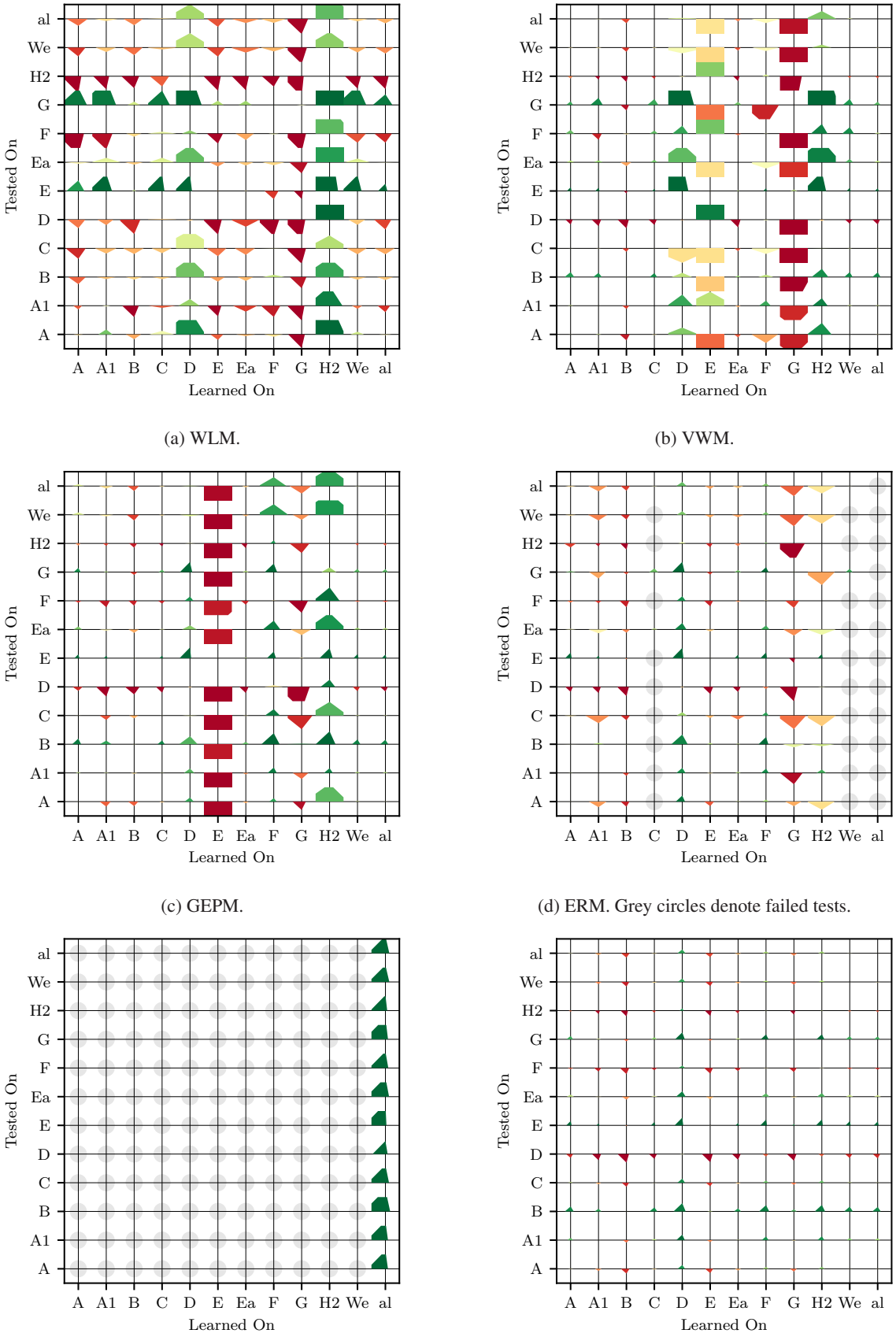

(a) WLM.

(b) VWM.

(c) GEPM.

(d) ERM. Grey circles denote failed tests.

(e) FSPL. Irrelevant cases as grey circles.

(f) FSPL-β.

Figure 18: Cross-validation performance visualizations. See Fig. 17 for the visualizations legend.

for active learning in the sense of Kriging using the posterior confidence interval, which is illustrated as useful with the ERM in Fig. 20b where a slice of the input space with the occupancy ratio fixed to 0.25 is portrayed. A possible drawback is that the method tends to be rather optimistic in extrapolation when learned only from the dataset areas G and H2. However, the overall cross-validation performance in Fig. 18d is satisfiable with low-dimensional geometry-based feature vectors.

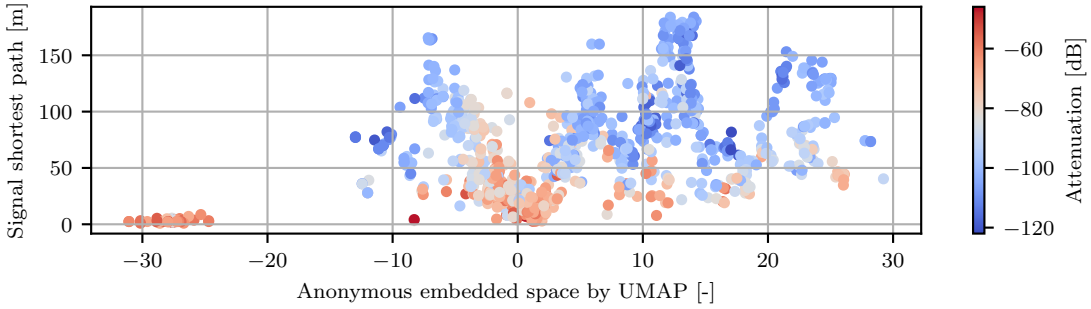

Figure 19: GEPM anonymous latent embedding space.

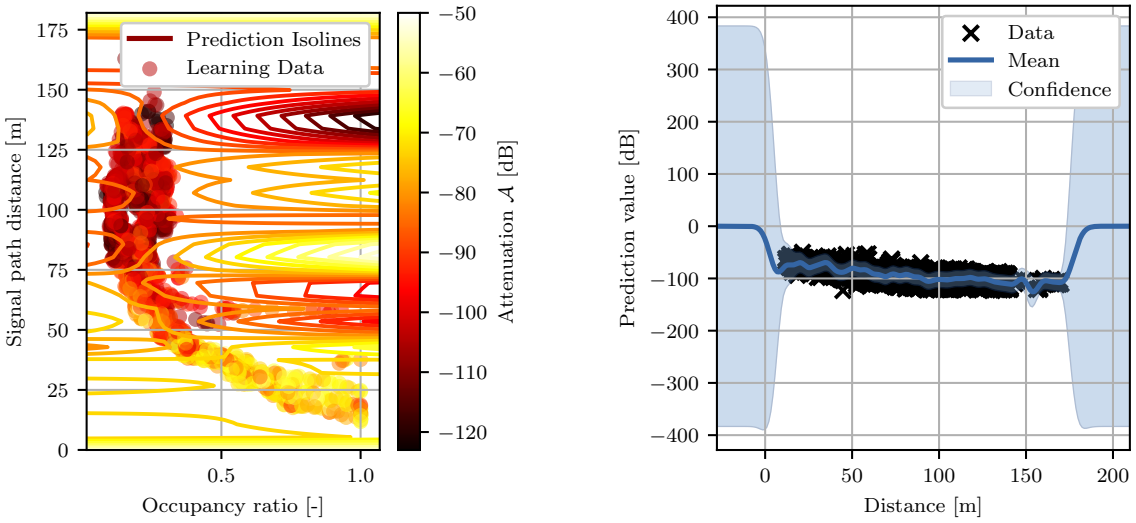

(a) Resulting signal attenuation modeled using occupancy ratio and radio distance. Notice the spatial oscillations along the distance (y) axis.

(b) Slice of the input space with the occupancy fixed to 0.25. The model correctly classifies the region beyond 175 m as unknown by assigning a wide confidence interval.

Figure 20: Plot of ERM predictions against input space.

Free Space Path Loss (**FSPL**) baseline model and its variant **FSPL-β** are summarized in Figs. 18e and 18f, respectively. The plain FSPL predictions overestimate the attenuation showing that the signal in the free space propagates *worse* than in underground. We explain the behavior by the strong waveguide effect happening underground, which focuses the signal energy to the tunnel rather than all directions of the dipole antenna radiation pattern as supported by [76]. Numerically, the prediction mean errors are between 50 dB and 70 dB. The accuracy of the FSPL is beyond usefulness, yet the error standard deviation occurs between 9 dB and 19 dB, meaning that the method is relatively precise. The attenuation predictions are surpassed by the FSPL-β model with the single parameter β learned by the least squares method. Although the error distribution's standard deviation is unchanged, the accuracy is improved. Besides, we do not see any signs of overfitting on any dataset areas.

The individual cross-validation results showed that the prediction of the signal availability in municipal utility tunnels is possible considering the systematic error discussed in Section 8.1. Among the considered models, the baseline FSPL-β provides a great prediction capability with only a single average attenuation coefficient β. The proposed data-driven methods ERM and GEPM provide even better predictions than the FSPL-β when learned on well-conditioned dataset areas. However, the physics-based WLM performs poorly because of too strong assumptions that are not satisfied for the evaluation environment of municipal utility tunnels. We provide detailed numeric results in Appendix A.

8.3 Memory and Computational Demands of the Models

We provide an insight into the computational and memory requirements as these properties vary significantly with the evaluated methods. Information about the approximate time-per-query of each investigated model is presented. The time is computed by observing the total inference time necessary for processing queries in a given dataset subset divided by the number of queries, taking into account the number of computation threads possibly used. Reported times include overheads incurred by our dataset processing framework, which are, however, constant among the investigated models. The memory requirements were measured offline when the learned models were stored on a disk. The computational environment consists of the HP® Z2 Tower Workstation with the Intel® Core™ i7-10700 CPU with 2.90 GHz base frequency and 64 GB RAM.

Table 2: Performance summary and computational requirements of the evaluated models.

Model	WLM	VWM	GEPL	ERM	FSPL-β
Representative Mean Error† [dB]	−8.7	2.3	1.0	0.6	0.8
Representative Std. Deviation† [dB]	36.7	11.6	10.8	9.9	11.4
Approximate Inference Time [ms]	3	50‡	3	5	< 1
Memory Requirements	4×8 B	6×8 B	>500 MB	>1 GB	1×8 B
Wilcoxon Tournament Rank	5	4	3	2	1
W. Tournament Rank, Interpolation	5	2	3	1	4

† Models learned on subset W and tested on subset all selected as representative.

‡ Experimental implementation with huge optimization potential.

Starting from the simplest, the evaluation of FSPL and FSPL-β models is trivial as they compute the value by a closed-form formula based on a single logarithmic expression. Further, they depend respectively on zero or single real-numbered parameter, which can be encoded as 64 b IEEE 754 floating point number [133]. The proposed WLM depends on four such parameters, which are also processed by a set of closed-form formulas once the shortest signal path is processed into the segments by the method described in Section 6.1.1. The segmentation is the most demanding part, as it relies on frequent dynamic memory allocations for vectors of varying lengths. Observing the implementation, around 5 ms are required per query for a full signal quality inference.

The VWM depends on six real-valued parameters similar to the WLM, and its total computational time is also determined by the shortest signal path processing method. Using our experimental single-threaded Python implementation utilizing NumPy [129] library, a single inference took around 60 ms of which 98 % was consumed by computing variances and means at each window. No effort has been made for optimization so far; significantly faster times can likely be achieved.

The data-driven approaches ERM and GEPM depend on large data representations that exceeded 500 MB with presented training sets. The high memory footprint is caused by keeping original training samples, GPs in the ERM, and transformed UMAP in the GEPM. For the ERM, the training data size directly relates to the performance, as each training sample in the used GP contributes to the final

predicted value at every query. When both learned and tested on the dataset subset C, the inference took about 200 ms on average for the ERM, mostly due to the GP. The occupancy processing took, on average, around 1.5 ms. Finally, the GEPM performed well with 6 ms total inference time of which UMAP consumed 4 ms.

The presented computational data, summarized in Tab. 2, are illustrative to provide a readable overview of the expected computational requirements. The requirements are expected to be decreased by more efficient implementations such as using [134].

8.4 Relative Comparison of the Models

The Wilcoxon matched sample signed-rank test [132] is used to pairwise compare the examined-signal prediction methods by comparing their distributions of mean absolute errors (MAEs) among all cross-validation cases. The test is based on the statistically significant evaluation of differences between distributions' samples matched by the cross-validation scenario, indicating that the model with less median MAE is better than the other model. The MAEs over all the learn-test cross-validation cases form a population of 144 samples per each examined method pair. The results of the pairwise model tests are visualized in Fig. 21, showing that one model is better than the other model with the probability of the assessment indicated by the color.

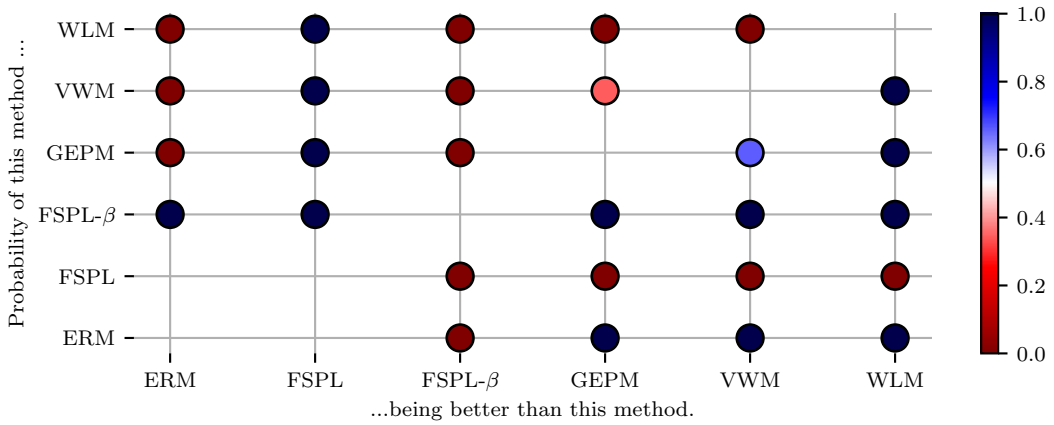

Figure 21: Wilcoxon signed-rank test using all test cases.

Based on the presented results, complex models failed to provide good predictions due to the higher error rates in difficult dataset subsets. Hence, the overall median prediction MAE renders worse than the FSPL-β. Compared to the FSPL-β performance, the high extrapolation error rates might be caused by overfitting the proposed models, as can be noticed for the WLM learned on the dataset area D. However, for the interpolation scenarios where the predictions are evaluated for the measurements from the same dataset areas as the models were learned, the data-driven methods are close to the systematic errors. For example, when the GEPM is learned and tested on the dataset area A, the mean prediction error is only 0.4 dB with the standard deviation 8.3 dB. Since the model provides good performance in extrapolation results as shown in Fig. 18, we reject the hypothesis about the overfitting and assess the Wilcoxon pairwise signed-rank test for the interpolation scenarios only (using the predictions from the diagonals of Fig. 18).

The pairwise comparison using only interpolation scenarios depicted in Fig. 22 suggests that the ERM, VWM, and GEPM outclass the FSPL-β. Even more, the VWM interpolates better than the GEPM, but the ERM provides superior results. Interpreting the evaluations Figs. 21 and 22 as tour-

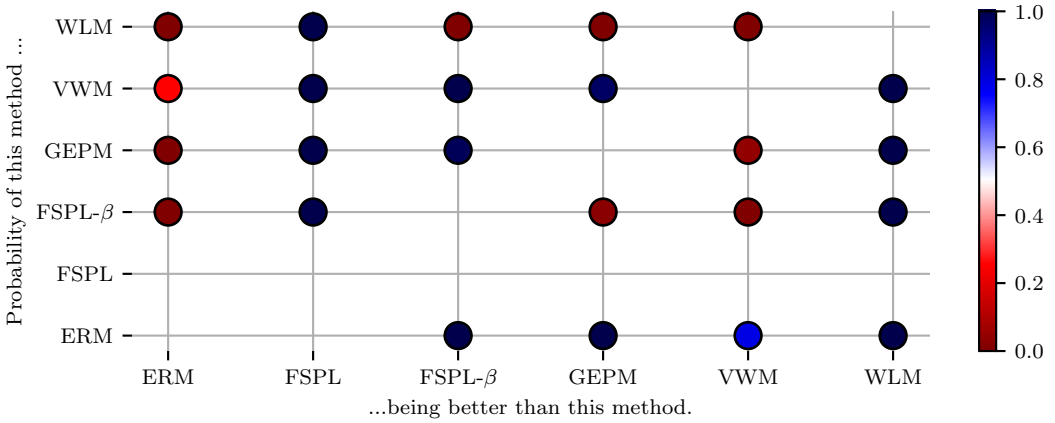

Figure 22: Wilcoxon signed-rank test using interpolation test cases only.

nament results, ordering of the methods can be established, which is summarized in Tab. 2. In this sense, the ERM is best in the interpolation, the VWM second; the FSPL-β is best-extrapolating with the ERM second. Recalling that the GEPM and ERM require a huge memory footprint for the models, the VWM is more suitable for deployment with limited computational resources as it requires only $48\,\mathrm{B}$ for storing six IEEE 754 floating point numbers [133].

8.5 Learning Material Properties of the Environment

The advantage of the proposed WLM is the option for inferring environment material properties by linear regression. The surface roughness Δh, the relative permittivities $\epsilon_r^{(h)}$ and $\epsilon_r^{(v)}$, the surface reflectivity γ, and the tilt θ can be expressed from the latent variables in (34) as

$$\epsilon_r^{(v)} = \frac{1 + \epsilon_*^{(v)^2}}{\epsilon_*^{(v)^2}}, \qquad \epsilon_r^{(h)} = \frac{\epsilon_*^{(h)^2} \pm \sqrt{\epsilon_*^{(h)^4} - 4\epsilon_*^{(h)^2}}}{2}, \tag{46}$$

$$\Delta h = \sqrt{\Delta h^2}, \qquad \gamma = 10^{\log_{10}\gamma}, \qquad \theta = \sqrt{\theta^2}.$$

We determine the properties individually for each subset area as listed in Tab. 3. The permittivities $\epsilon^{(v)}$ and $\epsilon^{(h)}$ were found to be very near to 1, which can be interpreted as the environment being made of vacuum. The values are wrong yet physically feasible as they are always above 1. We estimated the reference values of the properties from the engineering tabulations for common reinforced concrete in Tab. 4. The particular environment of utility tunnels with iron racks stacked inside the tunnel's profile is not tabulated; however, the iron racks should force the overall permittivity towards 1.

The roughness value was imaginary (Δh^2 was negative) in the dataset areas B, D, E, East E, and F. We argue that areas D and E have the most challenging geometry, which causes the waveguide model's assumptions to be violated the most. The linear model is not informed about physically relevant constraints in Tab. 4. Hence the squared terms converged to negative values. Regarding the other areas, the learned value is reasonable. The original method in [110] provides a different method for determining the roughness. The absolute value of the found roughness values adheres to our intuition based on the knowledge that the iron racks were around $1\,\mathrm{m}$ long and the concrete wall itself exhibited large-scale roughness of around $20\,\mathrm{cm}$.

Table 3: Material properties inferred by the proposed WLM.

Area	Subset	$\epsilon_r^{(v)}$ [-]	$\epsilon_r^{(h)}$ [-]	Δh [m]	γ [-]	θ [rad]
KolKN	all	1.000009	1.000000	0.035020	0.897866	0.441363*
KolKN	A1	1.000022	1.000062	0.076419	1.029281	1.278110*
KolKN	A	1.000128	1.000006	0.079746	1.088225	0.693860
KolKN	B	1.000525	1.000003	0.048345*	0.802923	1.532234*
KolKN	C	1.000000	1.000000	0.041845	0.925311	2.518387
KolKN	D	1.000006	1.000000	0.055139*	0.625510	0.649083
KolKN	East	1.000000	1.000000	0.015666*	0.856842	2.883446
KolKN	E	1.000202	1.000003	0.021598*	0.859623	1.114838*
KolKN	F	1.000014	1.000001	0.077788*	0.668298	0.737028
KolKN	G	1.000004	1.000000	0.034045	0.956478	0.754462*
KolKN	H2	1.000034	1.000000	0.092952	0.992130	2.894600
KolKN	West	1.000015	1.000002	0.062626	0.984545	0.694892*

*The squared value Δh^2, θ^2 was negative. Reported value was obtained as $\sqrt{|\square|}$.

Table 4: Reference material properties based on engineering tabulations.

Parameter	$\epsilon_r^{(v)}$ [-]	$\epsilon_r^{(h)}$ [-]	Δh [m]	γ [-]	θ [rad]
Reference Value Interval	$\langle 2, 12\rangle$	$\langle 2, 12\rangle$	$\langle 0, 1\rangle$	$\langle 0.4, 0.7\rangle$	†
Physicaly Meaningful Interval	$\langle 1, \infty\rangle$	$\langle 1, \infty\rangle$	$\langle 0, w\rangle$	$\langle 0, 1\rangle$	$\langle -\pi, \pi\rangle$

† This value cannot be assesed as there is no reference method of computation provided in [110].

Most likely because of local ambient material differences, the reflectivity γ in the areas A and A1 resulted in values larger than 1. That would mean the surface boosts the signal by sole reflection, violating the energy conservation law. We see another instance of ill-fulfilled assumptions about the municipal utility tunnels being an instance of an ideal oversized waveguide. Nevertheless, other areas exhibit the reflectivity learned as might be expected. The reflectivity might be estimated from the LiDAR data; however, that would not be straightforward because of other influences from the surface orientation, related refractive, and reflective optics.

Finally, the value of the environment tilt parameter θ is from the range $0.44\,\mathrm{rad}$ $(25.21°)$ to $2.89\,\mathrm{rad}$ $(165.58°)$ in absolute values. Since the reference methodology for its estimation is unavailable, we can only interpret the found angles as an average angle value determined by the perpendicular iron racks stuck from the corridor wall.

8.6 Discussion

The presented signal propagation modeling is intended to predict the signal availability onboard during the robotic mission in regions that were not yet traversed but observed using onboard exteroceptive sensors attached to a mobile robot. Based on the presented evaluation results, the FSPL-β model provides the best performance in extrapolation scenarios as its simplicity made the predictions conservative. The waveguide theory-based WLM showed to be limited by the too-strict assumptions unsuitable for the examined underground environments. The proposed VWM exhibits better results with consistently low error and no significant bias. The results improve with anonymous latent space embedding of the proposed GEPM, and the model supports extrapolation. However, among the pro-

posed models, the ERM achieves the best results with close performance to the FSPL-β in extrapolation but having supreme interpolation performance. The GEPM was shown as infeasible as better models in all observed criteria exist.

The relatively poor extrapolation results of the proposed models compared to the FSPL-β motivated us to hypothesize that the added regression parameters do not support the extrapolation of the signal propagation. Three factors were contemplated to be the cause of the poor performance. First, disastrous overfitting may render a model instance useless, as was the case of the GEPL model learned on dataset area E. Even in some cases, once the training data is well-determined, like in the subsets A, B, or C, the models do not suffer from overfitting, discarding the hypothesis. Second, the model's additional inputs might contain inherent uncorrelated noise preventing the model from achieving good fits, which is supported by the ERM behavior that should essentially fit the FSPL-β; instead, the extrapolation exhibits slightly worse qualities than the FSPL-β. We acknowledge that the environment exhibited rather uniform widths and heights of the corridor; that is why these parameters were finally omitted from the learning. The two used radius metrics correlate to the curvature and thus are useful, as shown by the results of the GEPM, yet are limited by the underlying method of computation relying on an 8-neighborhood grid, which embeds inherent quantization noise. That is where we see room for improvement. Finally, the third possible cause might be the insufficient geometry characterization along the signal path. As the proposed models systematically dominate the FSPL-β in interpolation scenarios, we consider the representation sufficient. Nevertheless, the prediction errors in extrapolation and interpolation scenarios are already close to the measured systematic error. That finally leads us to the conclusion that although the models may use the environment characterization efficiently, the inherent dataset noise is the limiting factor.

The used environment model, radio technology, and the dataset collection venue condition our findings. The model based on a volumetric 3D grid with the resolution $5\,\mathrm{cm}$ reflects the environment with sufficient detail compared to our expert knowledge. The widths and heights computed as the environment features in the individual waypoints were correct to the error margin of around $10\,\mathrm{cm}$. The radio modules have been considered identical, albeit differences can be observed in the signal strength. Therefore, a calibrated radio might improve the predictions. The municipal utility tunnel venue contained iron racks and an arched cross-section profile that stood against the oversized waveguide model assumptions. Moreover, two fire-proof door systems were present in the corridors, which introduced another source of discrepancy. That definitely led to poor performance of the WLM, yet we consider other linear models suitable for the studied purpose of a robotic mission.

Compared to the related work, similar prediction quality is achieved in [113], where the authors declare the achieved mean absolute error of $10\,\mathrm{dB}$, which is also the case of our models. The advantage of the proposed VWM is in using only 6 real-value parameters, while the VWM extrapolates moderately and interpolates significantly better than the baseline FSPL-β. Analogous to our work, the authors of [113] predicted the signal with similar errors as the baseline FSPL model.

8.7 Deployment

The technical feasibility of the proposed signal propagation models in the communication infrastructure building has been experimentally validated in a real-world exploration mission. Following the field robotics methodology and practice, the system has been integrated and examined in simulation first. Then, we deploy the system with the quadruped robot Spot® [82] in the abandoned gold mine adit Halíře [135] near Jílové u Prahy town in the Central Bohemia region of Czechia. The system integration, together with the description of the used simulation environment, is presented in Section 8.7.1. The report on the field deployment is dedicated to Section 8.7.2.

8.7.1 System Integration in Simulation Environment

The system integration has been done using the existing robotic exploration framework [119] already utilized in several deployments [19,136]. The mapping component of the system is duplicated to provide an independent full 3D volumetric model of the environment together with the environment geometry sampling along a path that is used to determine the environment geometry characterizations. The *Robot Operating System* (ROS) [21] middleware is used for interconnecting individual software components. The learned signal prediction models and breadcrumbs deployment in the exploration are implemented in a single ROS package `zoulamar_dp` that interfaces the presented signal evaluation system and mission controller. The software architecture of the implemented packages, the used interfaces, and ROS models are summarized in Fig. 23.

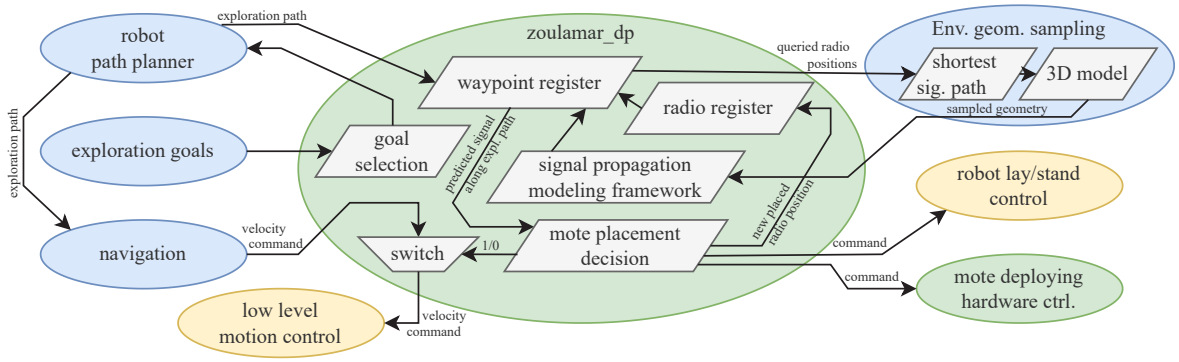

Figure 23: Overview of the system architecture within ROS. The oval shape represents ROS nodes, and the trapezoidal shape denotes individual components related to the proposed signal propagation and deployment of the breadcrumbs. The green outline represents implemented nodes within this thesis. The blue outline indicates components of the existing exploration framework [119], and the yellow outline denotes the interface to the robot hardware.

The communication infrastructure building during the exploration mission directly implements the algorithm presented in Chapter 4. Calling functions for shortest signal path computation and geometry sampling along the path are implemented using request-reply schema with ROS messages. Hence, the system inherently and systematically provides logging and recording. Due to a non-zero time of the mote deployment action, the robot is halted by hijacking the velocity command issued by the navigation subsystem so that the mote is safely deployed from a lower height while the robot sits.

The simulation environment is based on the Simple Two Dimensional Robot (S.T.D.R.) simulator [137] that is augmented to provide 3D scan data. The navigation framework determines the exploration goal based on frontiers inside the traversable area with its separate map. That is why the geometry-sampling mapper had to be tweaked to extend its range beyond the navigation map such that all queried shortest signal paths already have data in requested locations. At the beginning of the mission, the robot is forced for the initial movement such that the map is built even underneath the robot, and the signal propagation path can be determined. A snapshot from the visualized simulation environment is depicted in Fig. 24. Note that the simulation does not provide any signal availability data in the environment, and the simulation tested is only a technical implementation.

8.7.2 System Field Deployment

The real mission was run in the adit Halíře delved into metamorphic rock [135]. The mine consists of around 250 m long central straight corridor with four shorter perpendicular branches. The corridors are of uncommon diamond-shaped profile as illustrated by a LiDAR scan in Fig. 25a as opposed to the

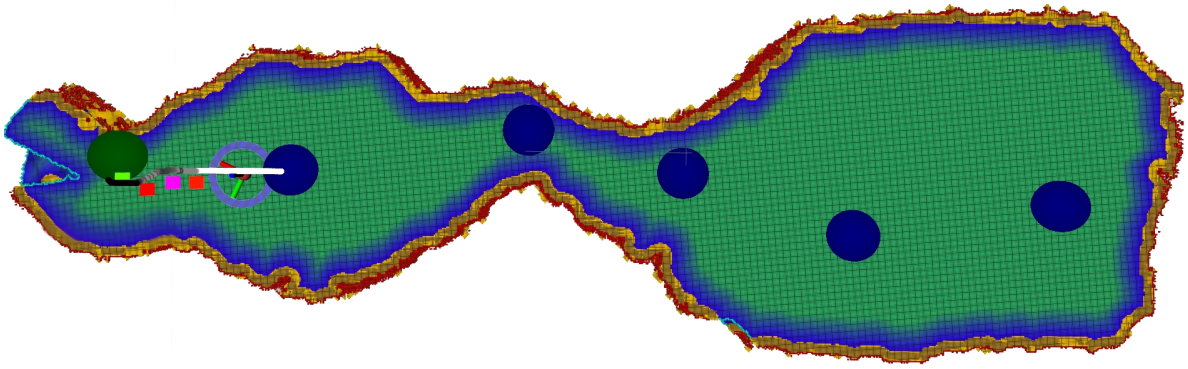

Figure 24: A snapshot from the simulated exploration mission. The colored tiles indicate the predicted signal strength along the current exploration path toward the current exploration goal, which is depicted as a large green sphere. The blue sphere denotes the robot's reckoning about the existing deployed radio. An example of the signal shortest path is a grayscale curve, where black denotes the curve's sharpest part. The environment 3D model, which regards ceilings and walls, is depicted as underlying but rendered from the same viewport.

municipal utility tunnel with the profile depicted in Fig. 25b. As the environment was categorically different from the municipal utility tunnels and due to the limited field deployment time[5] allowed by the Regional Museum Jílové u Prahy [138], it was not feasible to quantify the proposed signal prediction performance in the field.

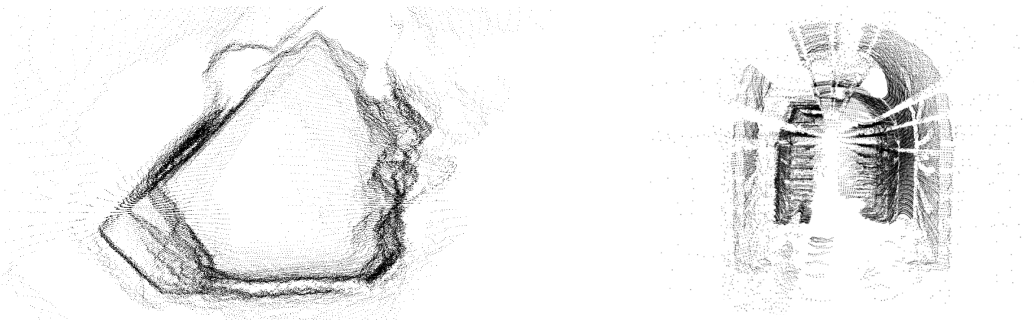

(a) Profile of Halíře mine adit.

(b) Profile of municipal utility tunnels

Figure 25: Tunnel profiles of the encountered environments.

[5] We are grateful to RNDr. Jan Váňa from Museum Jílové u Prahy, who supported the experiment even short before Christmas.

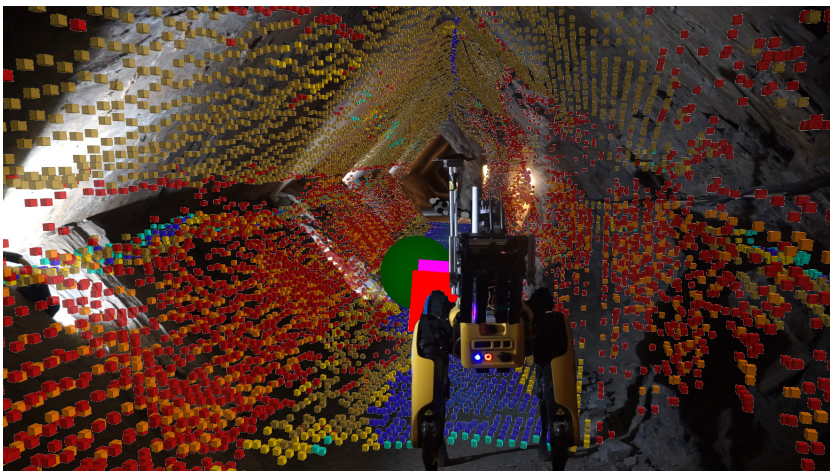

Figure 26: Montage of the robot's perceived model.

(a) Mission start.

(b) First deployed mote.

(c) Second deployed mote.

(d) Robot drops the mote while sitting.

Figure 27: Snaphosts from the real field deployment in Halíře mine adit.

The system developed and integrated with the simulation has been ported to the real robotic system with a minor technical hassle related to the operating system version used on the robot that requires adjusting UMAP [139] and GPy [123] libraries. During the mission, the system provided frequent and correct geometry assessments based on the 3D model, see Fig. 26, which were passed to the proposed signal availability prediction system. We set the requested minimum signal strength to $-60\,\mathrm{dB\,mW}$, which resulted in motes being spaced by approximately $10\,\mathrm{m}$ using the FSPL-β as the signal prediction model. The robot started short into the corridor and followed the exploration strategy, deploying motes when necessary as portrayed in Figs. 27a to 27d. The robot successfully placed motes such that a communication chain of 8 motes was created, covering around $120\,\mathrm{m}$ long section of the corridor with the signal as shown in Fig. 28. No significant message loss rate was apparent.

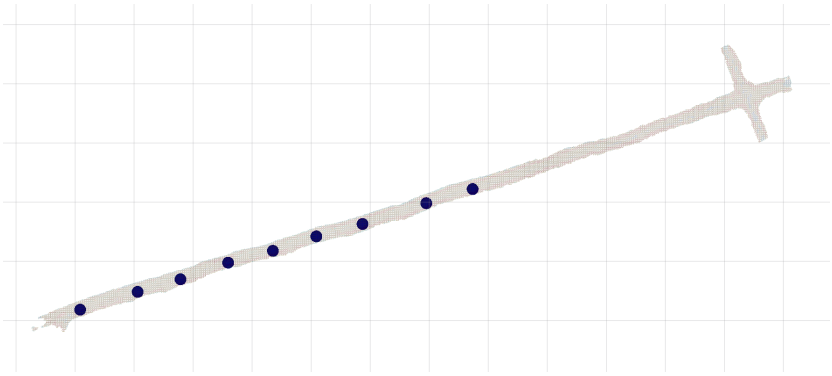

Figure 28: Final explored map with placed communication breadcrumbs depicted as blue disks.

Chapter 9
Conclusion

A solution to low-bandwidth communication infrastructure building during a robotic exploration mission motivated by a Search-and-Rescue mission was developed, tested, and deployed as described in this thesis. The proposed strategy builds upon existing exploration schemes by truncating the exploration path to the farthest waypoint with a good enough predicted signal with regard to known existing radios and the current environment model. An onboard signal propagation model suitable for the intended subterranean robotic mission was sought in the thesis to support assessment in observed yet so far untraversed areas. Based on the related theory review, four candidate models were proposed. The oversized waveguide theory was exploited in the *Waveguide Linear Model* (WLM) and generalized in the *Variance Windowing Model* (VWM). Further, two models fully abstracting the underlying physics, the *Generic Embedding Polynomial Model* (GEPM) based on unsupervised latent space embedding UMAP [122], and the *Evidence Regression Model* (ERM) utilizing the Gaussian process regression [51] were formulated. We evaluated the models on a novel dataset gathered as a part of the thesis, using the developed data evaluation framework, which also exposed the learned models to real-world deployment.

The VWM performed the best among the proposed models, being able to extrapolate the signal with around $11\,\mathrm{dB}$ standard deviation and no significant bias. The interpolation was slightly worse than the ERM, using only six regression parameters as opposed to ERM's up to $2\,\mathrm{GB}$ required memory footprint. Compared to the baseline *Free Space Path Loss* (FSPL) model with a single regression parameter, the attenuation coefficient (FSPL-β), the proposed models exhibited statistically worse extrapolation predictions. However, the differences are negligible compared to the systematic measurement error inherent in the dataset. On the other hand, the proposed VWM, ERM, and GEPL statistically overcome the FSPL-β in the interpolation scenarios. A follow-up method combining the best of all approaches while following rather pessimistic bias should be investigated.

The models used various methods of describing environment geometry along a signal path encoded in a variable-length vector. A slight limitation of the evaluation due to partially uniform model geometry was noticed, but it was shown as insignificant while determining model prediction performance. Besides the main evaluation, we also provided insight into the inference of physically meaningful environment properties inference based on the theoretically motivated WLM. Although physically feasible values were obtained, their correctness was limited to the environment violating the model's assumptions and, in some cases, lack of reference values and methods. Overall, the signal availability processing using contemporary onboard exteroception was confirmed.

Finally, we demonstrate the proposed robotic mission in both simulated and real-world settings in the Halíře adit near Jílové u Prahy. The deployment supports the technical feasibility of computing the environment geometry along the path near the edge of the known region and its subsequent usage in signal prediction. A communication chain covering around $120\,\mathrm{m}$ long tunnel section was created during the exploration mission. We understand the thesis as a gateway to a plethora of possible subsequent works.

References

[1] B. Siciliano, L. Sciavicco, L. Villani, and G. Oriolo. *Robotics: Modelling, Planning and Control*. Advanced Textbooks in Control and Signal Processing. Springer London, 2010.

[2] M. W. Spong, S. Hutchinson, and M. Vidyasagar. *Robot modeling and control*. John Wiley & Sons, 2020.

[3] P. Papadakis. Terrain traversability analysis methods for unmanned ground vehicles: A survey. *Engineering Applications of Artificial Intelligence*, 26(4):1373–1385, 2013.

[4] Clearpath™ Robotics Inc. Husky A200 unmanned ground vehicle. `https://clearpathrobotics.com/husky-unmanned-ground-vehicle-robot/`. [Online; accessed 1-December-2022].

[5] Open Source Robotics Foundation. Turtlebot. `https://www.turtlebot.com/about/`, 2022. [Online; accessed 1-December-2022].

[6] M. Pecka, V. Šalanský, K. Zimmermann, and T. Svoboda. Autonomous flipper control with safety constraints. In *IEEE/RSJ International Conference on Intelligent Robots and Systems (IROS)*, pages 2889–2894, 2016.

[7] M. Pecka, K. Zimmermann, M. Reinstein, and T. Svoboda. Controlling robot morphology from incomplete measurements. *IEEE Transactions on Industrial Electronics*, 64(2):1773–1782, 2017.

[8] P. Čížek, M. Zoula, and J. Faigl. Design, construction, and rough-terrain locomotion control of novel hexapod walking robot with four degrees of freedom per leg. *IEEE Access*, 9:17866–17881, 2021.

[9] M. Zoula. Locomotion control of hexapod walking robot with four degrees of freedom per leg. Bachelor's thesis, Czech Technical University in Prague, Faculty of Electrical Engineering, 2019.

[10] D. G. Macharet and M. F. M. Campos. A survey on routing problems and robotic systems. *Robotica*, 36(12):1781–1803, 2018.

[11] J. M. Mirats Tur and W. Garthwaite. Robotic devices for water main in-pipe inspection: A survey. *Journal of Field Robotics*, 27(4):491–508, 2010.

[12] R. Almadhoun, T. Taha, L. Seneviratne, J. Dias, and G. Cai. A survey on inspecting structures using robotic systems. *International Journal of Advanced Robotic Systems*, 13(6):172988141666366, 2016.

[13] N. Basilico. Recent trends in robotic patrolling. *Current Robotics Reports*, 3(2):65–76, 2022.

[14] R. Montero, J. Victores, S. Martínez, A. Jardón, and C. Balaguer. Past, present and future of robotic tunnel inspection. *Automation in Construction*, 59:99–112, 2015.

[15] L. Huang, M. Zhou, K. Hao, and E. Hou. A survey of multi-robot regular and adversarial patrolling. *IEEE/CAA Journal of Automatica Sinica*, 6(4):894–903, 2019.

[16] D. Portugal and R. Rocha. A survey on multi-robot patrolling algorithms. In L. M. Camarinha-Matos, editor, *Technological Innovation for Sustainability*, pages 139–146, 2011.

[17] F. Amigoni, J. Banfi, and N. Basilico. Multirobot exploration of communication-restricted environments: A survey. *IEEE Intelligent Systems*, 32(6):48–57, 2017.

[18] I. Lluvia, E. Lazkano, and A. Ansuategi. Active mapping and robot exploration: A survey. *Sensors*, 21(7):2445, 2021.

[19] M. Prágr, J. Bayer, and J. Faigl. Autonomous robotic exploration with simultaneous environment and traversability models learning. *Frontiers in Robotics and AI*, 9, 2022.

[20] X. Xu, L. Zhang, J. Yang, C. Cao, W. Wang, Y. Ran, Z. Tan, and M. Luo. A review of multi-sensor fusion SLAM systems based on 3d LIDAR. *Remote Sensing*, 14(12):2835, 2022.

[21] M. Quigley, B. Gerkey, K. Conley, J. Faust, T. Foote, J. Leibs, E. Berger, R. Wheeler, and A. Ng. Ros: an open-source robot operating system. In *IEEE International Conference on Robotics and Automation (ICRA)*, 2009.

[22] L. Bołoz and W. Biały. Automation and robotization of underground mining in poland. *Applied Sciences*, 10(20), 2020.

[23] J. P. Queralta, J. Taipalmaa, B. Can Pullinen, V. K. Sarker, T. Nguyen Gia, H. Tenhunen, M. Gabbouj, J. Raitoharju, and T. Westerlund. Collaborative multi-robot search and rescue: Planning, coordination, perception, and active vision. *IEEE Access*, 8:191617–191643, 2020.

[24] J. Delmerico, S. Mintchev, A. Giusti, B. Gromov, K. Melo, T. Horvat, C. Cadena, M. Hutter, A. Ijspeert, D. Floreano, L. M. Gambardella, R. Siegwart, and D. Scaramuzza. The current state and future outlook of rescue robotics. *Journal of Field Robotics*, 36(7):1171–1191, 2019.

[25] S. Grogan, R. Pellerin, and M. Gamache. The use of unmanned aerial vehicles and drones in search and rescue operations–a survey. *Proceedings of the PROLOG*, 2018.

[26] V. Orekhov and T. Chung. The DARPA subterranean challenge: A synopsis of the circuits stage. *Field Robotics*, 2(1):735–747, 2022.

[27] ZO ČSS 6-01. Býčí skála. `https://www.byciskala.cz/MaRS/index.php`. [Online, in Czech; accessed 1-December-2022].

[28] Colorado School of Mines. Edgar experimental mine. `https://mining.mines.edu/edgar-experimental-mine/`, 2022. [Online; accessed 1-December-2022].

[29] J. N. Aleinikoff, J. John C. Reed, and E. DeWitt. The mount evans batholith in the colorado front range: Revision of its age and reinterpretation of its structure. *Geological Society of America Bulletin*, 105(6):791, 1993.

[30] Collective of Authors. Pittsburgh mining research division. Technical report, U.S. Department of Health and Human Services, Public Health Service, Centers for Disease Control and Prevention, National Institute for Occupational Safety and Health, 2022.

[31] L. F. Ruppert, S. J. Tewalt, L. J. Bragg, and R. N. Wallack. A digital resource model of the upper pennsylvanian pittsburgh coal bed, monongahela group, northern appalachian basin coal region, usa. *International Journal of Coal Geology*, 41(1):3–24, 1999.

[32] Wikipedia. WNP-3 and WNP-5 — Wikipedia, the free encyclopedia. http://en.wikipedia.org/w/index.php?title=WNP-3%20and%20WNP-5&oldid=1120308305, 2022. [Online; accessed 13-November-2022].

[33] Louisville mega cavern. https://louisvillemegacavern.com/, 2022. [Online; accessed 13-November-2022].

[34] N. Kottege, A. Agha, S. Scherer, and J. Faigl. Editorial: Special issue on advancements and lessons learned during phases i and ii of the darpa subterranean challenge. *Field Robotics*, 2:1947–1950, 2022.

[35] T. Rouček, M. Pecka, P. Čížek, T. Petříček, J. Bayer, V. Šalanský, T. Azayev, D. Heřt, M. Petrlík, T. Báča, V. Spurný, V. Krátký, P. Petráček, D. Baril, M. Vaidis, V. Kubelka, F. Pomerleau, J. Faigl, K. Zimmermann, M. Saska, T. Svoboda, and T. Krajník. System for multi-robotic exploration of underground environments CTU-CRAS-NORLAB in the DARPA subterranean challenge. *Field Robotics*, 2:1779–1818, 2022.

[36] J. Faigl, M. Kulich, and L. Přeučil. Goal assignment using distance cost in multi-robot exploration. In *IEEE/RSJ International Conference on Intelligent Robots and Systems (IROS)*, pages 3741–3746, 2012.

[37] M. Meghjani and G. Dudek. Multi-robot exploration and rendezvous on graphs. In *IEEE/RSJ International Conference on Intelligent Robots and Systems (IROS)*, pages 5270–5276, 2012.

[38] B. Yamauchi. A frontier-based approach for autonomous exploration. In *IEEE International Symposium on Computational Intelligence in Robotics and Automation (CIRA)*, pages 146–151, 1997.

[39] H. Moravec. Sensor fusion in certainty grids for mobile robots. *AI Magazine*, 9(2):61–74, 1988.

[40] Z. Zhang. Iterative point matching for registration of free-form curves and surfaces. *International Journal of Computer Vision*, 13(2):119–152, 1994.

[41] S. Yu, C. Fu, A. K. Gostar, and M. Hu. A review on map-merging methods for typical map types in multiple-ground-robot slam solutions. *Sensors*, 20(23), 2020.

[42] J. Kshirsagar, S. Shue, and J. M. Conrad. A survey of implementation of multi-robot simultaneous localization and mapping. In *SoutheastCon 2018*, pages 1–7, 2018.

[43] M. Elhousni and X. Huang. A survey on 3d lidar localization for autonomous vehicles. In *2020 IEEE Intelligent Vehicles Symposium*, pages 1879–1884, 2020.

[44] H. H. González-Baños and J.-C. Latombe. Navigation strategies for exploring indoor environments. *The International Journal of Robotics Research*, 21(10–11):829–848, 2002.

[45] S. Dutta Roy, S. Chaudhury, and S. Banerjee. Active recognition through next view planning: a survey. *Pattern Recognition*, 37(3):429–446, 2004.

[46] J. A. Hartigan and M. A. Wong. Algorithm AS 136: A k-means clustering algorithm. *Applied Statistics*, 28(1):100, 1979.

[47] M. Kulich, J. Faigl, and L. Přeučil. On distance utility in the exploration task. In *IEEE International Conference on Robotics and Automation (ICRA)*, pages 4455–4460, 2011.

[48] A. Bircher, M. Kamel, K. Alexis, H. Oleynikova, and R. Siegwart. Receding horizon "next-best-view" planner for 3d exploration. In *IEEE International Conference on Robotics and Automation (ICRA)*, pages 1462–1468, 2016.

[49] S. M. LaValle et al. Rapidly-exploring random trees: A new tool for path planning. Technical report, Iowa State University, 1998.

[50] B. Charrow, S. Liu, V. Kumar, and N. Michael. Information-theoretic mapping using cauchy-schwarz quadratic mutual information. In *IEEE International Conference on Robotics and Automation (ICRA)*, pages 4791–4798, 2015.

[51] C. E. Rasmussen and C. K. I. Williams. *Gaussian processes for machine learning*. Adaptive Computation and Machine Learning series. MIT Press, 2005.

[52] J. Faigl, M. Kulich, and L. Přeučil. Goal assignment using distance cost in multi-robot exploration. In *IEEE/RSJ International Conference on Intelligent Robots and Systems (IROS)*, pages 3741–3746, 2012.

[53] J. Faigl and M. Kulich. On benchmarking of frontier-based multi-robot exploration strategies. In *European Conference on Mobile Robots (ECMR)*, pages 1–8, 2015.

[54] R. Jonker and A. Volgenant. A shortest augmenting path algorithm for dense and sparse linear assignment problems. *Computing*, 38(4):325–340, 1987.

[55] A. R. Mosteo and L. Montano. A survey of multi-robot task allocation. Technical report, Instituto de Investigacin en Ingenierła de Aragn (I3A), Tech. Rep, 2010.

[56] S. Sariel and T. R. Balch. Efficient bids on task allocation for multi-robot exploration. In *FLAIRS Conference*, pages 116–121, 2006.

[57] M. Dias, R. Zlot, N. Kalra, and A. Stentz. Market-based multirobot coordination: A survey and analysis. *Proceedings of the IEEE*, 94(7):1257–1270, 2006.

[58] M. Berhault, H. Huang, P. Keskinocak, S. Koenig, W. Elmaghraby, P. Griffin, and A. Kleywegt. Robot exploration with combinatorial auctions. In *IEEE/RSJ International Conference on Intelligent Robots and Systems (IROS)*, volume 2, pages 1957–1962 vol.2, 2003.

[59] N. Sullivan, S. Grainger, and B. Cazzolato. Sequential single-item auction improvements for heterogeneous multi-robot routing. *Robotics and Autonomous Systems*, 115:130–142, 2019.

[60] A. Bautin, O. Simonin, and F. Charpillet. Minpos : A novel frontier allocation algorithm for multi-robot exploration. In C.-Y. Su, S. Rakheja, and H. Liu, editors, *Intelligent Robotics and Applications*, pages 496–508, 2012.

[61] J. Bayer and J. Faigl. Decentralized topological mapping for multi-robot autonomous exploration under low-bandwidth communication. In *European Conference on Mobile Robots (ECMR)*, pages 1–7, 2021.

[62] N. Gildert, A. G. Millard, A. Pomfret, and J. Timmis. The need for combining implicit and explicit communication in cooperative robotic systems. *Frontiers in Robotics and AI*, 5:6, 2018.

[63] A. L. Diaz, A. E. Ortega, H. Tingle, A. Pulido, O. Cordero, M. Nelson, N. E. Cocoves, J. Shin, R. R. Carthy, B. E. Wilkinson, and P. G. Ifju. The bathy-drone: An autonomous uncrewed drone-tethered sonar system. *Drones*, 6(10), 2022.

[64] R. Doriya, S. Mishra, and S. Gupta. A brief survey and analysis of multi-robot communication and coordination. In *International Conference on Computing, Communication & Automation*, pages 1014–1021, 2015.

[65] J. Banfi, A. Q. Li, N. Basilico, I. Rekleitis, and F. Amigoni. Asynchronous multirobot exploration under recurrent connectivity constraints. In *IEEE International Conference on Robotics and Automation (ICRA)*, pages 5491–5498, 2016.

[66] S. Jung, D. Choi, S. Song, and H. Myung. Bridge inspection using unmanned aerial vehicle based on hg-slam: Hierarchical graph-based slam. *Remote Sensing*, 12(18), 2020.

[67] F. Voigtländer, A. Ramadan, J. Eichinger, C. Lenz, D. Pensky, and A. Knoll. 5g for robotics: Ultra-low latency control of distributed robotic systems. In *International Symposium on Computer Science and Intelligent Controls (ISCSIC)*, pages 69–72, 2017.

[68] Y. Liu, X. Liu, X. Gao, X. Mu, X. Zhou, O. A. Dobre, and H. V. Poor. Robotic communications for 5G and beyond: Challenges and research opportunities. *IEEE Communications Magazine*, 59(10):92–98, 2021.

[69] M. Tranzatto, T. Miki, M. Dharmadhikari, L. Bernreiter, M. Kulkarni, F. Mascarich, O. Andersson, S. Khattak, M. Hutter, R. Siegwart, and K. Alexis. CERBERUS in the DARPA subterranean challenge. *Science Robotics*, 7(66), 2022.

[70] Rajant. Rajant BreadCrumb® Technologies. `https://rajant.com/products/breadcrumb-wireless-nodes/`. [Online; accessed 30-November-2022].

[71] M. Tranzatto, M. Dharmadhikari, L. Bernreiter, M. Camurri, S. Khattak, F. Mascarich, P. Pfreundschuh, D. Wisth, S. Zimmermann, M. Kulkarni, V. Reijgwart, B. Casseau, T. Homberger, P. De Petris, L. Ott, W. Tubby, G. Waibel, H. Nguyen, C. Cadena, R. Buchanan, L. Wellhausen, N. Khedekar, O. Andersson, L. Zhang, T. Miki, T. Dang, M. Mattamala, M. Montenegro, K. Meyer, X. Wu, A. Briod, M. Mueller, M. Fallon, R. Siegwart, M. Hutter, and K. Alexis. Team cerberus wins the darpa subterranean challenge: Technical overview and lessons learned, 2022.

[72] K. Otsu, S. Tepsuporn, R. Thakker, T. S. Vaquero, J. A. Edlund, W. Walsh, G. Miles, T. Heywood, M. T. Wolf, and A.-A. Agha-Mohammadi. Supervised autonomy for communication-degraded subterranean exploration by a robot team. In *IEEE Aerospace Conference*, pages 1–9, 2020.

[73] M. Tatum. Communications coverage in unknown underground environments. Master's thesis, Carnegie Mellon University, Pittsburgh, Pennsylvania 15213, 2020.

[74] N. Hudson, F. Talbot, M. Cox, J. Williams, T. Hines, A. Pitt, B. Wood, D. Frousheger, K. L. Surdo, T. Molnar, R. Steindl, M. Wildie, I. Sa, N. Kottege, K. Stepanas, E. Hernandez, G. Catt, W. Docherty, B. Tidd, B. Tam, S. Murrell, M. Bessell, L. Hanson, L. Tychsen-Smith, H. Suzuki, L. Overs, F. Kendoul, G. Wagner, D. Palmer, P. Milani, M. O'Brien, S. Jiang, S. Chen, and R. Arkin. Heterogeneous ground and air platforms, homogeneous sensing: Team CSIRO data61's approach to the DARPA subterranean challenge. *Field Robotics*, 2(1):595–636, 2022.

[75] D. Tardioli, L. Riazuelo, D. Sicignano, C. Rizzo, F. Lera, J. L. Villarroel, and L. Montano. Ground robotics in tunnels: Keys and lessons learned after 10 years of research and experiments. *Journal of Field Robotics*, 36(6):1074–1101, 2019.

[76] A. Hrovat, G. Kandus, and T. Javornik. A survey of radio propagation modeling for tunnels. *IEEE Communications Surveys & Tutorials*, 16(2):658–669, 2014.

[77] M. A. Samad, S.-W. Choi, C.-S. Kim, and K. Choi. Wave propagation modeling techniques in tunnel environments: A survey. *IEEE Access*, 2023.

[78] C. Rizzo, D. Tardioli, D. Sicignano, L. Riazuelo, J. L. Villarroel, and L. Montano. Signal-based deployment planning for robot teams in tunnel-like fading environments. *The International Journal of Robotics Research*, 32(12):1381–1397, 2013.

[79] A. Quattrini Li, P. K. Penumarthi, J. Banfi, N. Basilico, J. M. O'Kane, I. Rekleitis, S. Nelakuditi, and F. Amigoni. Multi-robot online sensing strategies for the construction of communication maps. *Autonomous Robots*, 44(3):299–319, 2020.

[80] Czech Technical University in Prague, Faculty of Electrical Engineering. Computational Robotics Laboratory (CRL). `https://comrob.fel.cvut.cz/`. [Online; accessed 1-December-2022].

[81] Czech Technical University in Prague, Faculty of Electrical Engineering. Center for Robotics and Autonomous Systems (CRAS). `https://robotics.fel.cvut.cz/cras/`. [Online; accessed 1-December-2022].

[82] Boston Dynamics. Spot robotic platform. `https://www.bostondynamics.com/products/spot`. [Online; accessed 1-December-2022].

[83] Intel® Corporation. Intel nuc. `https://www.intel.com/content/www/us/en/products/details/nuc.html`. [Online; accessed 1-December-2022].

[84] Ouster, Inc. Ouster os0 lidar. `https://ouster.com/products/scanning-lidar/os0-sensor/`. [Online; accessed 1-December-2022].

[85] Ubiquiti Inc. UISP airMAX. `https://uisp.com/wireless/airmax`. [Online; accessed 1-December-2022].

[86] Mobilicom. Mobilicom MCU 30-Lite. `https://mobilicom.com/products/mcu-30-lite/`. [Online; accessed 1-December-2022].

[87] HOPE Microelectronics CO., Ltd. Rfm69hcw. `https://www.hoperf.com/modules/rf_transceiver/RFM69HCW.html`. [Online; accessed 1-December-2022].

[88] C. Zhou, T. Plass, R. Jacksha, and J. A. Waynert. Rf propagation in mines and tunnels: Extensive measurements for vertically, horizontally, and cross-polarized signals in mines and tunnels. *IEEE Antennas and Propagation Magazine*, 57(4):88–102, 2015.

[89] Collective of Authors. Universal serial bus interfaces for data and power - part 2-1: Universal serial bus specification, revision 2.0. Technical Report IEC 62680-2-1:2015, International Electrotechnical Commission, 2018.

[90] Collective of Authors. Advanced encryption standard (AES). Technical report, National Institute of Standards and Technology, 2001.

[91] J. C. Maxwell. A dynamical theory of the electromagnetic field. *Philosophical Transactions of the Royal Society of London*, 155:459–512, 1865.

[92] C. Shannon. Communication in the presence of noise. *Proceedings of the IRE*, 37(1):10–21, 1949.

[93] W. Sheng, Q. Yang, S. Ci, and N. Xi. Multi-robot area exploration with limited-range communications. In *IEEE/RSJ International Conference on Intelligent Robots and Systems (IROS)*, volume 2, pages 1414–1419, 2004.

[94] M. Rubenstein, C. Ahler, N. Hoff, A. Cabrera, and R. Nagpal. Kilobot: A low cost robot with scalable operations designed for collective behaviors. *Robotics and Autonomous Systems*, 62(7):966–975, 2014.

[95] E. Stump, N. Michael, V. Kumar, and V. Isler. Visibility-based deployment of robot formations for communication maintenance. In *IEEE International Conference on Robotics and Automation (ICRA)*, pages 4498–4505, 2011.

[96] T. Nestmeyer, P. Robuffo Giordano, H. H. Bülthoff, and A. Franchi. Decentralized simultaneous multi-target exploration using a connected network of multiple robots. *Autonomous Robots*, 41(4):989–1011, 2017.

[97] H. Friis. A note on a simple transmission formula. *Proceedings of the IRE*, 34(5):254–256, 1946.

[98] C. Phillips, D. Sicker, and D. Grunwald. A survey of wireless path loss prediction and coverage mapping methods. *IEEE Communications Surveys & Tutorials*, 15(1):255–270, 2013.

[99] S. Jiang, W. Wang, Y. Miao, W. Fan, and A. F. Molisch. A survey of dense multipath and its impact on wireless systems. *IEEE Open Journal of Antennas and Propagation*, 3:435–460, 2022.

[100] D. Micheli, A. Delfini, F. Santoni, F. Volpini, and M. Marchetti. Measurement of electromagnetic field attenuation by building walls in the mobile phone and satellite navigation frequency bands. *IEEE Antennas and Wireless Propagation Letters*, 14:698–702, 2015.

[101] A. Bildea, O. Alphand, F. Rousseau, and A. Duda. Link quality estimation with the gilbert-elliot model for wireless sensor networks. In *Annual International Symposium on Personal, Indoor, and Mobile Radio Communications (PIMRC)*, pages 2049–2054, 2015.

[102] K. A. Remley, H. R. Anderson, and A. Weisshar. Improving the accuracy of ray-tracing techniques for indoor propagation modeling. *IEEE Transactions on Vehicular Technology*, 49(6):2350–2358, 2000.

[103] M. Levy. *Parabolic equation methods for electromagnetic wave propagation*. Electromagnetics and Radar. Institution of Engineering and Technology, 2000.

[104] R. Janaswamy. Path loss predictions in the presence of buildings on flat terrain: a 3-d vector parabolic equation approach. *IEEE Transactions on Antennas and Propagation*, 51(8):1716–1728, 2003.

[105] X. Zhang, N. Sood, and C. D. Sarris. Fast radio-wave propagation modeling in tunnels with a hybrid vector parabolic equation/waveguide mode theory method. *IEEE Transactions on Antennas and Propagation*, 66(12):6540–6551, 2018.

[106] X. Zhang and C. D. Sarris. Vector parabolic equation-based derivation of rectangular waveguide surrogate models of arched tunnels. *IEEE Transactions on Antennas and Propagation*, 66(3):1392–1403, 2018.

[107] C. Yeh and F. Shimabukuro. *The Essence of Dielectric Waveguides*. Springer, 1st edition, 2008.

[108] B. Z. Katsenelenbaum, L. M. del Rio, M. L. Pereyaslavets, M. S. Ayza, and M. K. A. Thumm. *Theory of Nonuniform Waveguides: The cross-section method*. Institution of Electrical Engineers, London, UK, 1998.

[109] N. Marcuvitz. *Waveguide Handbook*. Institution of Electrical Engineers, 1986.

[110] M. D. Bedford and G. A. Kennedy. Modeling microwave propagation in natural caves passages. *IEEE Transactions on Antennas and Propagation*, 62(12):6463–6471, 2014.

[111] A. Emslie, R. Lagace, and P. Strong. Theory of the propagation of UHF radio waves in coal mine tunnels. *IEEE Transactions on Antennas and Propagation*, 23(2):192–205, 1975.

[112] S. M. Aldossari and K.-C. Chen. Machine learning for wireless communication channel modeling: An overview. *Wireless Personal Communications*, 106(1):41–70, 2019.

[113] L. Clark, J. A. Edlund, M. S. Net, T. S. Vaquero, and A.-a. Agha-mohammadi. PropEM-L: Radio propagation environment modeling and learning for communication-aware multi-robot exploration. *arXiv*, page 2205.01267, 2022.

[114] M. Malmirchegini and Y. Mostofi. On the spatial predictability of communication channels. *IEEE Transactions on Wireless Communications*, 11(3):964–978, 2012.

[115] J. Banfi, A. Q. Li, N. Basilico, I. Rekleitis, and F. Amigoni. Multirobot online construction of communication maps. In *IEEE International Conference on Robotics and Automation (ICRA)*, pages 2577–2583, 2017.

[116] W. Luo and K. Sycara. Adaptive Sampling and Online Learning in Multi-Robot Sensor Coverage with Mixture of Gaussian Processes. In *IEEE International Conference on Robotics and Automation (ICRA)*, pages 6359–6364, 2018.

[117] P. K. Penumarthi, A. Q. Li, J. Banfi, N. Basilico, F. Amigoni, J. O'Kane, I. Rekleitis, and S. Nelakuditi. Multirobot exploration for building communication maps with prior from communication models. In *International Symposium on Multi-Robot and Multi-Agent Systems (MRS)*, pages 90–96, 2017.

[118] M. Zoula, M. Prágr, and J. Faigl. On building communication maps in subterranean environments. In *2020 International Conference on Modelling and Simulation for Autonomous Systems*, pages 15–28, 2021.

[119] J. Bayer and J. Faigl. Speeded up elevation map for exploration of large-scale subterranean environments. In *2019 International Conference on Modelling and Simulation for Autonomous Systems*, pages 190–202, 2020.

[120] J. E. Bresenham. Algorithm for computer control of a digital plotter. *IBM Systems Journal*, 4(1):25–30, 1965.

[121] H. Akaike. A new look at the statistical model identification. *IEEE Transactions on Automatic Control*, 19(6):716–723, 1974.

[122] L. McInnes, J. Healy, and J. Melville. Umap: Uniform manifold approximation and projection for dimension reduction, 2018.

[123] GPy. GPy: A gaussian process framework in python. `http://github.com/SheffieldML/GPy`, 2012. [Online; accessed 1-December-2022].

[124] J. Martin, J. Burbank, W. Kasch, and P. D. L. Mills. RFC 5905: Network Time Protocol Version 4: Protocol and Algorithms Specification, 2010.

[125] Kolektory Praha a.s. https://www.kolektory.cz/. [Online, in Czech; accessed 1-December-2022].

[126] F. Pomerleau, F. Colas, R. Siegwart, and S. Magnenat. Comparing ICP Variants on Real-World Data Sets. *Autonomous Robots*, 34(3):133–148, 2013.

[127] G. Van Rossum and F. L. Drake. *Python 3 Reference Manual*. CreateSpace, 2009.

[128] Collective of Authors. *make(1) Linux User's Manual*, 2016.

[129] C. R. Harris, K. J. Millman, S. J. van der Walt, R. Gommers, P. Virtanen, D. Cournapeau, E. Wieser, J. Taylor, S. Berg, N. J. Smith, R. Kern, M. Picus, S. Hoyer, M. H. van Kerkwijk, M. Brett, A. Haldane, J. F. del Río, M. Wiebe, P. Peterson, P. Gérard-Marchant, K. Sheppard, T. Reddy, W. Weckesser, H. Abbasi, C. Gohlke, and T. E. Oliphant. Array programming with NumPy. *Nature*, 585(7825):357–362, 2020.

[130] P. Virtanen, R. Gommers, T. E. Oliphant, M. Haberland, T. Reddy, D. Cournapeau, E. Burovski, P. Peterson, W. Weckesser, J. Bright, S. J. van der Walt, M. Brett, J. Wilson, K. J. Millman, N. Mayorov, A. R. J. Nelson, E. Jones, R. Kern, E. Larson, C. J. Carey, İ. Polat, Y. Feng, E. W. Moore, J. VanderPlas, D. Laxalde, J. Perktold, R. Cimrman, I. Henriksen, E. A. Quintero, C. R. Harris, A. M. Archibald, A. H. Ribeiro, F. Pedregosa, P. van Mulbregt, and SciPy 1.0 Contributors. SciPy 1.0: Fundamental Algorithms for Scientific Computing in Python. *Nature Methods*, 17:261–272, 2020.

[131] O. Tange. Gnu parallel 20220922 ('elizabeth'), 2022. GNU Parallel is a general parallelizer to run multiple serial command line programs in parallel without changing them.

[132] F. Wilcoxon. Individual comparisons by ranking methods. *Biometrics Bulletin*, 1(6):80–83, 1945.

[133] IEEE standard for floating-point arithmetic. *IEEE Std 754-2019*, pages 1–84, 2019.

[134] A. Cully, K. Chatzilygeroudis, F. Allocati, and J.-B. Mouret. Limbo: A Flexible High-performance Library for Gaussian Processes modeling and Data-Efficient Optimization. *The Journal of Open Source Software*, 3(26):545, 2018.

[135] Regionální muzeum v Jílovém u Prahy. Štola Halíře. http://www.muzeumjilove.cz/stoly/stola-halire/. [Online; accessed 1-December-2022].

[136] M. Prágr, J. Bayer, and J. Faigl. Autonomous exploration with online learning of traversable yet visually rigid obstacles. *Autonomous Robots*, 9, 2022.

[137] Simple two dimensional robot simulator. http://stdr-simulator-ros-pkg. [Online; accessed 1-December-2022].

[138] Regionální muzeum v Jílovém u Prahy. http://www.muzeumjilove.cz/. [Online, in Czech; accessed 1-December-2022].

[139] L. McInnes et al. Umap github repository. https://github.com/lmcinnes/umap. [Online; accessed 1-December-2022].

Appendix A
Tabelated Crossvalidation Results

The appendix lists the results of all presented signal propagation models in the proposed extended cross-validation scheme. The following tables present the cross-validation results for particular models as denoted in the caption, which also denotes the computation stage in the evaluation system `zoulamar_dp` described in Section 7.2. Columns are annotated with the following abbreviations. The training and testing subsets are marked as **L** or **T**, respectively. **ME** denotes the prediction mean error achieved at the given case, **SD** is the prediction standard deviation, and **RMSE** is the prediction root-mean-square-error. The statistic about method pessimism is denoted **P** and represents the ratio of the predictions underestimating the signal gain with regard to the ground truth.

WLM (`.../Augment.segmentation/Forge/Bedford`)

L	T	ME	SD	RE	P	L	T	ME	SD	RE	P
A	A	−3.04	17.25	17.51	0.39	Ea	A	−5.95	34.36	34.87	0.31
A	A1	−12.65	13.73	18.67	0.17	Ea	A1	−20.70	41.44	46.32	0.12
A	B	−24.74	26.79	36.47	0.19	Ea	B	−13.53	26.88	30.09	0.32
A	C	−36.64	26.46	45.20	0.08	Ea	C	−22.68	32.64	39.75	0.25
A	D	−29.66	24.97	38.77	0.22	Ea	D	−24.73	49.58	55.41	0.13
A	E	36.74	21.59	42.61	0.89	Ea	E	1.98	4.67	5.08	0.44
A	Ea	−5.31	45.72	46.02	0.47	Ea	Ea	−11.22	27.28	29.50	0.35
A	F	−75.40	20.18	78.05	0.00	Ea	F	−22.21	29.03	36.55	0.29
A	G	59.72	30.65	67.13	0.96	Ea	G	14.68	20.81	25.47	0.71
A	H2	−59.16	10.73	60.13	0.00	Ea	H2	−48.69	10.82	49.88	0.00
A	We	−31.05	25.79	40.36	0.11	Ea	We	−17.64	53.29	56.13	0.22
A	al	−24.31	34.08	41.86	0.20	Ea	al	−14.56	49.14	51.25	0.25
A1	A	17.37	22.36	28.31	0.77	F	A	−8.23	32.63	33.65	0.41
A1	A1	−2.77	14.74	15.00	0.51	F	A1	−39.18	23.64	45.75	0.06
A1	B	−7.16	33.17	33.94	0.34	F	B	7.85	38.88	39.67	0.64
A1	C	−18.32	36.42	40.77	0.32	F	C	−0.74	53.72	53.72	0.47
A1	D	−18.93	25.70	31.92	0.26	F	D	−57.05	19.65	60.34	0.00
A1	E	60.09	20.64	63.54	1.00	F	E	−28.30	17.05	33.04	0.11
A1	Ea	15.62	51.43	53.75	0.57	F	Ea	−10.23	38.99	40.31	0.39
A1	F	−55.36	21.99	59.57	0.03	F	F	−2.86	18.54	18.76	0.53
A1	G	87.02	35.11	93.83	0.96	F	G	0.19	21.81	21.81	0.61
A1	H2	−45.54	10.33	46.69	0.00	F	H2	−36.29	22.05	42.46	0.00
A1	We	−15.53	34.91	38.21	0.35	F	We	−13.57	45.49	47.47	0.32
A1	al	−7.54	41.77	42.45	0.40	F	al	−13.93	43.75	45.91	0.33
B	A	−16.47	25.11	30.03	0.29	G	A	−47.14	11.41	48.50	0.00
B	A1	−39.71	16.64	43.05	0.00	G	A1	−50.96	9.90	51.91	0.00
B	B	−8.91	28.33	29.70	0.38	G	B	−38.87	17.09	42.46	0.05
B	C	−19.71	34.33	39.59	0.31	G	C	−53.83	15.58	56.04	0.00
B	D	−50.03	22.12	54.70	0.09	G	D	−66.54	13.02	67.80	0.00
B	E	3.76	7.01	7.96	0.67	G	E	−27.68	5.36	28.20	0.00
B	Ea	−8.09	31.45	32.47	0.36	G	Ea	−38.35	21.77	44.09	0.03
B	F	−10.74	26.09	28.21	0.39	G	F	−62.88	15.47	64.76	0.00
B	G	11.24	20.88	23.71	0.61	G	G	−1.90	17.58	17.69	0.50
B	H2	−41.85	17.87	45.50	0.00	G	H2	−70.65	7.22	71.02	0.00

WLM (.../Augment.segmentation/Forge/Bedford)

L	T	ME	SD	RE	P	L	T	ME	SD	RE	P
B	We	−26.46	30.51	40.38	0.21	G	We	−56.89	18.97	59.97	0.00
B	al	−22.13	31.77	38.72	0.24	G	al	−52.94	23.04	57.74	0.01
C	A	12.30	44.04	45.72	0.53	H2	A	119	54.97	131	0.99
C	A1	−7.44	48.67	49.24	0.17	H2	A1	69.18	46.08	83.12	0.95
C	B	−7.22	32.69	33.48	0.36	H2	B	67.04	76.84	102	0.86
C	C	−16.68	33.38	37.32	0.35	H2	C	44.84	74.46	86.92	0.67
C	D	2.21	71.49	71.53	0.35	H2	D	113	94.54	147	1.00
C	E	57.55	8.44	58.17	1.00	H2	E	191	30.51	193	1.00
C	Ea	15.69	43.79	46.51	0.59	H2	Ea	136	123	183	0.88
C	F	6.64	52.32	52.74	0.56	H2	F	95.59	83.20	127	0.81
C	G	49.62	27.93	56.94	0.96	H2	G	311	78.83	321	1.00
C	H2	−35.61	25.33	43.69	0.18	H2	H2	−0.11	19.83	19.83	0.45
C	We	−6.65	59.27	59.64	0.33	H2	We	54.68	79.15	96.20	0.74
C	al	1.91	59.71	59.74	0.41	H2	al	79.72	109	135	0.81
D	A	83.17	55.70	100	0.92	We	A	9.26	23.62	25.37	0.61
D	A1	23.28	34.44	41.57	0.72	We	A1	−10.62	17.34	20.34	0.22
D	B	65.74	68.78	95.14	0.78	We	B	−9.22	31.42	32.75	0.34
D	C	62.91	98.86	117	0.59	We	C	−20.52	32.73	38.63	0.30
D	D	−3.96	13.01	13.60	0.35	We	D	−17.93	27.45	32.79	0.35
D	E	56.38	7.05	56.82	1.00	We	E	55.05	14.51	56.93	1.00
D	Ea	59.66	68.67	90.97	0.80	We	Ea	12.85	44.02	45.86	0.59
D	F	11.18	27.23	29.43	0.74	We	F	−31.89	30.44	44.09	0.16
D	G	115	41.68	123	1.00	We	G	68.60	31.22	75.37	0.96
D	H2	0.40	42.08	42.08	0.45	We	H2	−42.93	12.10	44.60	0.00
D	We	50.10	82.64	96.64	0.66	We	We	−17.15	30.73	35.19	0.30
D	al	51.19	77.92	93.23	0.70	We	al	−8.75	36.67	37.70	0.37
E	A	−19.07	19.22	27.07	0.17	al	A	−2.35	22.69	22.81	0.46
E	A1	−36.86	12.51	38.92	0.00	al	A1	−22.42	17.07	28.18	0.10
E	B	−15.96	25.16	29.79	0.28	al	B	−10.38	28.48	30.31	0.35
E	C	−27.22	30.31	40.74	0.21	al	C	−20.58	33.18	39.05	0.29
E	D	−51.66	13.90	53.50	0.00	al	D	−34.32	21.22	40.35	0.13
E	E	−1.15	3.94	4.10	0.33	al	E	25.38	6.91	26.31	1.00
E	Ea	−14.70	26.44	30.25	0.26	al	Ea	−0.81	33.25	33.26	0.49
E	F	−34.71	18.07	39.14	0.01	al	F	−31.71	23.37	39.39	0.08
E	G	14.54	20.69	25.29	0.68	al	G	37.08	24.94	44.68	0.96
E	H2	−50.28	10.36	51.33	0.00	al	H2	−44.64	11.48	46.09	0.00
E	We	−31.78	26.31	41.26	0.14	al	We	−21.06	29.64	36.36	0.25
E	al	−27.95	27.06	38.90	0.16	al	al	−15.73	31.59	35.29	0.31

VWM (.../Augment.windowing/Forge.rad_only/PolyForWindowing)

L	T	ME	SD	RE	P	L	T	ME	SD	RE	P
A	A	0.52	8.63	8.64	0.48	Ea	A	−10.37	10.04	14.44	0.16
A	A1	2.51	9.84	10.16	0.62	Ea	A1	−5.54	9.22	10.76	0.29
A	B	16.97	13.25	21.53	0.89	Ea	B	5.48	9.18	10.69	0.74
A	C	−0.37	10.99	10.99	0.50	Ea	C	−9.53	9.35	13.36	0.15
A	D	−16.52	7.50	18.14	0.00	Ea	D	−26.67	8.62	28.02	0.00
A	E	12.73	3.79	13.28	1.00	Ea	E	2.67	3.62	4.50	0.67
A	Ea	6.45	13.02	14.53	0.68	Ea	Ea	−0.13	10.27	10.27	0.48
A	F	12.48	13.70	18.53	0.80	Ea	F	−6.01	11.29	12.79	0.18
A	G	12.32	8.90	15.20	0.86	Ea	G	10.61	11.90	15.94	0.79

VWM (.../Augment.windowing/Forge.rad_only/PolyForWindowing)

L	T	ME	SD	RE	P	L	T	ME	SD	RE	P
A	H2	−7.98	8.15	11.40	0.24	Ea	H2	−16.94	5.47	17.80	0.00
A	We	−1.63	10.35	10.48	0.43	Ea	We	−10.62	10.14	14.68	0.16
A	al	−0.14	11.75	11.75	0.47	Ea	al	−8.75	11.52	14.47	0.22
A1	A	2.05	10.74	10.93	0.61	F	A	−30.11	42.75	52.29	0.29
A1	A1	−0.24	8.62	8.62	0.54	F	A1	17.85	16.84	24.54	0.86
A1	B	14.58	12.10	18.94	0.90	F	B	8.19	26.56	27.80	0.66
A1	C	−0.97	9.68	9.73	0.47	F	C	−19.46	56.54	59.80	0.49
A1	D	−22.32	9.28	24.17	0.00	F	D	−2.43	11.46	11.72	0.52
A1	E	10.74	4.04	11.47	1.00	F	E	9.38	2.77	9.78	1.00
A1	Ea	6.65	15.60	16.96	0.74	F	Ea	−21.57	63.05	66.64	0.52
A1	F	−21.38	11.89	24.47	0.07	F	F	1.17	9.79	9.86	0.52
A1	G	24.47	15.14	28.77	0.93	F	G	−70.73	46.64	84.72	0.07
A1	H2	−11.47	5.67	12.80	0.00	F	H2	6.41	11.79	13.42	0.61
A1	We	−2.68	10.99	11.31	0.44	F	We	−12.10	47.52	49.03	0.49
A1	al	−1.23	13.65	13.70	0.48	F	al	−14.72	51.14	53.21	0.49
B	A	−20.86	11.82	23.97	0.06	G	A	−73.30	79.50	108	0.07
B	A1	−10.98	10.51	15.20	0.12	G	A1	−74.26	73.81	105	0.08
B	B	0.57	8.38	8.40	0.55	G	B	−105	59.88	121	0.00
B	C	−12.01	9.99	15.62	0.12	G	C	−180	162	242	0.00
B	D	−30.10	8.65	31.32	0.00	G	D	−169	95.41	194	0.00
B	E	−8.74	3.52	9.42	0.00	G	E	4.52	12.41	13.21	0.67
B	Ea	−13.26	17.35	21.83	0.28	G	Ea	−114	183	216	0.10
B	F	−3.10	13.16	13.52	0.42	G	F	−581	189	611	0.00
B	G	−19.32	9.65	21.60	0.04	G	G	−0.17	6.27	6.27	0.50
B	H2	−20.08	5.57	20.84	0.00	G	H2	−137	28.34	140	0.00
B	We	−14.80	11.49	18.74	0.11	G	We	−147	140	203	0.02
B	al	−15.29	13.34	20.29	0.14	G	al	−140	157	211	0.04
C	A	−2.19	9.68	9.92	0.44	H2	A	39.78	35.10	53.05	0.91
C	A1	0.03	9.34	9.34	0.51	H2	A1	26.24	20.85	33.51	0.95
C	B	13.72	9.92	16.93	0.92	H2	B	28.49	23.40	36.87	0.92
C	C	−0.46	8.43	8.44	0.51	H2	C	0.44	35.72	35.72	0.66
C	D	−18.24	8.75	20.23	0.00	H2	D	−4.61	9.58	10.63	0.35
C	E	7.15	3.68	8.04	1.00	H2	E	66.92	15.20	68.62	1.00
C	Ea	8.61	11.33	14.23	0.79	H2	Ea	76.89	69.83	104	0.95
C	F	10.52	12.70	16.49	0.81	H2	F	33.44	20.43	39.19	0.94
C	G	20.41	14.33	24.94	0.86	H2	G	173	60.89	183	1.00
C	H2	−9.33	5.56	10.86	0.08	H2	H2	0.32	5.88	5.89	0.49
C	We	−2.32	9.43	9.71	0.43	H2	We	9.94	34.47	35.88	0.70
C	al	−0.28	11.55	11.56	0.49	H2	al	27.03	53.29	59.75	0.77
D	A	23.69	58.32	62.95	0.76	We	A	0.24	9.16	9.16	0.49
D	A1	38.77	38.39	54.56	0.86	We	A1	3.07	9.72	10.19	0.61
D	B	14.67	35.42	38.34	0.65	We	B	16.93	10.46	19.90	0.93
D	C	−50.23	115	125	0.41	We	C	1.41	8.71	8.82	0.58
D	D	−1.59	9.14	9.27	0.30	We	D	−13.92	8.87	16.51	0.00
D	E	100	21.90	103	1.00	We	E	10.48	3.67	11.11	1.00
D	Ea	63.92	71.88	96.19	0.81	We	Ea	11.27	12.13	16.56	0.84
D	F	27.58	21.84	35.18	0.87	We	F	22.34	14.97	26.89	0.92
D	G	150	42.04	156	1.00	We	G	20.77	12.88	24.44	0.89
D	H2	−3.02	12.45	12.81	0.47	We	H2	−5.94	6.10	8.52	0.16
D	We	−20.09	93.53	95.66	0.52	We	We	0.03	9.06	9.06	0.51
D	al	3.32	93.59	93.65	0.61	We	al	2.30	11.60	11.82	0.57
E	A	−312	446	544	0.19	al	A	−1.04	9.18	9.24	0.44

VWM (`.../Augment.windowing/Forge.rad_only/PolyForWindowing`)

L	T	ME	SD	RE	P	L	T	ME	SD	RE	P
E	A1	48.65	88.10	101	0.65	al	A1	2.30	9.18	9.46	0.60
E	B	−181	341	386	0.36	al	B	16.26	10.22	19.21	0.93
E	C	−588	1097	1244	0.40	al	C	0.75	8.74	8.77	0.55
E	D	196	69.81	208	0.96	al	D	−16.44	8.12	18.34	0.00
E	E	−0.70	3.25	3.32	0.44	al	E	9.15	3.94	9.96	1.00
E	Ea	−95.41	317	331	0.40	al	Ea	5.40	11.44	12.65	0.66
E	F	177	255	310	0.78	al	F	3.69	10.97	11.57	0.64
E	G	−129	105	167	0.21	al	G	10.94	10.00	14.82	0.82
E	H2	78.61	142	163	0.75	al	H2	−7.05	5.81	9.13	0.14
E	We	−345	848	915	0.39	al	We	−0.99	9.25	9.30	0.47
E	al	−257	750	793	0.42	al	al	−0.11	10.61	10.61	0.48

GEPM (`.../Augment.histogram/Forge/Umap/Poly.2x`)

L	T	ME	SD	RE	P	L	T	ME	SD	RE	P
A	A	0.39	8.34	8.35	0.48	Ea	A	−5.84	9.76	11.37	0.29
A	A1	3.03	9.33	9.81	0.65	Ea	A1	−5.37	9.49	10.91	0.26
A	B	19.70	9.80	22.00	0.96	Ea	B	8.58	11.26	14.15	0.81
A	C	0.44	12.74	12.75	0.49	Ea	C	−1.60	9.91	10.04	0.47
A	D	−13.67	15.57	20.72	0.09	Ea	D	−21.31	9.75	23.44	0.00
A	E	13.47	4.07	14.07	1.00	Ea	E	2.40	3.67	4.38	0.67
A	Ea	10.39	13.83	17.30	0.77	Ea	Ea	−0.27	10.65	10.66	0.52
A	F	−6.81	10.64	12.64	0.09	Ea	F	−13.59	10.78	17.35	0.07
A	G	14.56	8.47	16.84	0.93	Ea	G	5.10	10.18	11.39	0.68
A	H2	−7.59	8.04	11.06	0.24	Ea	H2	−16.27	5.67	17.22	0.00
A	We	7.98	22.69	24.06	0.59	Ea	We	−5.52	11.78	13.00	0.31
A	al	6.33	21.64	22.55	0.58	Ea	al	−4.78	12.61	13.48	0.36
A1	A	−17.52	16.15	23.83	0.18	F	A	11.89	10.94	16.16	0.88
A1	A1	1.74	10.05	10.20	0.59	F	A1	18.80	10.96	21.76	0.96
A1	B	12.54	19.07	22.82	0.87	F	B	38.53	21.08	43.92	1.00
A1	C	−15.42	17.98	23.69	0.15	F	C	22.10	22.45	31.50	0.95
A1	D	−33.84	12.83	36.19	0.00	F	D	5.81	32.66	33.18	0.43
A1	E	7.85	5.14	9.38	1.00	F	E	22.93	7.94	24.27	1.00
A1	Ea	−4.21	24.82	25.18	0.47	F	Ea	30.81	23.82	38.95	0.95
A1	F	−22.58	13.05	26.07	0.06	F	F	1.16	10.59	10.65	0.42
A1	G	3.35	7.84	8.53	0.71	F	G	29.71	12.23	32.12	1.00
A1	H2	−8.47	8.34	11.89	0.12	F	H2	10.65	7.00	12.75	0.92
A1	We	−5.97	24.98	25.68	0.45	F	We	36.49	51.88	63.43	0.88
A1	al	−8.60	24.66	26.12	0.40	F	al	30.88	45.77	55.22	0.85
B	A	−15.55	15.18	21.73	0.17	G	A	−29.19	14.95	32.80	0.03
B	A1	−3.12	12.52	12.90	0.39	G	A1	−21.11	24.36	32.23	0.20
B	B	0.79	8.50	8.53	0.57	G	B	1.69	60.70	60.72	0.86
B	C	−9.65	15.37	18.15	0.30	G	C	−47.54	38.70	61.30	0.08
B	D	−26.42	19.66	32.93	0.00	G	D	−80.41	28.96	85.47	0.00
B	E	−0.87	5.66	5.73	0.56	G	E	1.84	7.95	8.16	0.44
B	Ea	−11.64	16.59	20.27	0.29	G	Ea	−19.54	33.94	39.16	0.33
B	F	−17.16	10.48	20.11	0.07	G	F	−41.86	22.76	47.65	0.00
B	G	−9.68	11.71	15.20	0.11	G	G	0.03	7.24	7.24	0.50
B	H2	−14.84	10.27	18.04	0.06	G	H2	−33.31	28.10	43.58	0.08
B	We	−20.03	17.82	26.80	0.12	G	We	−17.65	27.32	32.53	0.25
B	al	−17.07	17.75	24.63	0.16	G	al	−25.99	34.99	43.59	0.22

GEPM (`.../Augment.histogram/Forge/Umap/Poly.2x`)

L	T	ME	SD	RE	P	L	T	ME	SD	RE	P
C	A	−3.28	9.66	10.21	0.35	H2	A	62.04	65.78	90.42	0.81
C	A1	0.94	9.17	9.22	0.59	H2	A1	16.35	11.80	20.16	0.95
C	B	13.10	9.45	16.16	0.94	H2	B	44.93	21.16	49.67	1.00
C	C	−0.51	8.81	8.83	0.51	H2	C	47.47	66.43	81.64	0.82
C	D	−20.13	8.83	21.98	0.00	H2	D	25.00	20.05	32.05	0.96
C	E	8.66	3.67	9.41	1.00	H2	E	34.24	11.25	36.04	1.00
C	Ea	2.30	11.44	11.67	0.55	H2	Ea	58.13	62.51	85.36	0.90
C	F	−9.78	10.18	14.12	0.07	H2	F	46.54	35.94	58.80	0.98
C	G	8.32	9.47	12.61	0.82	H2	G	15.97	24.67	29.39	0.71
C	H2	−10.24	5.55	11.65	0.00	H2	H2	0.49	5.97	5.99	0.47
C	We	−3.39	9.91	10.47	0.39	H2	We	75.60	91.23	118	0.90
C	al	−2.70	11.02	11.35	0.40	H2	al	63.22	85.63	106	0.87
D	A	14.10	13.58	19.58	0.86	We	A	1.80	9.71	9.87	0.59
D	A1	14.96	15.85	21.79	0.82	We	A1	4.47	9.03	10.07	0.69
D	B	27.78	27.31	38.96	0.83	We	B	16.59	10.17	19.46	0.95
D	C	−1.84	28.26	28.32	0.54	We	C	1.82	9.82	9.99	0.59
D	D	−2.88	6.89	7.47	0.35	We	D	−14.80	8.76	17.20	0.09
D	E	37.17	4.08	37.40	1.00	We	E	13.77	3.94	14.32	1.00
D	Ea	14.21	24.82	28.60	0.75	We	Ea	6.43	11.30	13.00	0.73
D	F	14.69	12.25	19.13	0.91	We	F	−3.57	10.49	11.08	0.18
D	G	35.32	7.87	36.19	1.00	We	G	11.27	9.20	14.55	0.82
D	H2	1.61	18.59	18.66	0.49	We	H2	−7.21	5.56	9.10	0.14
D	We	−5.40	36.84	37.23	0.60	We	We	0.00	9.58	9.58	0.51
D	al	1.55	32.92	32.96	0.65	We	al	0.99	10.80	10.84	0.53
E	A	−466	493	678	0.01	al	A	0.69	9.81	9.84	0.51
E	A1	−263	290	391	0.00	al	A1	3.68	9.06	9.78	0.68
E	B	−423	411	589	0.05	al	B	15.63	10.02	18.57	0.94
E	C	−1015	1130	1519	0.01	al	C	1.33	9.45	9.55	0.57
E	D	−175	105	204	0.00	al	D	−16.29	9.03	18.63	0.00
E	E	−0.48	4.03	4.06	0.44	al	E	12.52	3.98	13.14	1.00
E	Ea	−492	552	739	0.05	al	Ea	5.32	11.32	12.51	0.68
E	F	−82.11	92.96	124	0.06	al	F	−4.92	10.39	11.50	0.13
E	G	−554	372	668	0.00	al	G	10.17	9.36	13.82	0.82
E	H2	−353	305	467	0.00	al	H2	−7.94	5.47	9.65	0.14
E	We	−742	933	1192	0.00	al	We	−0.90	9.62	9.66	0.48
E	al	−640	851	1065	0.02	al	al	0.01	10.73	10.73	0.50

ERM (`.../Augment.occupancy/Forge/GP.mesas`)

L	T	ME	SD	RE	P	L	T	ME	SD	RE	P
A	A	0.42	8.01	8.02	0.53	E	E	−0.61	3.33	3.39	0.44
A	A1	0.78	8.61	8.65	0.60	E	Ea	−6.87	16.24	17.63	0.36
A	B	−0.41	29.71	29.71	0.50	E	F	−19.08	10.35	21.70	0.07
A	C	−2.64	22.87	23.02	0.43	E	G	−8.37	9.92	12.98	0.11
A	D	−17.26	8.40	19.19	0.00	E	H2	−13.26	8.81	15.92	0.08
A	E	18.94	3.92	19.34	1.00	E	We	−10.12	16.11	19.03	0.29
A	Ea	2.26	20.13	20.26	0.52	E	al	−10.30	16.10	19.12	0.28
A	F	−6.56	10.68	12.54	0.20	Ea	A	1.51	11.29	11.39	0.58
A	G	3.56	18.52	18.86	0.79	Ea	A1	4.30	9.44	10.37	0.68
A	H2	−13.92	19.54	23.99	0.12	Ea	B	2.17	8.42	8.69	0.63
A	We	−3.27	18.85	19.13	0.39	Ea	C	−14.04	25.38	29.01	0.22

ERM (`.../Augment.occupancy/Forge/GP.mesas`)

L	T	ME	SD	RE	P	L	T	ME	SD	RE	P
A	al	−3.00	19.52	19.75	0.39	Ea	D	−17.61	9.32	19.92	0.00
A1	A	−19.31	29.10	34.93	0.27	Ea	E	12.02	3.56	12.53	1.00
A1	A1	0.17	8.69	8.70	0.55	Ea	Ea	−0.04	8.57	8.57	0.52
A1	B	4.83	19.60	20.19	0.69	Ea	F	−4.12	9.85	10.68	0.25
A1	C	−26.53	39.50	47.58	0.25	Ea	G	6.98	10.96	12.99	0.79
A1	D	−21.30	8.39	22.89	0.00	Ea	H2	−9.64	10.43	14.20	0.22
A1	E	8.18	4.09	9.14	1.00	Ea	We	−9.02	20.18	22.10	0.28
A1	Ea	−13.06	33.39	35.85	0.47	Ea	al	−7.17	18.71	20.03	0.34
A1	F	−8.30	10.39	13.29	0.10	F	A	6.81	11.06	12.99	0.72
A1	G	−22.12	25.27	33.59	0.29	F	A1	14.57	10.07	17.71	0.93
A1	H2	−10.49	7.06	12.64	0.04	F	B	24.97	8.47	26.37	0.99
A1	We	−19.93	32.04	37.73	0.23	F	C	11.72	9.93	15.36	0.88
A1	al	−18.23	31.77	36.63	0.26	F	D	−7.35	9.53	12.03	0.22
B	A	−17.85	10.72	20.82	0.07	F	E	19.65	3.50	19.96	1.00
B	A1	−10.27	9.49	13.99	0.12	F	Ea	13.90	12.74	18.86	0.85
B	B	0.48	8.52	8.53	0.53	F	F	1.15	10.06	10.12	0.44
B	C	−16.29	12.49	20.53	0.08	F	G	16.78	9.41	19.23	1.00
B	D	−32.08	8.97	33.31	0.00	F	H2	3.62	6.38	7.34	0.75
B	E	−3.64	3.57	5.10	0.22	F	We	9.70	11.75	15.23	0.78
B	Ea	−11.21	12.99	17.15	0.24	F	al	9.76	12.43	15.81	0.76
B	F	−22.37	10.11	24.55	0.07	G	A	−15.82	27.12	31.40	0.30
B	G	−7.82	8.88	11.83	0.14	G	A1	−39.37	31.09	50.17	0.03
B	H2	−21.34	5.76	22.11	0.00	G	B	−10.68	39.50	40.92	0.56
B	We	−16.69	12.34	20.76	0.09	G	C	−47.07	43.78	64.28	0.21
B	al	−16.20	12.92	20.72	0.12	G	D	−50.02	13.16	51.72	0.00
C	C	−0.41	8.53	8.54	0.51	G	E	−16.62	4.30	17.16	0.00
C	Ea	3.89	11.44	12.08	0.65	G	Ea	−21.31	31.62	38.13	0.25
C	G	12.75	13.48	18.56	0.79	G	F	−24.78	19.29	31.40	0.12
C	al	−1.35	11.68	11.76	0.48	G	G	0.57	7.00	7.03	0.68
D	A	21.06	9.86	23.25	0.97	G	H2	−62.02	39.33	73.44	0.00
D	A1	17.31	11.86	20.98	0.92	G	We	−40.11	38.82	55.82	0.18
D	B	33.83	19.32	38.96	0.94	G	al	−35.22	37.15	51.19	0.19
D	C	11.51	17.09	20.61	0.71	H2	A	−28.03	46.09	53.95	0.40
D	D	−2.59	6.86	7.33	0.35	H2	A1	11.56	15.57	19.39	0.85
D	E	35.51	4.15	35.75	1.00	H2	B	−6.97	44.87	45.41	0.62
D	Ea	22.59	15.03	27.13	0.94	H2	C	−37.28	50.99	63.17	0.36
D	F	15.73	12.06	19.82	0.92	H2	D	−1.33	13.66	13.73	0.52
D	G	35.61	8.58	36.62	1.00	H2	E	14.41	3.06	14.73	1.00
D	H2	4.83	13.11	13.97	0.57	H2	Ea	−18.70	49.74	53.14	0.54
D	We	12.03	15.61	19.71	0.77	H2	F	−0.06	11.83	11.83	0.47
D	al	14.31	15.92	21.41	0.80	H2	G	−44.71	46.48	64.49	0.29
E	A	−15.90	14.16	21.29	0.16	H2	H2	−0.16	4.99	4.99	0.51
E	A1	−2.44	11.82	12.07	0.41	H2	We	−31.19	49.99	58.92	0.38
E	B	4.69	10.01	11.05	0.68	H2	al	−25.82	49.01	55.40	0.43
E	C	−9.09	15.15	17.67	0.31	We	G	11.13	9.91	14.90	0.86
E	D	−24.60	10.74	26.84	0.00	We	al	0.65	9.94	9.96	0.52

FSPL (`.../Forge.fspl/FSPL`)

L	T	ME	SD	RE	P	L	T	ME	SD	RE	P
al	A	63.45	9.15	64.11	1.00	al	Ea	67.23	13.10	68.49	1.00
al	A1	65.66	9.23	66.30	1.00	al	F	57.38	10.36	58.31	1.00
al	B	76.56	17.02	78.43	1.00	al	G	75.68	9.30	76.25	1.00
al	C	61.73	12.84	63.05	1.00	al	H2	53.76	6.46	54.15	1.00
al	D	45.45	8.06	46.16	1.00	al	We	58.63	14.00	60.28	1.00
al	E	76.31	3.67	76.40	1.00	al	al	60.42	14.00	62.02	1.00

FSPL-β (`.../Forge.fspl/FSPL.beta`)

L	T	ME	SD	RE	P	L	T	ME	SD	RE	P
A	A	1.10	10.35	10.41	0.49	Ea	A	−5.91	10.57	12.11	0.29
A	A1	7.74	9.29	12.09	0.82	Ea	A1	1.22	9.38	9.46	0.58
A	B	17.15	11.22	20.50	0.93	Ea	B	10.47	10.72	14.98	0.90
A	C	2.74	9.46	9.84	0.62	Ea	C	−3.90	9.44	10.22	0.35
A	D	−13.24	8.99	16.00	0.09	Ea	D	−19.84	9.11	21.83	0.00
A	E	14.92	3.52	15.33	1.00	Ea	E	8.01	3.51	8.75	1.00
A	Ea	6.95	12.33	14.15	0.66	Ea	Ea	0.17	12.43	12.43	0.48
A	F	−3.83	10.13	10.83	0.16	Ea	F	−10.72	10.12	14.74	0.07
A	G	11.48	9.19	14.71	0.86	Ea	G	4.26	9.21	10.14	0.64
A	H2	−3.73	5.43	6.59	0.20	Ea	H2	−10.20	5.50	11.59	0.06
A	We	0.45	10.28	10.29	0.51	Ea	We	−6.09	10.24	11.92	0.29
A	al	1.46	11.37	11.46	0.52	Ea	al	−5.17	11.36	12.48	0.32
A1	A	−7.49	10.62	12.99	0.26	F	A	6.10	10.21	11.89	0.72
A1	A1	−0.24	9.41	9.41	0.52	F	A1	12.38	9.23	15.45	0.92
A1	B	8.97	10.61	13.89	0.88	F	B	21.92	11.61	24.80	0.95
A1	C	−5.39	9.45	10.88	0.29	F	C	7.47	9.52	12.10	0.79
A1	D	−21.32	9.13	23.19	0.00	F	D	−8.53	8.91	12.33	0.17
A1	E	6.46	3.50	7.35	1.00	F	E	19.84	3.53	20.16	1.00
A1	Ea	−1.35	12.45	12.53	0.45	F	Ea	11.78	12.29	17.02	0.82
A1	F	−12.26	10.12	15.90	0.07	F	F	1.08	10.14	10.19	0.44
A1	G	2.64	9.21	9.58	0.57	F	G	16.63	9.18	19.00	1.00
A1	H2	−11.65	5.52	12.89	0.02	F	H2	0.88	5.40	5.47	0.57
A1	We	−7.56	10.25	12.73	0.24	F	We	5.12	10.36	11.56	0.68
A1	al	−6.66	11.37	13.18	0.28	F	al	6.19	11.41	12.98	0.70
B	A	−16.59	10.92	19.86	0.09	G	A	−9.49	10.68	14.29	0.20
B	A1	−8.70	9.56	12.92	0.20	G	A1	−2.10	9.44	9.67	0.42
B	B	0.30	10.03	10.03	0.57	G	B	7.06	10.47	12.63	0.84
B	C	−14.00	9.58	16.97	0.07	G	C	−7.28	9.47	11.95	0.21
B	D	−29.89	9.29	31.30	0.00	G	D	−23.20	9.17	24.95	0.00
B	E	−2.50	3.48	4.29	0.22	G	E	4.49	3.50	5.69	0.89
B	Ea	−10.15	12.64	16.21	0.26	G	Ea	−3.29	12.49	12.91	0.41
B	F	−21.20	10.12	23.49	0.07	G	F	−14.23	10.12	17.46	0.07
B	G	−6.73	9.24	11.43	0.18	G	G	0.58	9.22	9.23	0.54
B	H2	−20.05	5.68	20.83	0.00	G	H2	−13.50	5.55	14.60	0.00
B	We	−16.05	10.36	19.11	0.07	G	We	−9.43	10.26	13.93	0.18
B	al	−15.26	11.49	19.10	0.11	G	al	−8.55	11.39	14.24	0.23
C	A	−2.54	10.46	10.77	0.38	H2	A	6.62	10.20	12.16	0.75
C	A1	4.36	9.34	10.30	0.68	H2	A1	12.87	9.23	15.83	0.92
C	B	13.68	10.95	17.53	0.92	H2	B	22.42	11.65	25.26	0.96
C	C	−0.71	9.44	9.46	0.47	H2	C	7.96	9.53	12.42	0.80
C	D	−16.66	9.05	18.96	0.00	H2	D	−8.04	8.90	11.99	0.17

FSPL-β (`.../Forge.fspl/FSPL.beta`)

L	T	ME	SD	RE	P	L	T	ME	SD	RE	P
C	E	11.33	3.52	11.87	1.00	H2	E	20.36	3.54	20.66	1.00
C	Ea	3.43	12.38	12.84	0.56	H2	Ea	12.29	12.28	17.37	0.84
C	F	−7.40	10.12	12.54	0.07	H2	F	1.59	10.14	10.26	0.48
C	G	7.73	9.20	12.02	0.75	H2	G	17.17	9.18	19.47	1.00
C	H2	−7.09	5.46	8.95	0.12	H2	H2	1.36	5.40	5.57	0.61
C	We	−2.95	10.25	10.66	0.39	H2	We	5.61	10.38	11.79	0.70
C	al	−1.98	11.36	11.53	0.41	H2	al	6.69	11.42	13.23	0.71
D	A	13.26	10.02	16.62	0.90	We	A	0.43	10.37	10.38	0.47
D	A1	19.03	9.17	21.13	0.99	We	A1	7.11	9.30	11.70	0.77
D	B	28.74	12.20	31.22	0.96	We	B	16.51	11.17	19.94	0.93
D	C	14.24	9.69	17.23	0.93	We	C	2.10	9.45	9.68	0.60
D	D	−1.79	8.79	8.97	0.52	We	D	−13.87	9.00	16.53	0.09
D	E	26.89	3.55	27.13	1.00	We	E	14.25	3.52	14.68	1.00
D	Ea	18.71	12.26	22.36	0.95	We	Ea	6.30	12.34	13.85	0.63
D	F	8.11	10.15	12.99	0.87	We	F	−4.49	10.13	11.08	0.13
D	G	24.00	9.17	25.70	1.00	We	G	10.79	9.19	14.17	0.86
D	H2	7.48	5.40	9.23	0.90	We	H2	−4.36	5.43	6.96	0.20
D	We	11.80	10.56	15.84	0.87	We	We	−0.18	10.27	10.28	0.49
D	al	12.96	11.53	17.35	0.87	We	al	0.83	11.36	11.39	0.50
E	A	−14.78	10.86	18.34	0.12	al	A	−0.63	10.41	10.42	0.44
E	A1	−7.01	9.53	11.83	0.24	al	A1	6.13	9.31	11.15	0.73
E	B	2.02	10.14	10.34	0.65	al	B	15.50	11.09	19.06	0.93
E	C	−12.29	9.55	15.56	0.10	al	C	1.10	9.45	9.51	0.56
E	D	−28.18	9.26	29.66	0.00	al	D	−14.87	9.02	17.39	0.09
E	E	−0.72	3.49	3.56	0.44	al	E	13.21	3.52	13.68	1.00
E	Ea	−8.40	12.60	15.14	0.31	al	Ea	5.27	12.35	13.43	0.61
E	F	−19.42	10.12	21.90	0.07	al	F	−5.53	10.13	11.54	0.09
E	G	−4.87	9.24	10.44	0.21	al	G	9.70	9.19	13.36	0.86
E	H2	−18.38	5.64	19.22	0.00	al	H2	−5.33	5.44	7.62	0.16
E	We	−14.36	10.33	17.69	0.09	al	We	−1.16	10.26	10.33	0.45
E	al	−13.55	11.45	17.74	0.13	al	al	−0.17	11.36	11.36	0.47